

Absolute Photoemission Timing

Dissertation

von

Marcus Tobias Ossiander



Fakultät für Physik
Laser- und Röntgenphysik

Absolute Photoemission Timing

Marcus Tobias Ossiander

Vollständiger Abdruck der von der Fakultät für Physik der Technischen Universität München zur Erlangung des akademischen Grades eines Doktors der Naturwissenschaften genehmigten Dissertation.

Vorsitzender: Prof. Dr. Frank Pollmann

Prüfer der Dissertation:

1. Prof. Dr. Reinhard Kienberger
2. Prof. Dr. Martin Stutzmann
3. Prof. Dr. Giuseppe Sansone (nur schriftliche Beurteilung)

Die Dissertation wurde am 02.03.2018 bei der Technischen Universität München eingereicht und durch die Fakultät für Physik am 04.10.2018 angenommen.

Der wahre Zweck des Menschen — nicht der, welchen die wechselnde Neigung, sondern welchen die ewig unveränderliche Vernunft ihm vorschreibt — ist die höchste und proportionierlichste Bildung seiner Kräfte zu einem Ganzen.
Zu dieser Bildung ist Freiheit die erste und unerläßliche Bedingung.

Wilhelm von Humboldt
*Ideen zu einem Versuch, die Grenzen der
Wirksamkeit des Staats zu bestimmen*
1792

Abstract

This work presents the photoemission timing of helium measured with sub-attosecond uncertainty. It reveals how electron interaction slows down photoelectrons participating in a shake-up process by up to 6 attoseconds, which constitutes the first observed attosecond time domain manifestation of electronic correlation. The correlation delay emerges when the photoelectron exiting from the helium atom forces the remaining electron to the opposite side of the photoion, which creates an electric dipole moment and therefore a dc-Stark-shift in the streaking laser field. This process is subsequently exploited to determine the exact quantum state of the prepared photoion.

The helium timing is furthermore used to create an absolute time-zero reference in photoemission by benchmarking the absolute delay predictions of ab-initio modeling, which prove to be accurate to within one attosecond. Absolute referencing is then used to demonstrate how resonances, electron transport and localization, as well as the traversed potentials and electric fields, shape the creation of photoelectrons from atoms, molecules and solids.

The absolute helium reference is utilized to create a time domain perspective on the origin of the giant dipole resonance in iodine. The photoemission timing of a mixture of small iodine-containing molecules and helium proves that electron exit is significantly slowed down by the resonance, suggesting an intermediate step with a lifetime that facilitates photoemission. A Fano-model qualitatively reproduces the measured delay increase, however only accounts for $\sim 70\%$ of the experimental observations and the results of scattering simulations, indicating more complex time domain mechanics than deducible from the photoionization cross-section.

Using the now gauged iodine photoemission as the new absolute clock allows timing the photoelectric effect on a tungsten surface. Comparing tungsten core and conduction band electron exit highlights two domains governing their respective exit delay. While the duration of core level electron exit is explainable by transport and inelastic scattering in the crystal, the conduction band electron exit is dominated by surface emission and proceeds significantly faster than expected from a pure transport model. Subsequently, valence state photoemission from adsorbed iodine atoms is clocked, revealing that vacuum photoelectrons from adsorbate states can be created as fast as from isolated atoms. The measurement demonstrates that virtually lag-free photon-photoelectron interconversion is possible also in solid devices.

Kurzzusammenfassung

Diese Dissertation beschreibt den zeitlichen Ablauf der Photoemission aus einem Heliumatom, gemessen mit einer Unsicherheit von weniger als einer Attosekunde.

Diese Abfolge stellt die erste Zeitbereichsbeobachtung der Elektronenkorrelation im Attosekundenregime dar. Die Dauer des Photoeffekts erhöht sich, wenn das verbleibende Elektron auf die der Photoemission entgegengesetzte Seite des Elternions gedrückt wird und somit ein elektrischer Dipol entsteht, der einem linearen Stark-Effekt im Feld des Messlasers unterworfen ist. Dieser Dipol und sein Entstehungsprozess werden im Folgenden genutzt, um den vollständigen Quantenzustand des so präparierten Photoions zu bestimmen.

Eine Ab-Initio-Simulation reproduziert die ermittelte zeitliche Abfolge mit einer Genauigkeit von unter einer Attosekunde. Das ermöglicht es, den Photoeffekt des Heliumatoms als absolute Referenz für die Bestimmung des Zeitnullpunkts, d. h. die Ankunft des Mess-Laserimpulses am Atom, in anderen Photoemissionsverzögerungsmessungen zu verwenden. Diese Möglichkeit der absoluten Zeitmessung wird in weiteren Experimenten angewendet. Auf diese Weise lässt sich verfolgen, wie Resonanzen, der Transport und die Herkunft von Elektronen in Festkörpern sowie die durchlaufenen Potentiallandschaften und elektrischen Felder die Entstehung eines Photoelektrons aus Atomen, Molekülen und Festkörpern beeinflussen.

Dazu werden die zeitlichen Eigenschaften der Iod-Riesenresonanz, gemessen auf einer absoluten Zeitskala mithilfe der neuen Helium-Referenz, vorgestellt. Die an einem Gasgemisch aus kleinen iodhaltigen Molekülen und Helium durchgeführte Photoemissionsverzögerungsmessung zeigt, dass die Resonanz die Entstehung freier Elektronen verlangsamt. Dies deutet auf einen Zwischenschritt hin, dem eine Lebenszeit zugeordnet werden kann. Ein Modell aus der Beschreibung von Fano-Resonanzen reproduziert qualitativ die Energieabhängigkeit der beobachteten Verzögerung. Quantitative Unterschiede zwischen dem Modell und der Messung beziehungsweise den Ergebnissen von Streutheorierechnungen legen eine komplexere Zeitbereichsdynamik nahe als die, die aus dem Photoabsorptionsquerschnitt geschlossen werden kann.

Mit der nun absolut geeichten Photoemission des Iodatoms als neuer Referenz wird die Dauer des photoelektrischen Effekts an einer Wolframoberfläche bestimmt. Es zeigt sich, dass die Austrittszeiten von Wolfram-Kern- und Leitungsbandelektronen von unterschiedlichen Eigenschaften des Kristalls festgelegt werden. Während der Transport und die inelastische Streuung im Kristall die gemessene Austrittszeit von Kernelektronen erklären, verlassen Leitungsbandelektronen den Kristall deutlich schneller, als von einem solchen Transportmodell vorhergesagt wird. Aufgrund dieser Beobachtung lässt sich der Beitrag von Oberflächenzuständen zur Emissionszeit bestimmen. Außerdem wird die Elektronenerzeugung aus Valenzzuständen von adsorbierten Iodatomen untersucht.

Dabei wird nachgewiesen, dass Elektronen aus diesen Zuständen ähnlich schnell wie aus isolierten Atomen freigesetzt werden können, was den Weg für eine nahezu latenzfreie Photon-Photoelektron-Wandlung in Festkörperbauelementen ebnet.

Curriculum Vitae

Marcus Tobias Ossiander

*18.04.1989, Munich

Education

Technical University of Munich	2015–now
<i>Doctoral Candidate, Chair for Laser and X-ray Physics</i>	
Doctorate Supervisor: Prof. Dr. Reinhard Kienberger	
TUM Graduate School	2015–now
<i>Postgraduate Studies</i>	
International Max Planck Research School of Advanced Photon Science	2014–now
<i>Postgraduate Studies, Kienberger Group</i>	
Technical University of Munich	2012–2014
<i>Master of Science, Condensed Matter Physics</i>	
Master's Thesis: On the Expansion of Attosecond Streaking Spectroscopy towards Ultrafast Surface Dynamics	
McGill University	2012
<i>Exchange Student, Physics</i>	
Technical University of Munich	2009–2012
<i>Bachelor of Science, Condensed Matter Physics</i>	
Bachelor's Thesis: Investigation of Laser Filamentation in a Water Cell	
Johanniter Unfallhilfe e.V.	2008–2009
<i>Compulsory Community Service, In-House Emergency Systems Technician</i>	
Louise-Schroeder-Gymnasium	1999–2008
<i>Abitur</i>	

Scientific Experience

- Max Planck Institute of Quantum Optics** **2014–2017**
Doctoral Research, Attosecond Division
Attosecond Spectroscopy and Femtosecond Laser Development
- Max Planck Institute of Quantum Optics** **2013–2014**
Master's Thesis Research, Attosecond Division
Attosecond Spectroscopy on Solids and Molecules
- University of California, Berkeley** **2012**
Visiting Student Researcher, Müller Group
Atom-Interferometry using Lithium, Laser Cooling, RF-Spectroscopy, Saturation Spectroscopy, Eddy Current Suppression
- Max Planck Institute of Quantum Optics** **2011–2012**
Student Researcher, Attosecond Division
Optical Parametric Chirped Pulse Amplification, Laser Whitelight Creation, Laser Filamentation in Water, Theoretical Work on Light Waveform Synthesis
- Walter Schottky Institut** **2010**
Student Researcher, Finley Group
Research on the Propagation of Surface Plasmon Polaritons on Metallic Nanowires

List of Publications

In order of relevance to this work.

Absolute timing of the photoelectric effect

M. Ossiander, J. Riemensberger, S. Nepll, M. Mittermair, M. Schäffer, A. Duensing, M. Wagner, R. Heider, M. Wurzer, M. Gerl, M. Schnitzenbaumer, J.V. Barth, F. Libisch, C. Lemell, J. Burgdörfer, P. Feulner, R. Kienberger

Nature 561, pp. 374–377, 2018

Attosecond correlation dynamics

M. Ossiander, F. Siegrist, V. Shirvanyan, R. Pazourek, A. Sommer, T. Latka, A. Guggenmos, S. Nagele, J. Feist, J. Burgdörfer, R. Kienberger, M. Schultze

Nature Physics 13, pp. 280–285, 2017

Carrier frequency tuning of few-cycle light pulses by a broadband attenuating mirror

O. Razskazovskaya, M. Ossiander, F. Siegrist, V. Pervak, M. Schultze

Applied Optics 56.32, pp. 8978–8982, 2017

Attosecond photoelectron streaking with enhanced energy resolution for small-bandgap materials

A. Guggenmos, A. Akil, M. Ossiander, M. Schäffer, A. M. Azzeer, G. Böhm, M.-C. Amann, R. Kienberger, M. Schultze, U. Kleineberg

Optics Letters 41.16, pp. 3714–3717, 2016

Chromium/Scandium multilayer mirrors for attosecond pulses at 145 eV

A. Guggenmos, M. Jobst, M. Ossiander, S. Radünz, J. Riemensberger, M. Schäffer, A. Akil, C. Jakubeit, P. Böhm, S. Noever, B. Nickel, R. Kienberger, F. Krausz, U. Kleineberg

Optics Letters 40.12, pp. 2846–2849, 2015

Few-Femtosecond Wave Packet Revivals in Ozone

T. Latka, V. Shirvanyan, M. Ossiander, O. Razskazovskaya, A. Guggenmos, M. Jobst, M. Fieß, S. Holzner, A. Sommer, M. Schultze, C. Jakubeit, J. Riemensberger, B. Bernhardt, W. Helml, F. Gatti, B. Lasorne, D. Lauvergnat, P. Decleva, G. J. Halász, Á. Vibók, R. Kienberger

in review

Attosecond chronoscopy of soft x-ray photoemission from resonant sp-band excitation

J. Riemensberger, S. Neppl, D. Potamianos, M. Schäffer, M. Schnitzenbaumer, M. Ossiander, A. Guggenmos, U. Kleineberg, P. M. Echenique, F. Allegretti, D. Menzel, J. Barth, A. G. Borisov, A. K. Kazansky, R. Kienberger, P. Feulner

in preparation

Optical study of lithographically defined, subwavelength plasmonic wires and their coupling to embedded quantum emitters

G. Bracher, K. Schraml, M. Ossiander, S. Frédérick, J. J. Finley, M. Kaniber

Nanotechnology 25.7, 075203, 2014

Carrier-envelope-phase-stable, 1.2 mJ, 1.5 cycle laser pulses at 2.1 μm

Y. Deng, A. Schwarz, H. Fattahi, M. Ueffing, X. Gu, M. Ossiander, T. Metzger, V. Pervak, H. Ishizuki, T. Taira, T. Kobayashi, G. Marcus, F. Krausz, R. Kienberger, N. Karpowicz

Optics Letters 37.23, pp. 4973–4975, 2012

Active stabilization for optically synchronized optical parametric chirped pulse amplification

A. Schwarz, M. Ueffing, Y. Deng, X. Gu, H. Fattahi, T. Metzger, M. Ossiander, F. Krausz, R. Kienberger

Optics Express 20.5, pp. 5557–5565, 2012

Presented Conference Contributions

Absolute Timing of Photoemission from Atoms and Solids

M. Ossiander, J. Riemensberger, F. Siegrist, S. Neppl, M. Mittermair, M. Schäffer, A. Duensing, M. Wagner, R. Heider, J.V. Barth, M. Schultze, P. Feulner, R. Kienberger

Oral Presentation, ATTO, Xi'an 2017

Attosecond correlation dynamics

M. Ossiander, F. Siegrist, V. Shirvanyan, R. Pazourek, A. Sommer, T. Latka, A. Guggenmos, S. Nagele, J. Feist, J. Burgdörfer, R. Kienberger, M. Schultze

Poster, Atomic Physics, Dresden 2016

Correlation Effects in the Photoemission Delay of Helium

M. Ossiander, F. Siegrist, V. Shirvanyan, R. Pazourek, A. Sommer, T. Latka, A. Guggenmos, U. Kleineberg, F. Krausz, R. Kienberger, M. Schultze

Oral Presentation, Ultrafast Phenomena, Santa Fe 2016

Photon Energy Dependent Photoemission Delay in Tungsten

M. Ossiander, M. Jobst, S. Neppl, J. Riemensberger, M. Schäffer, E.M. Bothschafter, M. Gerl, A. Kim, A. Akil, S. Jarosch, J.V. Barth, F. Krausz, P. Feulner, R. Kienberger

Oral Presentation, Ultrafast Optics, Beijing 2015

Attosecond electron dynamics in layered systems

J. Riemensberger, M. Ossiander, M. Jobst, S. Neppl, M. Schäffer, A. Kim, A. Guggenmos, P. Feulner, R. Kienberger

Oral Presentation, ATTO, Montreal 2015

Attosecond electron dynamics in layered systems

M. Ossiander, M. Jobst, J. Riemensberger, S. Neppl, M. Schäffer, A. Kim, P. Feulner, R. Kienberger

Oral Presentation, LASERLAB INREX Meeting, Munich 2015

Tunable High Flux Attosecond XUV Sources

M. Ossiander, T. Latka, V. Shirvanyan, A. Guggenmos, M. Jobst, J. Riemensberger, M. Schäffer, P. Feulner, R. Kienberger

Oral Presentation, COST X-ray Telescopes Meeting, Milan 2015

Towards the Absolute Timing of Photoemission from Condensed Matter Systems

M. Ossiander, J. Riemensberger, M. Schäffer, M. Gerl, A. Schiffrin, J.V. Barth, F. Krausz, R. Kienberger, P. Feulner, S. Neppl

Oral Presentation, Ultrafast Phenomena, Okinawa 2014

Contents

Abstract	vii
Kurzzusammenfassung	ix
Curriculum Vitae	xi
List of Publications	xiii
Presented Conference Contributions	xv
1 Introduction	1
2 Ultrashort Laser Pulses in the Time and Frequency Domain	3
2.1 Atomic Units, International System of Units and Electron Volts	3
2.2 General Description of Ultrashort Laser Pulses	4
2.3 Differences of a Single versus a Train of Light Pulses	7
3 Delaying and Expediting Electron Wave Packets	9
3.1 A Classical Concept of Delay	9
3.2 Delay in Quantum Scattering — Eisenbud-Wigner-Smith Delay	11
3.3 Relating Photoemission and Scattering	14
3.4 Photoemission Delays of Hydrogenic Systems	15
4 Photoelectron Timing Measurement	17
4.1 Attosecond Pulse Generation	17
4.1.1 Generation of Attosecond Pulse Trains	17
4.1.2 Isolation of Individual Attosecond Pulses	18
4.1.3 Phase Matching	21
4.2 The Attosecond Streak Camera	22
4.2.1 Classical Description	25
4.2.2 Quantum Mechanical Description	26
4.2.3 Photoemission Delay Retrieval	29
4.2.4 Relating Streaking and Eisenbud-Wigner-Smith Delays — Coulomb-Laser-Coupling	30
4.2.5 Disentangling Photoemission Delays from Attosecond Pulse Prop- erties	31

5	Attosecond Correlation Dynamics — Setting an Absolute Reference	35
5.1	Absolute Timing of Helium Photoemission	36
5.2	Photoemission Pathways in Helium	36
5.2.1	Experimental Setup	37
5.2.2	Delay Retrieval and Experimental Results	41
5.2.3	High Order Photoemission Phase Terms	46
5.2.4	Isolation of the n=2 Shake-Up Delay	47
5.3	Contributions to the Photoemission Delay	49
5.3.1	Direct Photoemission	49
5.3.2	Shake-Up Photoemission into n=2	50
5.4	Correlation Delay	51
5.5	Shake-Up into n>2 States	54
5.6	Complete Measurement of a Quantum State	55
6	Absolute Photoemission Delays from Small Molecules	57
6.1	Measurement of the Absolute Iodine 4d Photoemission Delay	58
6.1.1	Preparation of Gas Mixtures	59
6.1.2	Laser, Beamline, and Electron Detection Setup	59
6.1.3	Data Retrieval and Statistical Evaluation	60
6.1.4	Estimation of Molecular Orbital and Shake-Up Influences	61
6.1.5	Estimation of Auger Influence	63
6.1.6	Absolute Streaking and Wigner Delay for Iodine 4d Photoemission	64
6.2	Simulation of Photoemission from Small Molecules	65
6.3	Time Domain Evaluation of the Giant Dipole Resonance in Iodine	67
7	Absolute Timing of Condensed Matter Photoemission and Adsorbates	73
7.1	The Atomic Chronoscope Method	74
7.2	Experimental Photoemission Timing of I/W(110)	75
7.2.1	Sample Preparation	76
7.2.2	Data Retrieval and Statistical Evaluation	76
7.2.3	Estimation of Surface Influences on Iodine 4d Photoemission	79
7.3	Absolute Timing of Crystal and Surface Photoemission	79
7.4	Adsorbate State Photoemission Delays	82
8	Strongly Correlated Materials — The Opportunities of Photoelectron Timing	85
9	Summary	89
10	Outlook	91
A	Photoemission Delay Retrieval	93
A.1	Center-of-Energy Retrieval	93
A.2	Restricted Time-Dependent Schrödinger Equation Retrieval	95
A.3	Generalized-Projections Retrieval	96

A.4	Chirped Gaussian Pulses in the Time and Frequency Domain	100
A.5	Photoemission Cross-Section — Extreme-Ultraviolet Chirp Delay Distortion	103
A.6	Data Conversion and Energy Calibration	104
A.7	Background Subtraction	105
B	Experimental Tools	107
B.1	FP2 Laser System	107
B.2	FP3 Laser System	109
B.3	The Femtopower at the Technical University of Munich	109
B.4	The Attosecond Beamline at the Technical University of Munich	110
B.5	The Bulk and Gas Phase Beamline AS2	111
B.6	The Surface Science Beamline AS3	111
	Bibliography	113
	Abbreviations	127
	Danksagung	129

Chapter 1

Introduction

One of the universal interactions of matter and light is the release of a bound electron after the absorption of an energetic photon. The observation of the photoelectric effect by Heinrich Hertz and Wilhelm Hallwachs in metallic surfaces [1, 2] and its explanation by Albert Einstein [3] through the application of Max Planck's quantized origin of thermal radiation [4] is one of the pillars of quantum mechanics. Furthermore, because photoemission can occur in systems of any complexity and at continuous energy, it has been pivotal for the unraveling of the inner workings of atoms, molecules, and crystals for over a century. Up to today, angle-resolved photoelectron spectroscopy is one of the most potent ways to examine the electronic properties of solids, be it the band structure of simple metals and semiconductors or gap-opening and Cooper-pairing in high-temperature superconductors.

It is all the more astonishing that the duration of the photoemission process, a rather natural property, went unrecognized until a decade ago, mainly due to its minuteness. With magnitudes at the lower edge of the attosecond realm, following the birth of a photoelectron requires tools that can resolve such timescales. These instruments were first demonstrated around the turn of the millennium [5] and the first photoemission timing measurement using the attosecond streak camera performed for a solid sample in 2007 [6]. Photoemission delays were generalized to atoms three years later [7], repeating the historical order of the photoelectric effect's discovery. Extensive research led to the observation of photoemission delays also in molecules [8–10] and other atoms [11–14], as well as in the vicinity of Fano resonances [15, 16] and during double ionization [17]. Photoemission timing of solid samples identified effects of classical transport [18, 19], elastic and inelastic scattering [20, 21], screening [19, 21] and final states [22].

Following ultrafast physical dynamics requires exact knowledge about not only the instant of measurement but also the instant when the examined process began, which is predominantly achieved by intentionally starting dynamics using a short pump pulse of light and then observing the system's state at adjustable delay with a second probe burst of light. What is a straightforward concept down to femtochemistry gains new complexity when entering the attosecond realm. The creation and propagation of a light pulse cannot yet be predicted with attosecond precision. Therefore, the pump-probe delay has to be calibrated. However, even the measurement of two pulses' absolute delay with attosecond precision is demanding because the intrinsic response time of the measurement device, which is often a single atom, quickly exceeds the required uncertainty. As a result, all mentioned experiments rely on relatively comparing photoelectron timing. Despite being

unquestionably powerful, the method has a disadvantage: general delays, occurring in all compared features or processes, are overlooked, and delay contributions cannot be unambiguously assigned to one origin.

This thesis remedies this common flaw by introducing a universally applicable way to achieve an absolute gauge in attosecond science and demonstrates its viability to the three most common classes of matter: atoms, molecules, and condensed matter.

The work starts with a brief introduction to the description of ultrashort laser pulses, which constitute the basis of the presented research. The photoemission delay is then conceptualized by drawing lines from the classical notion of delay to the quantum picture of a scattering delay and then to the photoemission process. Furthermore, photoemission delays of hydrogenic systems are discussed to develop fundamental trends. The attosecond streak camera is the primary measurement technique used in the presented research. Its modeling and the intricacies of its application for photoemission timing are introduced in a chapter along with how attosecond pulses are generated via high-harmonic generation. Three experiments that introduce and demonstrate the use of helium photoemission as absolute clock make up the central part of the work. The first experiment sets and tests the absolute helium reference with a precision and accuracy of better than 1 as, usable to introduce an absolute scale to attosecond pump-probe measurements. The reference is set by clocking simple and correlated processes in the photoemission spectrum of helium and understanding the delay contributions. A correlation delay is identified, which demonstrates how electron interaction influences the photoemission process on the attosecond timescale and subsequently allows to determine the complete photoion and photoelectron quantum state prepared by photoemission. In the next chapter, the new reference is applied to examine the photoemission timing of iodine, in which electron interaction gives rise to a giant dipole resonance. The absolute photoemission timing reveals a clear signature of the resonance in the photoemission delay and opens a new perspective on a process that was only accessible through its cross-section in the past. Subsequently, the reference and giant dipole resonance data will be combined with solid-state photoemission timing. Through two-, respectively three-step referencing, the absolute photoelectron exit times from tungsten bulk, surface and adsorbate states are determined. The absolute scale allows scrutinizing the transport dynamics and origin of these electrons. Finally, a proof-of-principle experiment on high-temperature superconductors provides an outlook into the future possibilities of timing photoelectron emission from strongly correlated systems.

Chapter 2

Ultrashort Laser Pulses in the Time and Frequency Domain

A central aspect in the modeling of any ultrashort laser experiment is describing the involved light pulses. It is especially instructive in the photoemission context since many concepts transfer seamlessly to free electron wave packets, which will be addressed in the next chapter. Standard texts commonly treat the description of ultrashort light transients. However, the relation to experimental quantities is often not explicitly worked out, and normalization is hardly addressed. Therefore, the critical concepts of pulse description will be briefly introduced. The naming convention follows [23].

2.1 Atomic Units, International System of Units and Electron Volts

Light and electron pulse description is briefer in atomic units as opposed to the International System of Units (SI). In Hartree atomic units, the electron mass, its charge and the reduced Planck's constant are defined to be unity. Other quantities are derived from those values [24]. This unit system is used in equations throughout this thesis to accentuate the key dependencies. Nonetheless, experimental data is commonly reported in SI or other unit systems. Besides the three base definitions, conversion factors necessary in the scope of this thesis are given in the following. A precise list of conversion factors including uncertainties can be found online [25].

Time in atomic units is measured in units of $1 \text{ at. u.} = 24.2 \text{ as}$, and the length measure is the Bohr radius, thus $1 \text{ at. u.} = 52.9 \text{ pm}$. The vacuum speed of light in atomic units is given by the fine structure constant $c_0 = \alpha \approx 1/137$. The electric field unit corresponds to $1 \text{ at. u.} = 5.14 \times 10^{11} \text{ V/m}$, and the unit of intensity is $1 \text{ at. u.} = 6.43 \times 10^{15} \text{ W/cm}^2$ [26]. A feature of atomic units is the equivalence of photon energy and photon angular frequency. The conversion to SI units is $1 \text{ at. u.} = 1/24.2 \text{ as}$ for angular frequency and $1 \text{ at. u.} = 4.36 \times 10^{-18} \text{ J}$ for energy. Not in the SI-system, but often more appropriate due to its smaller magnitude is the use of electron volts, which is related to atomic units by $1 \text{ at. u.} = 27.2 \text{ eV}$.

2.2 General Description of Ultrashort Laser Pulses

When examining the interaction of a few-cycle ultrashort laser pulse with an atom, its magnetic field components and spatial properties are often negligible. If true, this allows describing such pulse using its electric field evolution over time, $E(t)$. This real quantity can be measured as the time-dependent force a laser pulse exerts on a test charge, which is challenging for visible (VIS) light laser pulses due to their rapid oscillation. It is possible, e.g., using the attosecond streak camera [27]. A pulse's energy transport per time through an area in a vacuum is called the instantaneous intensity $I(t)$. It is calculated from the electric field via

$$I(t) = \frac{1}{4\pi\alpha} E^2(t). \quad (2.1)$$

Literature often does not substantiate between the instantaneous and average intensity, whose definition includes an additional factor $1/2$. Its source is in the calculation of the time-averaged energy transport of a monochromatic wave. However, since consecutive field oscillations in a few-cycle laser pulse heavily deviate and light fields do not transport energy during zero crossings, the utility of such quantity for few-cycle-pulses is questionable. From the instantaneous intensity, the energy transport of the complete pulse per area, called the radiant fluence H_e , can be found by time integration

$$H_e = \int_{-\infty}^{\infty} dt I(t). \quad (2.2)$$

This quantity has to be invariant under Fourier transformation of $E(t)$, due to energy preservation. Therefore, when describing the same pulse in the spectral domain, integration of the spectral intensity $\int_0^{\infty} d\omega I(\omega) = H_e$ has to yield the same radiant fluence. $I(\omega)$ is straightforward measurable, e.g., using a grating spectrometer, or can even be perceived as color by the human eye. It is only non-zero for positive frequencies. Calculating the spectral field amplitude introduces a subtlety. Since the time-dependent electric field $E(t)$ is defined as a real quantity, its Fourier transform $\mathcal{F}(E(t)) = \tilde{E}(\omega)$ has to satisfy $\tilde{E}(\omega) = \tilde{E}^*(-\omega)$. This symmetry creates the need for spectral components at negative frequencies, which are not observable using a spectrometer and carry no additional information. Consequently, the spectral field amplitude is derived from the measured spectral intensity using

$$|\tilde{E}(\omega)| = |\tilde{E}^+(\omega)| = \sqrt{\frac{4\pi\alpha}{2} I(\omega)} \quad \text{for } \omega > 0 \quad (2.3)$$

$$|\tilde{E}(\omega)| = |\tilde{E}^-(\omega)| = \sqrt{\frac{4\pi\alpha}{2} I(-\omega)} \quad \text{for } \omega < 0. \quad (2.4)$$

As implied, the complex spectral field $\tilde{E}(\omega)$ is often split into a positive and negative frequency part $\tilde{E}(\omega) = \tilde{E}^+(\omega) + \tilde{E}^-(\omega)$. Both, $\tilde{E}^+(\omega)$ and $\tilde{E}^-(\omega)$ have a complex time domain equivalent, $\tilde{E}^+(t)$ and $\tilde{E}^-(t)$, obtained via inverse Fourier transform. Due to the

symmetry, knowledge of only \tilde{E}^+ is enough to describe a pulse. The original and real time-dependent field can be retrieved using

$$E(t) = 2\text{Re} \left(\tilde{E}^+(t) \right). \quad (2.5)$$

As any complex quantity, we can split \tilde{E}^+ into an amplitude and a phase part:

$$\tilde{E}^+(\omega) = \left| \tilde{E}^+(\omega) \right| e^{i \arg(\tilde{E}^+(\omega))} = \frac{1}{2} \mathcal{E}(\omega) e^{i \phi_\omega(\omega)} \quad (2.6)$$

$$\tilde{E}^+(t) = \left| \tilde{E}^+(t) \right| e^{i \arg(\tilde{E}^+(t))} = \frac{1}{2} \mathcal{E}(t) e^{i \phi_t(t)} \quad (2.7)$$

This separation is convenient in both the time and frequency domain because many experimental observables can be deduced from the new constituents. In the time domain the temporal envelope $\mathcal{E}(t)$ carries information about the duration and shape of a light pulse, but no information about its oscillation. The temporal phase $\phi_t(t)$ describes the oscillation frequency and its change. Respectively, in the spectral domain, the spectral envelope $\mathcal{E}(\omega)$ represents the bandwidth and color of a laser pulse but carries no information about how the frequencies are arranged in time. This information is contained in the spectral phase $\phi_\omega(\omega)$.

Instantaneous Frequency

An essential property of a light pulse is its frequency of oscillation at a particular time. It is called instantaneous frequency and can be found from the temporal phase by derivation:

$$f_{\text{inst}}(t) = \frac{1}{2\pi} \omega_{\text{inst}}(t) = -\frac{1}{2\pi} \frac{d}{dt} \phi_t(t) \quad (2.8)$$

Carrier Frequency

A quantity describing the color of a laser pulse as a single number is the so-called carrier frequency ω_0 . Although straightforwardly defined for a monochromatic wave, its definition for a pulse of significant spectral width is more cumbersome. Different options exist, some sources even describe it as arbitrarily selectable helper quantity. A physical choice exists: in theory, any coherent light pulse is compressible, i.e., can be manipulated to possess linear spectral and temporal phase, even though it might be technically challenging to achieve. Such a compressed laser pulse exhibits only a single frequency of oscillation over the whole pulse duration, hence is the physical choice for the carrier frequency. In the time domain, this frequency is the intensity weighted mean of the instantaneous frequency, which coincides with the intensity weighted spectrum in the spectral domain:

$$\omega_0 = \frac{\int_{-\infty}^{\infty} dt I(t) \omega_{\text{inst}}}{\int_{-\infty}^{\infty} dt I(t)} = \frac{\int_0^{\infty} d\omega I(\omega) \omega}{\int_0^{\infty} d\omega I(\omega)} \quad (2.9)$$

In the time domain, the carrier frequency can be used to separate the primary oscillation of a laser pulse from more faint effects such as chirp. For this purpose, the complex

envelope $\tilde{\mathcal{E}}(t)$ is defined as the product of the temporal envelope and the temporal phase exponential $e^{i\varphi_t(t)}$ excluding the carrier oscillation. Its Fourier transform is the complex spectral envelope, which is a replica of $\tilde{E}^+(\omega)$ shifted to the origin of the frequency axis:

$$\mathcal{E}(t)e^{i\phi_t(t)} = \mathcal{E}(t)e^{i\varphi_t(t)}e^{-i\omega_0 t} = \tilde{\mathcal{E}}(t)e^{-i\omega_0 t} \quad (2.10)$$

Chirp

The second derivative of the temporal phase, i.e., its curvature, is called a pulse's chirp β_t . Measuring the change in the instantaneous frequency, it represents how fast the oscillation frequency of a pulse changes over time:

$$\beta_t(t) = -\frac{1}{2\pi} \frac{d^2}{dt^2} \phi_t(t) \quad (2.11)$$

Group Delay

The equivalent to the instantaneous frequency in the frequency domain is the time at which a specific color is found in the pulse, referred to as group delay. It is found by derivation of the spectral phase:

$$GD(\omega) = \frac{d}{d\omega} \phi_\omega(\omega) \quad (2.12)$$

Group Delay Dispersion

Derivation of the group delay yields the group delay dispersion, which describes the change of the group delay with varying photon energy. It is thus closely related to a pulse's chirp:

$$GDD(\omega) = \frac{d}{d\omega} GD(\omega) = \frac{d^2}{d\omega^2} \phi_\omega(\omega) \quad (2.13)$$

Carrier-to-Envelope Phase

The temporal phase ϕ_{CEP} at the maximum of the temporal envelope is called the carrier-to-envelope phase (CEP). It describes the offset of a light pulse's oscillation relative to its envelope. For light pulses longer than a few carrier oscillations it can often be ignored. However, for few-cycle pulses, it substantially changes the ratio between the highest field crests contained in the pulse and can therefore have significant effects on nonlinear processes and attosecond experiments. The two extreme cases are illustrated in figure 2.1. They are referred to as cosine ($\phi_{\text{CEP}} = 0$, $\phi_{\text{CEP}} = \pi$) and sine ($\phi_{\text{CEP}} = \pi/2$, $\phi_{\text{CEP}} = 3\pi/2$) pulses, which represent light pulses that have the maximum and minimum possible global field maximum for a specific pulse envelope. More importantly, the cosine pulse only exhibits one global maximum, while a sine pulse contains two.

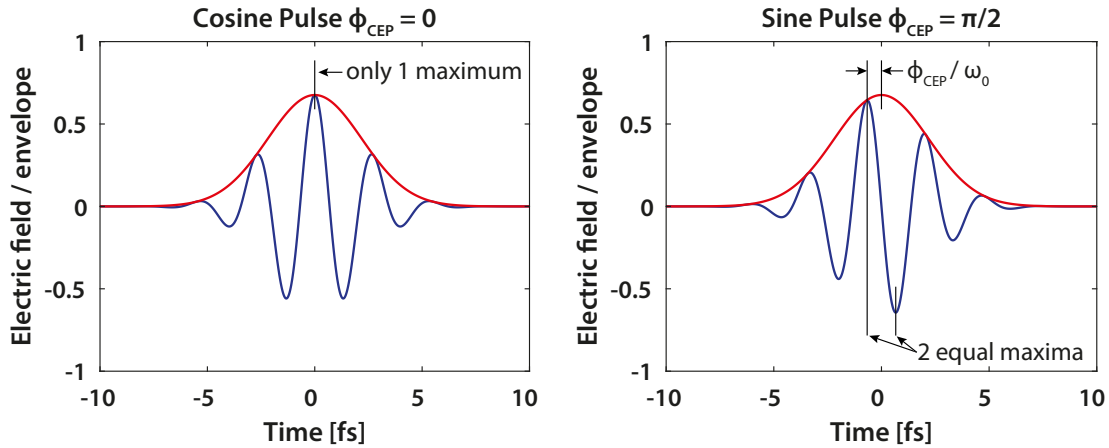


Figure 2.1: Ultrashort cosine and sine pulse electric fields (blue) and temporal envelopes (red). The carrier-to-envelope phase ϕ_{CEP} (CEP) defines the shift of the global field maximum under the envelope. The case exhibiting the largest global field maximum is called cosine pulse, while the opposite sine pulse contains two equally high maxima. ω_0 represents the carrier-frequency.

2.3 Differences of a Single versus a Train of Light Pulses

So far, only a single isolated pulse in the time domain was considered. It exhibits a smooth and unmodulated spectral intensity. This isolation disregards reality when considering how such pulses are created. In a femtosecond laser source, a concentrated packet of light oscillates between two cavity end mirrors and is amplified in a population inverted gain medium. One of these mirrors has slightly less than perfect reflectivity, such that each time the packet is reflected, a small replica of the packet is coupled out, forming the light beam used in experiments. Because the optical path length in the cavity and the speed of light is well defined, this outcoupled beam is a regular train of light pulses with equal envelopes, spaced in time by the round-trip time of the laser cavity, i.e., the inverse repetition rate f_{rep} . The same is true in the case of high-harmonic generation if more than one laser cycle contributes to the process. When calculating the spectral intensity of such a regular pulse train, it is not smooth, but consists of many regularly spaced sharp teeth. Therefore, femtosecond oscillators are also-called frequency combs. The frequency spacing between two such teeth is precisely f_{rep} . Because the repetition rate in a femtosecond train is low compared to optical frequencies, the teeth are not resolved by conventional spectrometers. However, in an attosecond pulse train, the repetition rate is given by the inverse of half the femtosecond driver laser period, which is on the order of one to a few femtoseconds. This small time-domain spacing results in spectral modulation frequencies of a few hundred meV to a few eV, which are resolved by XUV spectrometers. The remaining degree of freedom is the absolute position of the spectral modulation, equivalent to the offset of the (usually vanishing) first comb in the spectrum from zero frequency. This offset f_{CEO} is called the carrier-to-envelope offset (CEO) frequency and

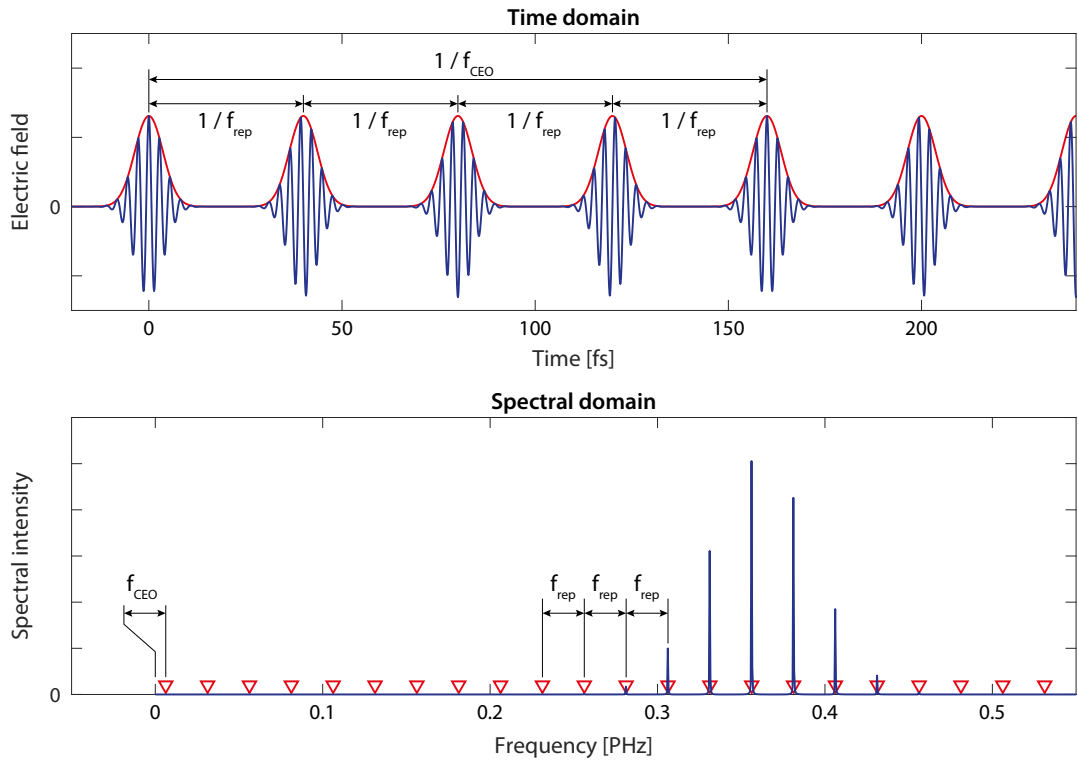


Figure 2.2: Pulse trains in the time and frequency domain. Upper panel: the repetition rate f_{rep} defines the spacing between consecutive maxima of the pulse envelope (red). The carrier-to-envelope offset frequency f_{CEO} fixes the spacing between pulses with equal electric fields (blue). Lower panel: possible comb frequencies (red triangles) are given by the absolute offset of the first tooth f_{CEO} and the spacing between consecutive teeth f_{rep} . Real teeth (blue) only exist within the spectral range of a single pulse.

is the frequency at which two pulses with equal electric field under the envelope occur in the pulse train. Figure 2.2 illustrates the properties for a femtosecond pulse train with extremely high repetition rate. Therefore, the frequency teeth are widely spaced. Every fourth pulse is identical, thus $f_{\text{CEO}} = f_{\text{rep}}/4$. Stabilizing f_{rep} and f_{CEO} allows creating an extremely precise ruler for spectroscopy, a development which was honored with a Nobel Prize for Roy J. Glauber, John L. Hall, and Theodor W. Hänsch in 2005 [28]. In most attosecond applications, only f_{CEO} is stabilized, which allows creating field transients with controlled CEP, important for the generation of isolated attosecond pulses.

Chapter 3

Delaying and Expediting Electron Wave Packets

The central observable in this thesis is the photoemission delay. What seems — at first glance — as a straightforward concept, bears pitfalls, which sometimes lead to misconceptions or even apparent problems with causality. Therefore, the idea and proper definition will be developed in the following section in the notion of a scattering experiment. Then the quantum concept of scattering delay as developed by Eisenbud, Wigner, and Smith will be discussed, from which a line will be drawn to photoemission timing in general and simple systems.

3.1 A Classical Concept of Delay

To understand many of the main properties of delay and the boundary conditions necessary for a robust definition, an example, intuitively solved by a kid, can be considered: what happens to a sled when it slides through a shallow, finite pit in the snow? The problem is illustrated in figure 3.1 (a). The shallowness mitigates effects of the sled's deflection and highlights those caused by velocity changes, which allows drawing parallels to a one-dimensional potential from this two-dimensional example.

When the sled enters the pit, it accelerates until the lowest point due to gravity. Subsequently, it decelerates until it reaches the verge of the ditch and if both sides of the pit share the same elevation, its speed before the ditch is restored. There are two possibilities to examine the time-properties of this event: one could either define a start and finish line and measure the time it takes the sled to traverse the distance in between with a stopwatch. However, the recorded time depends mainly on how the start and finish lines are chosen, which is exceptionally grave far away from the pit, where its influence becomes negligible. The second way is to introduce a second (reference) sled that starts at the same speed next to the first sled, but slides over a bridge across the trench and then clock the arrival time difference between the two sleds at any point after the pit. This way has two main advantages: the measurement does not depend on picking the finish line (as long as it is far away from the ditch), thus it is well defined, and it directly characterizes the difference the pit makes, even if the observer is at an infinite distance. Consequently, a well-defined negative time delay (advance) can be assigned to the event *sled sliding through the pit*, but the concept requires the reference sled.

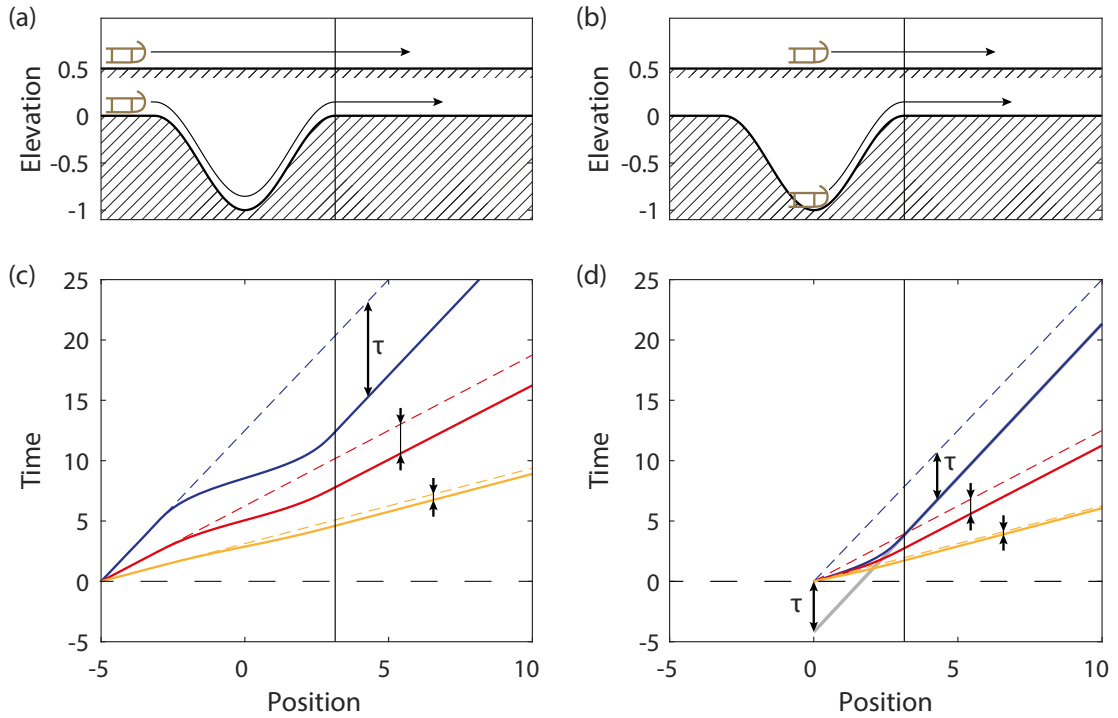


Figure 3.1: Panel (a): a sled with finite initial velocity slides into and out of a shallow short-ranged pit. Its horizontal speed temporarily increases, causing it to arrive at the far verge of the ditch (black vertical line) faster than a sled that slides on flat land with the same starting conditions. After the trench, the delay between the sleds is well defined and constant, since the final energy of the sleds is equal. The position-time diagram (c) illustrates the initial momentum dependence of this time advance: sleds with decreasing initial velocity (full yellow, red, blue lines) are more advanced after the pit (black arrows, τ) compared to their flat-land references (dashed lines). Panel (b): a sled starts at the bottom of a ditch with enough initial velocity to escape it. Once the sled arrives at the verge of the trench, its speed stays constant. A sled with the same initial velocity on flat land is now a bad reference because the pit slows the other sled down. Therefore, the delay between those sleds is position dependent, even far from the ditch. To achieve a position-independent measure of the time advance caused by the trench, one must compare two sleds with the same final velocity and horizontal starting position. In this case, the sled starting in the pit is advanced, because it started at higher horizontal speed. For equal final velocities, the time advance in (d) is half of that in (c). Asymptotically, one cannot distinguish a sled that started in a pit from a sled on flat land with a head start (grey line in (d)). Both cases result in a negative delay.

The position-time diagrams for three sleds entering the trench with different initial speeds are shown in figure 3.1 (c). The time advance caused by the pit is decreasing along increasing initial sled velocity, especially slow sleds are noticeably advanced compared to their references. In the limit of an ambling sled, the time advance diverges. The observed time advance changes to a delay if the pit is exchanged for a hill. The diverging limit is now occurring for sleds that are ambling on top of the elevation, since even slower sleds are reflected and therefore never reach the measurement area.

In the classical limit, the above concepts apply to electron scattering experiments, though there are differences, i.e., other potentials, interactions, and constraints.

3.2 Delay in Quantum Scattering — Eisenbud-Wigner-Smith Delay

Apart from the classical limit, an equivalent picture of delay for a quantum particle has to exist for the correct description of wave packets. Eisenbud investigated the quantum particle delay caused by scattering from a potential in his doctoral thesis [29]. Later, Wigner examined causality constraints [30], and Smith introduced a lifetime matrix for multichannel systems [31]. Honoring their achievements, scattering delays from short-ranged potentials are referred to as Eisenbud-Wigner-Smith (EWS) delays. This section will give a brief introduction to the EWS delay following Wigner's explanation and from an ultrashort-laser perspective [30]. An extensive mathematical discourse about the quantum time delay can, e.g., be found in [32].

The delay concept for a quantum particle will be explored by replacing the ditch with a short ranged attractive potential and the sled with an electron wave packet. The aim is again to examine the potential by sending a measurement wave packet through it and comparing it to a reference wave packet. Figure 3.2 illustrates the situation. The time properties of this system can be extracted by considering wave packet train solutions to the time-independent Schrödinger equation. In an infinite train of electron pulses, some of the pulses will always be found before the attractive potential, while others will already have traversed it. For illustrative purposes, the individual plane wave energies and phases in figure 3.2 (b) were chosen such that there is a compressed electron pulse just left and another one just right of the potential. The train of electron wave packets consists of multiple Eigenstates of the system in a frequency comb, following the concept of light pulse trains introduced in section 2.3. Some of these Eigenstates are plotted in figure 3.2 (c). As in the classical case, a reference is needed to define a meaningful scattering delay, which in this case is the same pulse train propagating without feeling the potential ditch.

Two effects are noticeable when comparing the electron pulses left and right of the attractive potential: first, the pulses are significantly broadened in space after the pit. This spreading is not a feature of the potential since it is also observed for the reference, but rather the vacuum dispersion of an electron causing it to diffuse with time. Second, the envelope of the wave packet that experienced the attractive potential is advanced in space compared to the reference. This advance stays constant, therefore is well defined on both sides of the attractive potential, which can be verified when addressing farther

pulses on both sides (not shown).

For simplicity, only one wave packet propagating in positive space direction x with central energy E will now be treated. The reference wave packet $\Psi_{\text{reference}}$ is chosen as a sum of two closely spaced plane waves, with energies $E - \delta E$ and $E + \delta E$ and wave numbers $k - \delta k$ and $k + \delta k$:

$$\Psi_{\text{reference}} = e^{i(k-\delta k)x - i(E-\delta E)t} + e^{i(k+\delta k)x - i(E+\delta E)t} \quad (3.1)$$

The central position of this packet is found at the position where both waves interfere constructively, i.e., at position

$$x_{\text{reference}} = t \frac{\delta E}{\delta k} \quad \text{where} \quad -x \delta k + t \delta E \stackrel{!}{=} x \delta k - t \delta E. \quad (3.2)$$

If the same wave packet scatters from a potential, the components will acquire a phase shift because the wave packet's oscillation is modified in the potential region. Due to the ratio of change over the initial oscillation, the effect is more drastic for the lower energy component. Therefore, its phase evolution is shifted by $-(\phi + \delta\phi)$ and that of the higher energy component by $-(\phi - \delta\phi)$. The exact shift is defined by the shape and magnitude of the potential, in the current convention an attractive potential causes a negative phase shift. The scattered wave and its position are then described by

$$\Psi_{\text{scattered}} = e^{i(k-\delta k)x - i(E-\delta E)t - i(\phi + \delta\phi)} + e^{i(k+\delta k)x - i(E+\delta E)t - i(\phi - \delta\phi)} \quad (3.3)$$

$$-x \delta k + t \delta E - \delta\phi \stackrel{!}{=} x \delta k - t \delta E + \delta\phi \quad (3.4)$$

$$x_{\text{scattered}} = t \frac{\delta E}{\delta k} - \frac{\delta\phi}{\delta k} = \left(t - \frac{\delta\phi}{\delta k} \frac{\delta k}{\delta E} \right) \delta E k = \left(t - \frac{\delta\phi}{\delta E} \right) \frac{\delta E}{\delta k}. \quad (3.5)$$

The time delay $\frac{\delta\phi}{\delta E}$, or advance if negative, of the scattered wave packet compared to the reference is then directly apparent from equations (3.2) and (3.5). It can be concluded that — in accordance with the group delay definition for ultrashort laser pulses — the EWS delay or advance caused by a potential variation is given by the derivative of the spectral phase difference caused by the potential.

$$\tau^{\text{EWS}}(E) = \frac{\partial}{\partial E} (\phi_{\text{scattered}}(E) - \phi_{\text{reference}}(E)) \quad (3.6)$$

Depending on the formulation of the exact problem, e.g., when superpositions of incoming and outgoing waves reflected off an infinite barrier are treated, an additional factor of 2 is used in the definition of the time delay. This difference is not repugnant to the presented but caused by using the eigenphase instead of the phase shift [33].

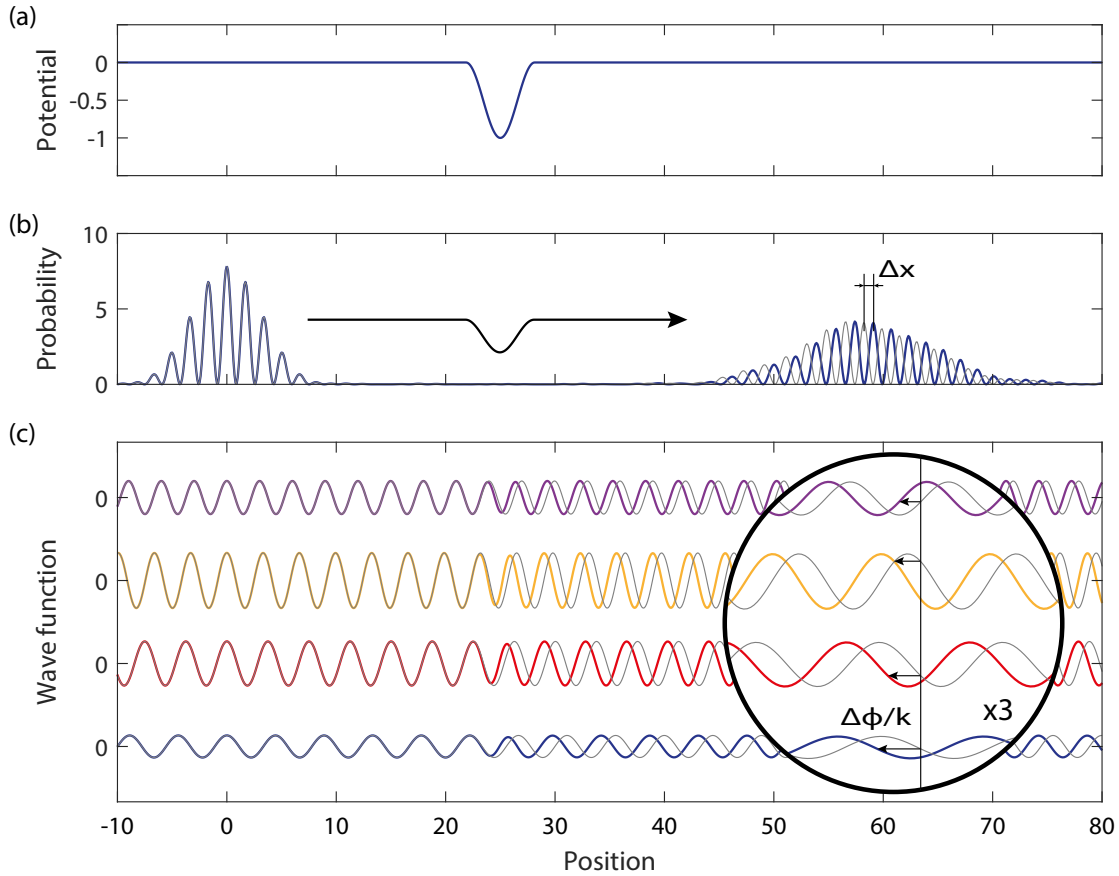


Figure 3.2: An electron wave packet train is experiencing a potential. Panel (a): potential landscape. Panel (b): electron wave packets created from 8 Eigenstates of the system, phases are chosen such that the train is compressed left of the potential ditch. When considering electrons traveling left to right, the scattered wave packet (blue) is spatially advanced by Δx compared to the reference wave packet (grey) after the potential. Panel (c): selected Eigenstates included in the scattered wave packet (colors) versus unscattered references (grey). The inset highlights the phase $\Delta\phi$ and spatial advance $\Delta\phi/k$ caused by the potential. k is the wave number.

3.3 Relating Photoemission and Scattering

Many of the properties developed for electron scattering can be applied to photoemission. The similarities and differences are illustrated in figure 3.3. In scattering, an incoming electron wave packet interacts with an atom or ion, which modifies its angular distribution and phase. For elastic scattering, the electron energy is conserved and hence defined only by the incoming wave packet. In photoemission, an incoming photon creates the wave packet close to the atom or ion it is absorbed by. Subsequently, the photoelectron escapes the potential around the now modified system, which defines the electron wave packet's angular distribution and phase combined with the incoming photon properties. The photoelectron's final energy is given by the difference of the photon energy and the ionization potential of the state the electron is freed from. Because the electron wave packet is already created around the atom or ion, it only samples one side of the potential. Therefore, photoemission can be described as a half-scattering event. The examined systems are mostly atoms, meaning the scatterer is usually an ion, which has significant implications due to its long-range Coulomb potential. These will be discussed in sections 3.4 and 4.2.4. Defining a delay for a time-dependent photoemission

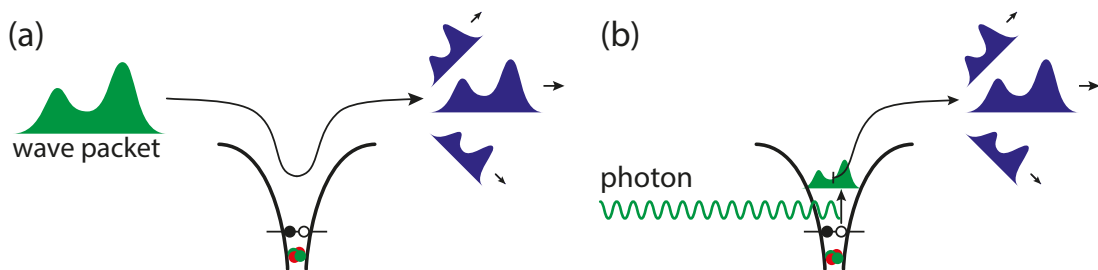


Figure 3.3: Elastic electron scattering versus photoemission. Panel (a): scattering. An incoming electron wave packet (green) experiences an (elastically scatters from an) arbitrary potential, in this case, caused by an ionic atom. The wave packet is observed far after the scattering event (blue), its phase and angular distribution depend on the potential. The kinetic energy of the electron far before and after the potential is equal. Panel (b): photoemission. A photon separates an electron from a neutral atom, creating an energetic electron wave packet and an ionic atom. The electron is freed close to the now ionic atom, at whose potential the electron can scatter. The ionic potential influences the final wave packet (blue) phase and angular distribution.

experiment is not as straightforward as for a scattering experiment because no incoming wave packet exists as a natural reference. Time-zero has to be defined by the incoming photon. Therefore, the reference is a virtual free electron wave packet created in the instant when the laser light pulse hits the examined atom. To be usable as a reference, its kinetic energy has to match the final, not initial, energy of the outgoing photoelectron. Figures 3.1 (b) and (d) illustrate the case in terms of the sled experiment: both our measurement and reference sleds are created at time-zero. The first starts in the ditch,

while the second starts on the bridge above it. The probe sled loses energy by escaping the ditch. Hence, it and the reference sled would have different final velocities if started with the same velocity, which makes the sleds' time difference position dependent. To record a defined delay, the reference sled's initial velocity must thus be chosen to match the measurement sled's final velocity. Only then the sleds co-propagate at a distance from the pit and the recorded time is unambiguous. This choice creates one of the main confusions arising from absolute photoemission delay measurements (gauged to the arrival time of the photon pulse): if only the time difference between the sleds at a distance from the ditch is observed and the landscape is assumed to be flat, it seems like the probe sled was started earlier than the reference. Transferring this fact to photoemission means that, under the assumption of a flat potential, the negative photoemission delay caused by an attractive potential seems like the photoelectron was created before the arrival of a photon, violating causality. However, this is not true, since it just evolved faster than our virtual reference packet due to its transiently higher energy. Therefore, negative photoemission delays do not automatically violate causality. There is an upper limit for their magnitude, which is discussed in the original paper by Wigner [30].

3.4 Photoemission Delays of Hydrogenic Systems

Up to this point, a central assumption of the discussion was a short ranged potential of the scatterer. This is, except for special cases such as singly charged negative ions, not the case in photoemission. Photoionization of a neutral system creates a positive ion, which is described by an attractive Coulomb potential. If the photoelectron does not interact with the electrons remaining at the photoion, photoemission from such a hydrogenic system into a partial wave with angular momentum l at large distance r from the parent ion with charge Z is phase shifted compared to a plane wave with the same asymptotic energy by [34, 35]

$$\Delta\phi^{\text{hydrogenic}}(r, k, l, Z) = \phi_{\text{scattered}}(r, k, l, Z) - \phi_{\text{plane wave}}(r, k) = -\frac{l\pi}{2} + \text{Im} \left[\ln \left[\Gamma \left(1 + l - i\frac{Z}{k} \right) \right] \right] + \frac{Z}{k} \ln(2kr), \quad (3.7)$$

in which Γ is the complex Gamma function. When calculating the EWS delay, the first term has no energy dependence, thus causes no delay. The second term is independent of r but changes with energy $E = \frac{k^2}{2}$, it causes a well-defined emission delay. However, the third term and its energy derivative diverge for large r , which prevents defining a proper delay due to the long range of the Coulomb potential, which the photoelectron never leaves. Therefore, it never stops acquiring phase compared to a free reference wave packet. The only possibility to remedy this is to switch to a reference that shows the same asymptotic phase behavior $\frac{Z}{k} \ln(2kr)$, not only the same asymptotic energy. Because the diverging term is universal for electrons with the same asymptotic kinetic energy and parent ions with equal charge Z , switching to this specific reference does not limit generality or comparability. For the rest of the thesis, the EWS delay will hence be

defined for all systems as

$$\tau_{\text{Coulomb}}^{\text{EWS}}(E, p_1, p_2, \dots) = \frac{\partial}{\partial E} \left(\phi_{\text{scattered}}(r, E, p_1, p_2, \dots) - \phi_{\text{plane wave}}(r, E) - \frac{Z}{\sqrt{2E}} \ln(r\sqrt{8E}) \right), \quad (3.8)$$

which eliminates the diverging term and the location dependence in equation (3.7). Consequently, this definition of the EWS delay excludes the infinite-range contributions of the Coulomb potential but focuses on the phase that builds up in the vicinity of the parent ion. This definition is also advantageous because the system-specific photoemission delay is isolated from the commonly uniform and dominating Coulomb delay. In many cases, the EWS delay does not only depend on the photoelectron energy but also on other parameters p_1, p_2, \dots , e.g., the initial state, emission angle or ionization state. The EWS delay for photoemission from a hydrogenic system in this notion is given by

$$\tau_{\text{Hydrogenic}}^{\text{EWS}}(E, l, Z) = \frac{\partial}{\partial E} \left(\text{Im} \left[\ln \left[\Gamma \left(1 + l - i \frac{Z}{\sqrt{2E}} \right) \right] \right] \right). \quad (3.9)$$

For a known electron kinetic energy and partial wave, the hydrogenic delay provides a ballpark estimate even for more complex atoms, results for $Z = 1$ and $l = 0 \dots 5$ are plotted in figure 3.4. Deviations occur in the proximity of resonances when the local potential shows substantial structure, e.g., in the angle-resolved photoemission from molecules, or if the Coulomb repulsion between electrons in multi-electron systems has a significant influence on the exit channel.

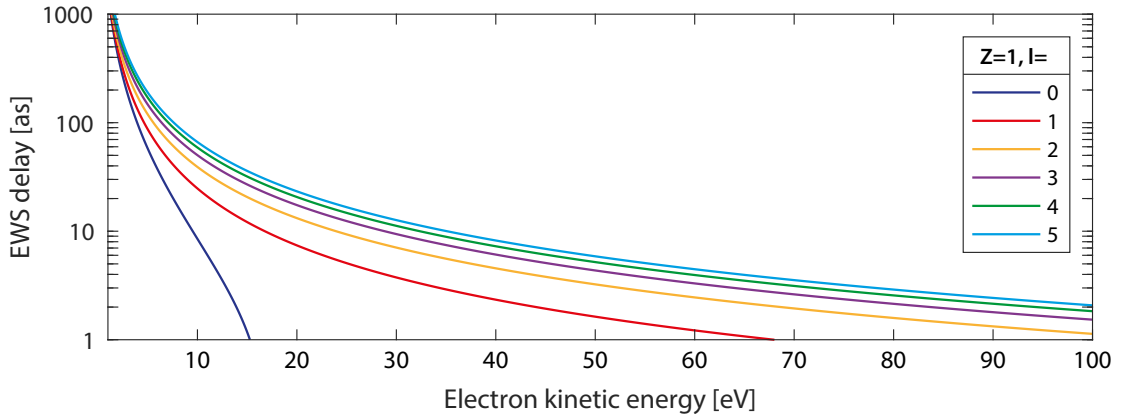


Figure 3.4: Eisenbud-Wigner-Smith (EWS) delay for photoemission into different partial waves l from a neutral hydrogenic system that has charge $Z = 1$ after photoemission.

Chapter 4

Photoelectron Timing Measurement

The typical magnitude of a photoemission delay is on the order of a few to several hundred attoseconds. Therefore, its direct observation requires time resolutions in the attosecond domain, which are currently only attainable by a handful of techniques. Two versatile methods for the timing of photoelectrons are the reconstruction of attosecond beating by interference of two-photon transitions (RABBITT) [36] and the attosecond streak camera [27]. Relative delays in photoemission can also be examined using interferences in non-time-resolved measurements [37, 38]. However, these interferences have to be present in the sample and cannot be externally enforced, limiting the generality of this method compared to time-resolved techniques. This thesis is based on measurements using the attosecond streak camera, whose requirements, concept and theory will be discussed in the following. Because of their similar nature, the quantum description of streaking is directly applicable to RABBITT measurements.

4.1 Attosecond Pulse Generation

To perform a photoemission delay measurement, the attosecond streak camera relies on two light pulses, an extreme-ultraviolet (XUV) attosecond pulse triggering photoemission and a visible (VIS) to near-infrared (NIR) light pulse to probe the photoelectron wave packet. So far, the only technique providing XUV attosecond pulses reproducibly enough to be used as a source in timing measurements is high-harmonic generation. Consequently, both, attosecond streaking and RABBITT rely on this method. In high-harmonic generation, a high photon energy pulse train with attosecond sub-structure is created from an intense VIS or NIR driving laser pulse. The technique has the advantage that the latter can be repurposed as an intrinsically synchronized streaking field in the experiment. High-harmonic generation is a vast and active field of research, hence only the basic concepts relevant to this thesis can be introduced.

4.1.1 Generation of Attosecond Pulse Trains

When focusing an intense ultrashort laser pulse into a gas target, the spectrum after the target can contain frequencies reaching up to a few hundred times the initial photon energy [39–41]. The mechanism responsible for those new frequencies is high-harmonic generation, which is an extremely nonlinear process that cannot be described in the perturbation theory nonlinear optics framework, e.g., used for second harmonic generation. It

can be conceptualized using the semiclassical *three-step model* [42, 43], which is illustrated in figure 4.1: focused short laser pulses can reach field strengths that significantly alter the atomic binding potential for electrons. At a field crest, this leads to a reduction of the potential barrier, increasing the possibility for valence electrons to tunnel out of the atom. Once this process occurs, the now free electron finds itself in an intense electric field, which accelerates the electron until the field reverses. The electron is then decelerated and accelerated back towards its parent ion. When the electron passes its parent ion, it can recollide and release its energy as a single photon. This photon's energy is given by the kinetic energy $E_{\text{kin}}^{\text{recollision}}$ acquired in the field until recollision and the ionization potential IP of the atom.

The recollision process can be understood when acknowledging that not the whole electron, but merely a small part of it tunnels and is accelerated, while its majority stays in the bound state at the atom. When the continuum wave packet part returns and overlaps with the coherent bound fraction of the electron, their beating creates a rapidly changing dipole oscillating at the difference frequency $E_{\text{xuv}} = E_{\text{dipole}} = E_{\text{kin}}^{\text{recollision}} - (-IP)$, which emits the harmonic radiation.

Because the tunneling probability is only considerable around field crests, possible recollision times follow their time structure. Hence, the emitted train consists of short, energetic light pulses that are spaced at twice the driving laser's cycle time or twice its photon energy in the frequency domain. For VIS or NIR driving laser pulses, an individual pulse's duration is in the attosecond regime, molding the name attosecond pulse train.

Figure 4.2 compares classical electron trajectories in the driving laser field. For a continuous wave driver, the electron trajectories recolliding with maximum kinetic energy start 0.05 laser cycles after a field crest and recollide with the parent atom 0.65 cycles later. Calculating the kinetic energy gained during that time in the field allows to estimate the cutoff energy, i.e., the highest reachable photon energy in the process [43]:

$$E_{\text{xuv}}^{\text{cutoff}} = E_{\text{kin}}^{\text{recollision}} - (-IP) = IP + 3.17U_p \quad \text{with} \quad U_p = \frac{(E_{\text{laser}}^{\text{max}})^2}{4\omega_{\text{laser}}^2} \quad (4.1)$$

The ponderomotive potential U_p is the average kinetic energy of a free electron oscillated by a continuous wave electric field with amplitude $E_{\text{laser}}^{\text{max}}$ and carrier frequency ω_{laser} . The maximum attainable high-harmonic photon energy is defined by the used target via its ionization potential and the driving laser field amplitude and frequency. Larger driving laser wavelengths can reach higher cutoff energies due to a longer acceleration time.

4.1.2 Isolation of Individual Attosecond Pulses

Current femtosecond laser systems can produce light pulses containing only two optical oscillations within their intensity full-width-at-half-maximum (FWHM). With specially designed chirped mirror compressors, even single or sub-cycle pulses can be created [45]. To illustrate the implications for the high-harmonic creation process, figure 4.2 compares a continuous wave driver with short laser pulses containing 1.8 and 1.1 light oscillation cycles.

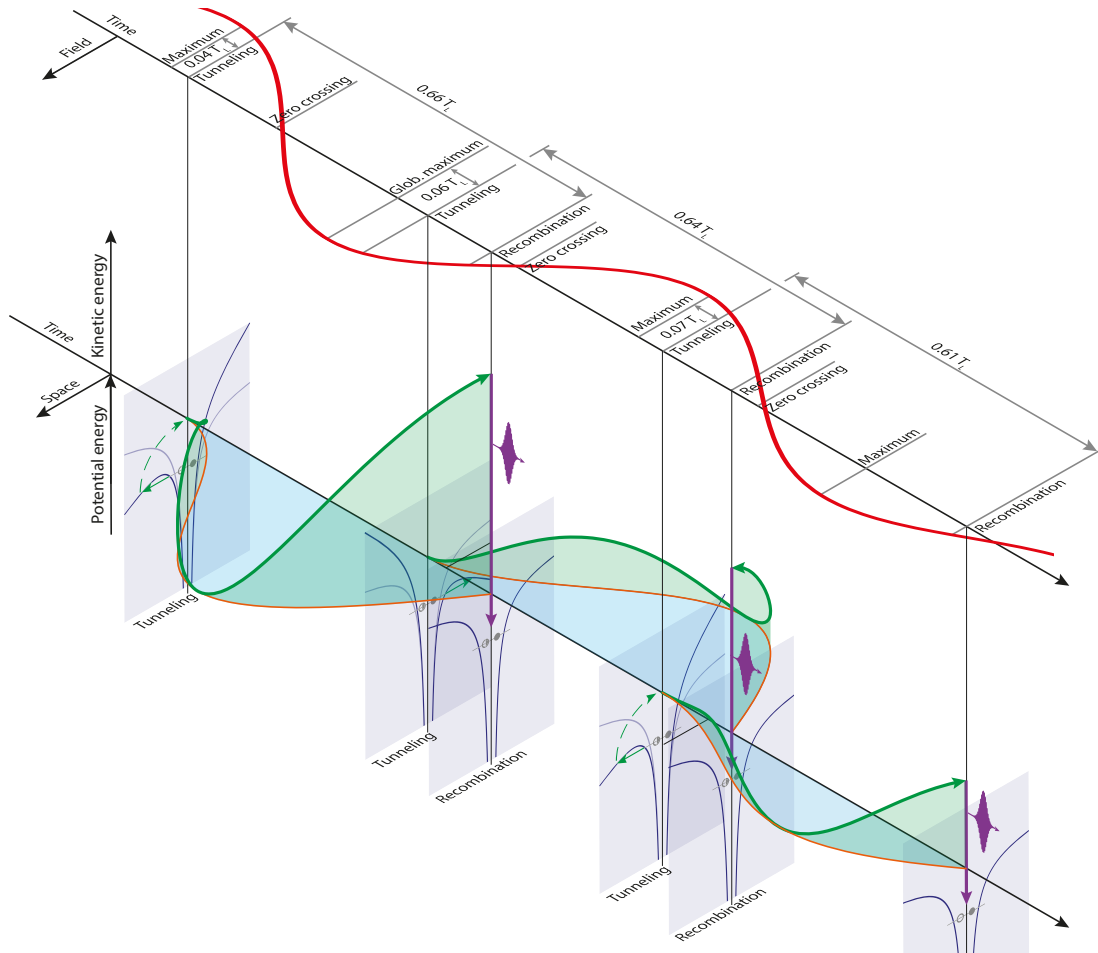


Figure 4.1: Three-step model for high-harmonic generation from a gas atom. The intense driving laser electric field (red) distorts the atomic binding potential (dark vs. light blue lines indicate the distorted and undistorted potentials at selected times) such that valence electron tunnel escape is possible near field crests. In case of a tunnel exit, the electron is assumed to start at zero kinetic energy and the atom's position (green dashed arrow) and is then accelerated by the laser electric field. There are three prevalent electron emission times during a 1.8 cycle cosine pulse, see figure 4.2. For each emission, the trajectory in the position-kinetic energy space which recollides with maximum kinetic energy is plotted in green, its projection to position space is plotted in orange. When the electron returns to its parent ion, there is a chance for recollision, which releases the potential and kinetic energy as an energetic photon (purple). Only the first electron emission contributes to the cutoff energy photons. Time is measured in units of the driving laser period T_L .

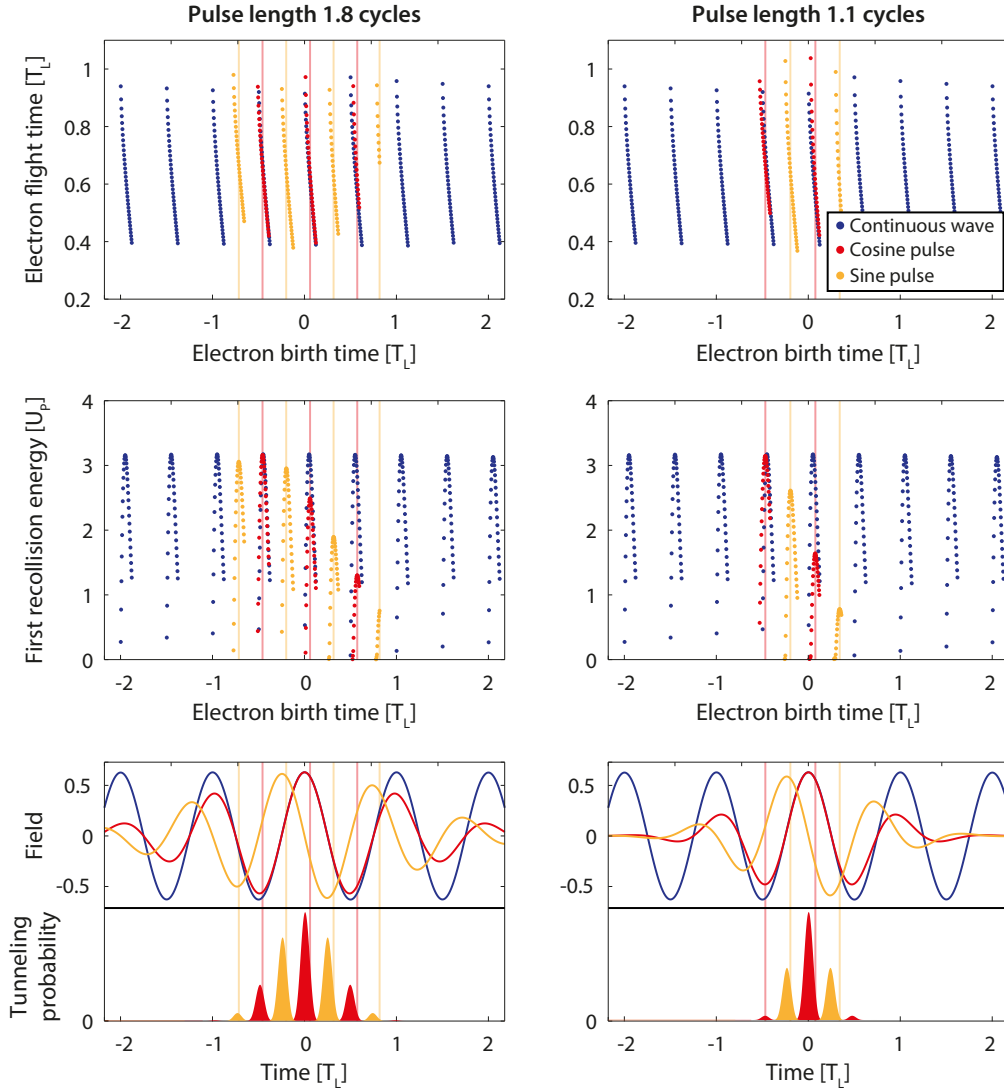


Figure 4.2: Classical electron trajectories during high-harmonic generation from a continuous wave and short cosine and sine laser pulses. All electric fields share the same envelope amplitude. Vertical lines link the emission times of the maximum kinetic energy recollision (in units of the ponderomotive potential U_p) trajectories with their position in the driving electric field and their flight time. The ionization probability cannot be estimated as generally as the trajectories. Only electrons escaping at intensities above half the maximum intensity are shown to exclude improbable tunneling times crudely. The depicted tunneling probabilities are estimated using the Ammosov–Delone–Krainov formula [44] for neon and $\sim 6 \text{ V/\AA}$ field amplitude (corresponding to a cosine pulse maximum intensity of $\sim 1 \times 10^{15} \text{ W/cm}^2$). The cutoff energy reached by an 800 nm wavelength driver laser in this particular case is $\sim 115 \text{ eV}$.

For a 1.8 cycle laser pulse, the cutoff energy does not deviate significantly from the continuous wave case. However, only one or two cycles contribute to the cutoff photon energy emission, depending on the CEP. This fact means that an isolated attosecond pulse can be synthesized by generating high-harmonics from a cosine pulse and spectrally selecting the cutoff photons using a filter, a technique known as *intensity gating* [46]. Due to its two equally high field maxima, a sine pulse of equal duration produces two cutoff energy attosecond bursts. Thus, CEP stabilization is required when using intensity gating [47]. The picture changes for even shorter pulses, illustrated in the right panels of figure 4.2: for a 1.1 cycle cosine pulse, the tunnel exit probability of the cutoff trajectories is suppressed, preventing efficient generation of cutoff harmonics. Therefore, sine pulses have to be used when approaching the single-cycle limit. A 1.1 cycle sine pulse now creates an isolated attosecond pulse at high photon energies because the tunneling probability is only significant during the two field maxima and the second electron wave packet is not efficiently accelerated. Although the cutoff photon energy is reduced compared to the 1.8 cycle pulse, the maximum energy contrast of the two consecutive electron bursts is better for the shorter than for the longer pulse, allowing to create shorter attosecond pulses. While all driving pulses at this duration now generate single attosecond pulses at the cutoff energy, CEP stabilization is still necessary for flux and stability. Especially for the attosecond streak camera it is a must since it relies on sampling a reproducible light waveform.

4.1.3 Phase Matching

So far, only the single-atom response to an intense driving laser pulse was treated to explain high-harmonic generation. In this picture, arbitrarily high photon energies can be generated by increasing the driving laser intensity. For using high-harmonics as an experimental radiation source in the XUV, many emitters have to be combined in order to reach usable conversion efficiencies [48]. As for most nonlinear processes, phase matching, i.e., coherently overlapping the emission over the whole interaction region, plays a major role because the generating and generated frequencies are extremely different [49]. In gas phase high-harmonic generation, phase matching is achieved by balancing the refractive index of the neutral medium and the negative contribution of the generated plasma. This balancing is achieved by varying the gas density and laser intensity to optimize the flux of generated high-harmonic radiation in the desired energy window. More elaborate schemes were proposed but are not routinely used yet [50]. Precisely predicting phase matching conditions is cumbersome due to the extreme nonlinearity of the tunneling process and spatial effects [51]. For uniform plane waves in the target area, an optimal ionization fraction η_{opt} can be calculated from the refractive index difference $\Delta n(\lambda_{\text{laser}}, \lambda_{\text{xuv}})$ of the generating medium at atmospheric pressure, its number density $N_{\text{atm.}}$ at atmospheric pressure and the classical electron radius r_e using equation (4.2) [50].

$$\eta_{\text{opt}} = \left(1 + \frac{N_{\text{atm.}} r_e \lambda_{\text{laser}}^2}{2\pi \Delta n} \right)^{-1} \quad (4.2)$$

$$\begin{aligned}\Delta n(\lambda_{\text{laser}}, \lambda_{\text{xuv}}) &= n(\lambda_{\text{laser}}) - n(\lambda_{\text{xuv}}) \\ &\approx n(\lambda_{\text{laser}}) - 1 \quad (\text{far from resonances})\end{aligned}$$

For an 800 nm wavelength driving laser pulse, the optimal ionization fraction is roughly 0.5 % for helium, 1 % for neon and 5 % for argon [50]. At this optimal ionization fraction, no phase shift occurs between the driver and the generated XUV radiation, allowing efficient build-up of high-harmonics to up to the absorption length of the XUV in the gas target. The existence of an optimal ionization fraction, depending only on the generating species but no macroscopic quantity, has severe consequences for the maximum reachable XUV photon energies: Because the ionization fraction is mainly generated via nonlinear tunnel ionization, phase matching collapses quickly above the optimal ionization fraction due to excessive plasma creation. At the same time, the cutoff energy increases linearly with the laser intensity, i.e., grows only marginally above the phase matching condition while the achievable flux suffers disproportionately. Effectively, for a given driver wavelength, the maximum cutoff energy is limited by the phase matching condition of the generating medium. Switching the medium is a possible way to raise the cutoff energy, however raising the ionization potential above that of helium requires the use of positive ions, which is experimentally cumbersome. Therefore, the only scalable way to increase the cutoff energy is to enlarge the driving laser wavelength. This comes at the cost that the longer electron excursion decreases the chance for recollision due to diffusion of the continuum electron wave packet. The conversion efficiency scales roughly with λ^{-6} [52, 53]. Thus, extreme target pressures, high laser fluences, and large generation volumes are necessary when pushing for long wavelength drivers.

4.2 The Attosecond Streak Camera

The streak camera concept uses a temporally rapidly varying electric field to map electronically unresolvable time structures of electron wave packets to a detectable momentum variation. Conventional streak cameras are used to measure the structure of picosecond laser pulses. For this purpose, electron wave packets copying the light pulses' structure are created in a photocathode. These are accelerated and propagate through a plate capacitor, which applies a temporally changing electric field perpendicular to the electrons' propagation direction [54]. The resulting transverse momentum distribution is recorded as spatial shift on a screen and allows to retrieve the electrons' time structure, which corresponds to the creating picosecond pulses' envelope. The temporal resolution is mainly limited by the rate at which the measurement field can be modulated. The attosecond streak camera was developed to determine the pulse structure of attosecond XUV light pulses [27]. A hundred-thousandfold resolution increase is achieved by switching from an electronically created measurement field to a controlled optical waveform, which is naturally oscillating with frequencies up to a Petahertz.

The prototypical experimental setup is illustrated in figure 4.3. After generating an attosecond pulse train using high-harmonic generation, the XUV and laser radiation are split using their differing divergences. An attosecond pulse is then created by spectrally

selecting the cutoff photons using metal foils and multilayer optics. The attosecond pulse and the laser pulse are then delayed, recombined and focused into the streaking target, which can be solid, liquid or gaseous. These steps can, but do not have to, be combined using a focusing annular double mirror assembly, which reflects XUV radiation from a movable center and the streaking laser field on the outer part. Photoelectrons created in the streaking target by the XUV radiation are recorded using a time-of-flight detector, which allows recording their complete energy spectrum without scanning. A description of the employed measurement setups with references to literature by the designing scientists is found in appendix B.

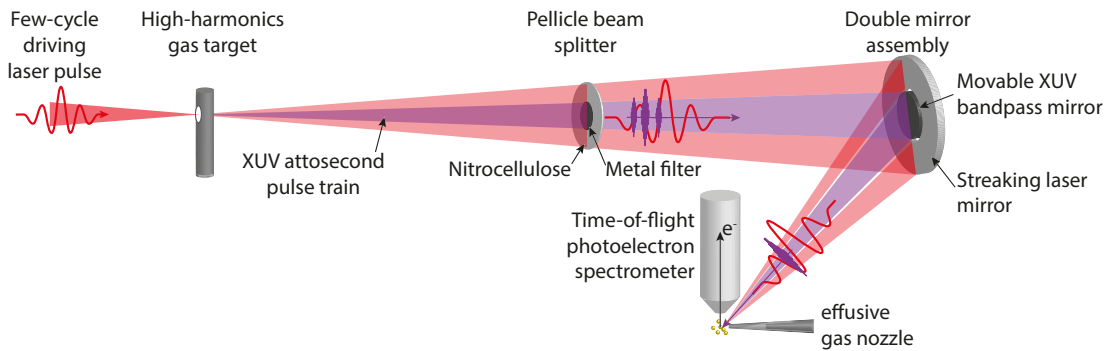


Figure 4.3: Exemplary streak camera setup. A CEP stabilized few-cycle laser pulse is focused into a gas target. The nonlinear interaction of the laser pulse with the gas atoms creates a train of extreme-ultraviolet (XUV) attosecond pulses via high-harmonic generation. Using the smaller divergence of the XUV, the driving laser and XUV radiation are split by an annular filter, which transmits XUV at its center and the driving laser on the outside. A double mirror assembly with the same annular structure is then employed to isolate a single attosecond pulse by spectrally filtering the XUV cutoff photons, introduce a relative delay between the two pulses and focus them into the streaking target. In the examined sample, the XUV attosecond pulse creates photoelectrons which are energy-modulated according to their moment of creation by the laser pulse and detected using a time-of-flight spectrometer.

The measurement happening at the streaking target is outlined in figure 4.4. An unknown attosecond pulse and an optical test field are co-propagating for the measurement. The XUV pulse creates a photoelectron wave packet from an atom that inherits its time structure. From the instant when the electron can be regarded as charged free particle, the optical test field *streaks* the photoelectron, i.e., exerts a force changing the photoelectron's final momentum distribution according to its time of release. The resultant photoelectron spectra are recorded for different time delays between the examined pulse and test field, resulting in a spectrogram which contains the time structure of both involved pulses.

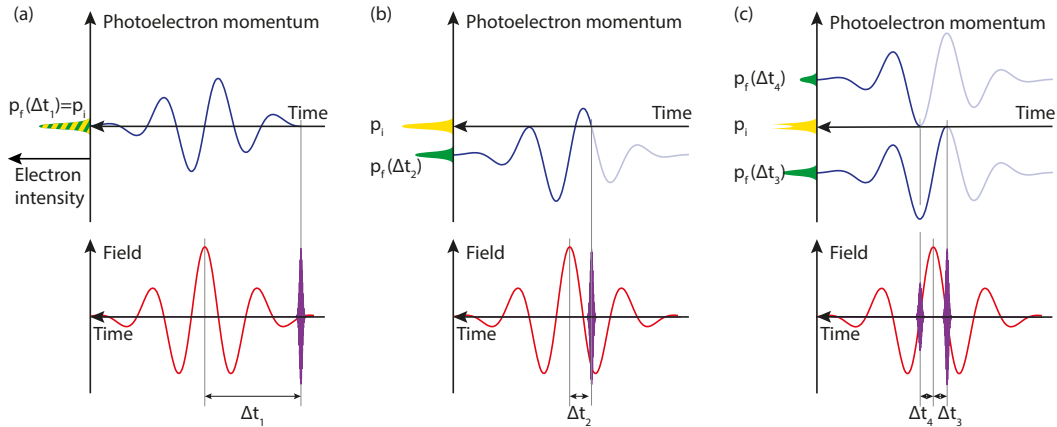


Figure 4.4: Streak camera concept. A waveform controlled visible (VIS) or near-infrared (NIR) (red) and XUV (purple) light pulse impinge on an atom (not shown). The XUV pulse photoionizes the atom and creates a continuum electron wave packet with an initial momentum distribution (yellow) centered around an initial momentum p_i . Panel (a): the XUV pulse arrives before the streaking laser pulse. The electron feels a force due to the streaking electric field: its momentum change follows the negative streaking pulse vector potential (blue). The alternating current nature of light results in no net momentum shift, thus the final momentum distribution (green) p_f is unchanged. Panel (b): the pulses overlap. Photoelectrons only feel part of the streaking laser field (dark blue vs. light blue momentum evolution), allowing finite shifts of the final momentum distribution. Temporal substructure in the XUV pulse is resolved by a smeared final momentum distribution. Panel (c): multiple XUV pulses cause modulations in the initial spectrum due to interference. These allow to extract the temporal pulse spacing but are not sufficient to distinguish if two or more pulses are present. The streak camera lifts the energetic overlap of pulse components with equal instantaneous frequency occurring at different times during a pulse train and therefore allows retrieving not only the spacing but also the number and intensity ratio of the pulses.

4.2.1 Classical Description

The fundamental concept of the attosecond streak camera is grasped by classical equations of motion, as long as isolated attosecond pulses, whose duration is shorter than a quarter of the measurement waveform laser period T_{laser} , are employed. Due to the benefit for conceivability, this picture will be introduced before switching to a more coherent quantum description, which is also able to describe the interferences arising when experimenting with attosecond pulse trains or longer attosecond pulses.

An XUV attosecond pulse with central photon angular frequency ω_{xuv} can ionize matter and create free electrons with initial momentum $|\vec{\mathbf{p}}_i| = \sqrt{2(\omega_{\text{xuv}} - IP)}$, where IP is the ionization potential of the used target atoms. Assuming these are instantaneously placed into the streaking laser field $\vec{\mathbf{E}}_{\text{laser}}$ at the attosecond pulse's temporal center, the asymptotic electron momentum $\vec{\mathbf{p}}_f$ is given by the integrated force the streaking field exerts on the electron from this instant until the streaking laser field has passed. For a delay Δt between the attosecond pulse and the streaking laser field, $\vec{\mathbf{p}}_f$ is given by [55]:

$$\frac{d\vec{\mathbf{p}}(t')}{dt'} = \vec{\mathbf{F}}(t') = -\vec{\mathbf{E}}_{\text{laser}}(t') \quad (4.3)$$

$$\vec{\mathbf{p}}_f(\Delta t) = \vec{\mathbf{p}}_i - \int_{\Delta t}^{\infty} \vec{\mathbf{E}}_{\text{laser}}(t') dt' = \vec{\mathbf{p}}_i - \vec{\mathbf{A}}_{\text{laser}}(\Delta t) \quad (4.4)$$

$$\vec{\mathbf{A}}_{\text{laser}}(\Delta t) \stackrel{!}{=} \int_{\Delta t}^{\infty} \vec{\mathbf{E}}_{\text{laser}}(t') dt' \quad (4.5)$$

The momentum distribution change induced by the streaking field coincides with its vector potential in the Coulomb-length gauge $\vec{\mathbf{A}}_{\text{laser}}$. The term vector potential is used in the following for brevity. However, it has to be regarded that equation (4.4) is not gauge invariant, i.e., $\vec{\mathbf{A}}_{\text{laser}}$ is not a real vector potential. Due to relation (4.4), the electron movement in momentum space can be visualized by overlapping the streaking laser vector potential at time Δt and the initial electron momentum, which results in the blue lines in figure 4.4. Vice versa, the streaking laser vector potential at time Δt can be directly extracted from the asymptotic momentum modification. The resulting kinetic energy modulation is most prominent when detecting electrons along the streaking laser polarization axis but affects all ejected electrons. In the case of electron detection perpendicular to the laser polarization, the mechanism changes from detecting a delay-dependent momentum shift for electrons emitted into the detector to bending the electron trajectories such that different electrons are reaching the detector with each delay step [46]. Their projected final momentum is decreased by the streaking field with twice its oscillation period. The spectrogram is therefore ambiguous about the CEP of the streaking laser field. The further discussion will focus on electrons detected in the streaking polarization direction, which is the most frequently used experimental geometry.

To extract the XUV pulse shape, we focus on a fixed delay between the XUV pulse center and the streaking field. The envelope of a finitely long but compressed XUV pulse (which has no photon energy sweep across its duration) is projected to a momentum sweep, i.e., a spectral broadening because the streaking field varies over its duration.

To first order, the sweep is linear to the streaking laser's vector potential slope at the overlap time Δt :

$$p_f(t) = p_i - A_{\text{laser}}(t) \approx p_i - t \left. \frac{\partial A(t')}{\partial t'} \right|_{t'=\Delta t} \quad (4.6)$$

For a compressed XUV pulse and known slope, the attosecond pulse duration is hence directly related to the recorded sweep. The broadening is maximal at the zero crossings of the streaking vector potential, i.e., where the streaking field is maximal. However, a compressed pulse's duration can more easily be inferred from its spectrum via Fourier transformation.

To examine if the attosecond pulse is compressed, we consider two adjacent zero crossings of the streaking vector potential. A linearly chirped XUV pulse creates an initial electron momentum distribution $p_i(t) = \sqrt{2(\omega_{\text{xuv}} + \beta_{\text{xuv}}t - IP)}$ that is also time-dependent. The broadening then depends on the signs of the chirp β_{xuv} and the slope of the streaking vector potential [56]:

$$p_f(t) = p_i(t) - A_{\text{laser}}(t) \approx p_i(0) + t \frac{\beta_{\text{xuv}}}{p_i(0)} - t \left. \frac{\partial A(t')}{\partial t'} \right|_{t'=\Delta t} \quad (4.7)$$

If chirp and streaking vector potential gradient have opposite signs, the electron momentum distribution is spectrally broadened more than in the compressed case. If they share the same sign, their effects cancel, and the distribution is narrowed. By comparing the broadening and narrowing in adjacent zero crossings of the streaking vector potential, we can hence evaluate if an XUV attosecond pulse is chirped or compressed and thus also its duration. Figure 4.5 illustrates the broadening of a compressed, a positively and a negatively chirped pulse.

4.2.2 Quantum Mechanical Description

A complete picture can be gained from quantum mechanical considerations. The observable in attosecond streaking spectroscopy is a photoelectron spectrum, i.e., the asymptotic spectral properties of a photoelectron wave packet $\psi(t)$ created by an XUV pulse. Using continuum Eigenstates $|p_f\rangle$ of the system with asymptotic momentum p_f at the electron detector, the photoelectron spectrum is given by $S(p_f) = |\langle p_f | \psi(t) \rangle|^2$. In the strong-field approximation, which ignores the parent ion, the final states are plane wave states. Continuum Eigenstates of a Hamiltonian including the Coulomb potential would be a more realistic choice [57, 58]. In first-order perturbation theory and the dipole and rotating wave approximation, $\langle p_f | \psi(t) \rangle$ is determined by the product of the transition matrix element $\tilde{D}(p_f)$, the attosecond pulse's complex spectral field \tilde{E}_{xuv} and a delta function enforcing energy conservation [58, 59]:

$$\begin{aligned} S(p_f) &= |\langle p_f | \psi(t) \rangle|^2 \propto \left| \int_{-\infty}^{\infty} d\omega_{\text{xuv}} \tilde{D}(p_f) \tilde{E}_{\text{xuv}}(\omega_{\text{xuv}}) \delta(\omega_{\text{xuv}} - (p_f^2/2 + IP)) \right|^2 \\ &= \left| \tilde{D}(p_f) \tilde{E}_{\text{xuv}}(p_f^2/2 + IP) \right|^2 \end{aligned} \quad (4.8)$$

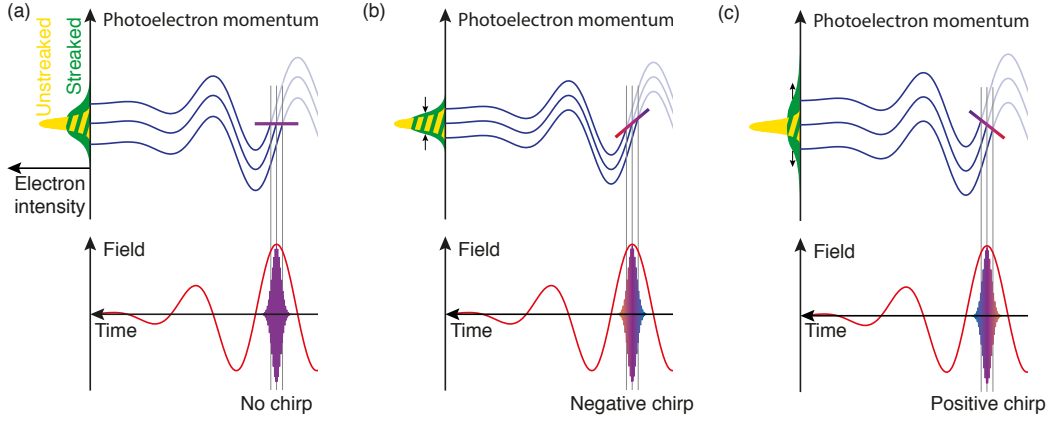


Figure 4.5: Streaking of compressed and chirped attosecond pulses. Panel (a): an electron wave packet created by a compressed attosecond pulse with finite duration is spectrally broadened when overlapping with a maximum of the streaking field because the streaking shift is time-dependent. Panels (b) and (c): a chirped pulse creates a chirped electron wave packet. This energy sweep is added to the time-dependent streaking shift. Therefore, the electron wave packet is either broadened or narrowed compared to a compressed wave packet. Which process happens, depends on the attosecond pulse chirp and zero crossing slope sign, resulting in a recognizable pattern in the streaking spectrogram, for example see figure 4.6

Vice versa, the final electron energy is defined by the ionization potential IP of the initial state and the angular frequency of the XUV pulse ω_{xuv} . The transition matrix element depends on the overlap and phase of the initial state $|i\rangle$ and the final state $|p_f\rangle$. It is complex valued and contains the photoemission delay and dispersion. Therefore, neither the amplitude nor the phase of the electron wave packet depends solely on the attosecond pulse. Further on, only streaking from one initial state will be treated, the transition matrix element will thus only be marked by the final state's momentum p .

To treat streaking, we switch to the time domain by using the Fourier transform of the complex spectral attosecond pulse envelope:

$$\begin{aligned} \tilde{E}_{\text{xuv}}(p_f^2/2 + IP) &= \int_{-\infty}^{\infty} dt \tilde{E}_{\text{xuv}}(t) e^{it(p_f^2/2 + IP)} \rightarrow \\ S(p_f) &\propto \left| \int_{-\infty}^{\infty} dt \tilde{E}_{\text{xuv}}(t) \tilde{D}(p_f) e^{it(p_f^2/2 + IP)} \right|^2 \end{aligned} \quad (4.9)$$

By adding a streaking laser field described by the vector potential $A_{\text{laser}}(t)$ and delayed with respect to the XUV pulse by Δt , the initial continuum state and asymptotic continuum state differ due to the introduced momentum shift. The correct transition matrix element for an asymptotic momentum p_f is hence that to the continuum state before streaking, $\tilde{D}(p_f + A_{\text{laser}}(t))$. Additionally, the phase evolution of the free electron

wave packet is modified by the streaking field. The additional phase accumulated by a free electron in an electric field is called the Volkov-Phase, which is given by equation (4.10). The electron momentum spectrum including x-ray photoemission and streaking can be evaluated from equation (4.11). In x-ray photoelectron spectroscopy, often the energy spectrum is evaluated, which is straightforwardly calculated using equation (4.11) and $E_{\text{kin}} = p_f^2/2$:

$$\phi_V(p_f, t) = - \int_t^\infty dt' \left(p_f A_{\text{laser}}(t') + \frac{1}{2} A_{\text{laser}}^2(t') \right) \quad (4.10)$$

$$S(p_f, \Delta t) \propto \left| \int_{-\infty}^\infty dt \tilde{E}_{\text{XUV}}(t + \Delta t) \tilde{D}(p_f + A_{\text{laser}}(t)) e^{i\phi_V(p_f, t)} e^{it(p_f^2/2 + IP)} \right|^2 \quad (4.11)$$

Equation (4.11) can be used to simulate the impact of different pulse parameters on streaking spectrograms. Figure 4.6 illustrates the broadening due to streaking an attosecond pulse of finite duration. A compressed attosecond pulse is equally broadened in rising and falling zero crossings of the vector potential. A chirped attosecond pulse shows a distinct broadening and narrowing, depending on the sign of the slope of the zero crossing and the attosecond pulse chirp. In contrast to the classical treatment, also attosecond pulse trains can be treated. For these, the streaking pattern disappears and is replaced by oscillating sidebands, which are typical for RABBITT experiments.

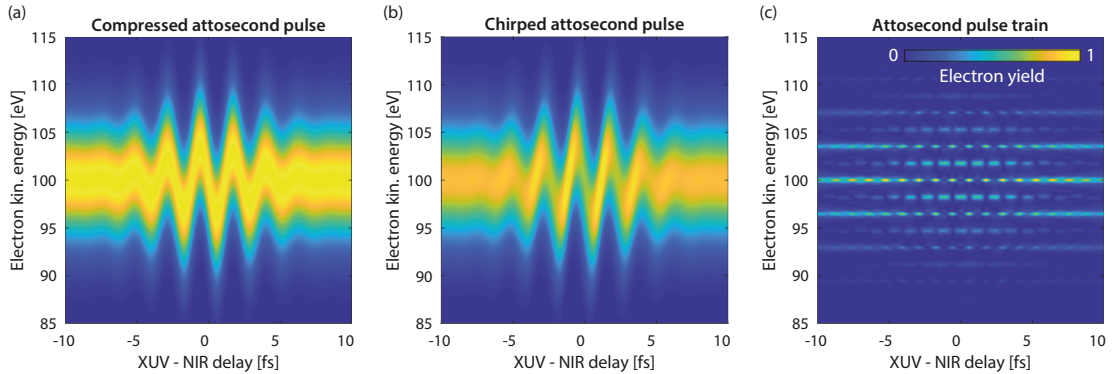


Figure 4.6: Streak camera simulations employing different XUV attosecond pulses but equal streaking laser fields. Panel (a): a compressed XUV pulse. Panel (b): an XUV pulse with 20 as/eV group delay dispersion. Panel (c): a train of attosecond pulses spaced with $T_{\text{laser}}/2$. The streak pattern is replaced by reconstruction of attosecond beating by interference of two-photon transitions (RABBITT) sidebands.

The terms in equation (4.11) can be conceptualized when re-writing and interpreting as integral over all possible excitation paths [59]: The weight of a path is given by the transition matrix element and the XUV amplitude at the excitation time. The phase of a path is given by the transition phase and two additional parts, the phase accumulated in the bound state until excitation and subsequently the phase accumulated as a free

electron in the streaking field. The time evolution of the bound electron is given by

$$e^{-i \int_{-\infty}^t dt' (-IP)} = e^{i(IPt - \text{const.})}. \quad (4.12)$$

Using a velocity gauge Hamiltonian, the free electron time evolution is described by

$$e^{-i \int_t^\infty dt' \frac{1}{2} (p_f + A_{\text{laser}})^2} = e^{-i \left(-\frac{1}{2} p_f^2 t + \text{const.} + \int_t^\infty dt' \left(p_f A_{\text{laser}}(t') + \frac{1}{2} A_{\text{laser}}^2(t') \right) \right)}. \quad (4.13)$$

The constant phase terms are equal for all paths and can be dropped, resulting in:

$$S(p_f, \Delta t) \propto \left| \int_{-\infty}^{\infty} dt \underbrace{\tilde{E}_{\text{XUV}}(t + \Delta t) \tilde{D}(p_f + A_{\text{laser}}(t))}_{\text{transition probability and phase}} \times \underbrace{e^{-i \left(-\frac{1}{2} p_f^2 t + \int_t^\infty dt' \left(p_f A_{\text{laser}}(t') + \frac{1}{2} A_{\text{laser}}^2(t') \right) \right)}}_{\text{free electron phase}} \underbrace{e^{iIPt}}_{\text{bound electron phase}} \right|^2 \quad (4.14)$$

4.2.3 Photoemission Delay Retrieval

Both, experiment and advanced theoretical modeling do not directly reveal photoemission delays. Instead, the result of an attosecond streaking experiment is a spectrogram, i.e., multiple electron energy spectra recorded for differing time delays between the attosecond pump and the probe pulse. The photoemission delay appears in these spectrograms as a shift of the streaking modulation along the pulse delay axis, because the electron starts the streaking process at a different time than if it was placed into the streaking field instantly. Due to the small magnitude of this shift, it is hardly discernible by eye. Therefore, specialized retrieval algorithms are used to extract pulse properties and emission delays from spectrograms. Three retrieval algorithms with different strengths were developed to attain the presented results. In the course of this thesis, all were implemented in an end-user tool, which is currently used by multiple groups for the evaluation of streaking spectrograms. Due to the technical nature, only the individual strengths of these algorithms will be introduced here, while detailed information can be found in appendix A.

Center-of-Energy Retrieval

The *center-of-energy* (COE) retrieval calculates the energy first moment of the photoelectron spectra recorded for each pulse to pulse delay in a spectrogram. The resulting energy modulation and equation (4.4) allow retrieving the streaking laser field directly. If multiple photoemission lines are compared, the relative time shift between the extracted streaking laser fields yields the photoemission delay. Its main advantage is the speed of retrieval, but the algorithm provides no information about the attosecond XUV pulse.

Restricted Time-Dependent Schrödinger Equation Retrieval

The *restricted time-dependent Schrödinger equation (TDSE) retrieval* fits an approximated equation (4.11) to a spectrogram in its full dimensionality. In the fitting process, the streaking field and the electron wave packets are characterized by a Gaussian envelope and linear group delay dispersion. Furthermore, the photoemission peak energies and amplitudes are restricted to match synchrotron data. Constricting the fitted fields and features leads to a robust retrieval, even in the presence of experimental noise, which made it the primary algorithm used in this research. Another useful property is the weighting introduced by this algorithm when different photoemission features overlap spectrally. Such overlap can unfortunately often not be avoided in attosecond photoelectron spectroscopy because attosecond pulses have an intrinsically high bandwidth to satisfy the Fourier-limit. If a main photoemission peak is accompanied by a small overlapping side-peak, the main photoemission delay is distorted by the photoemission delay of the side-peak. Using the restricted TDSE retrieval weights the two delays according to their feature's quadratic intensity. Consequently, small admixtures of up to 33% are mitigated, and the emission delay of the major photoemission feature is still reliably retrieved.

Generalized-Projections Retrieval

The *generalized-projections retrieval* also fits equation (4.11) to a spectrogram but requires no parametrization of the streaking field and the electron wave packet, allowing retrieving arbitrary pulse shapes and wave packet phases. The algorithm can thus retrieve the photoemission delay not only at the central energy of a photoemission feature but returns the energy-resolved photoemission delay over the attosecond pulse's bandwidth. While powerful, the unrestrictedness makes the algorithm less robust and less precise in the determination of the delay at the central energy. It is hence used to extract additional information after robust benchmark values are available from the restricted TDSE retrieval.

4.2.4 Relating Streaking and Eisenbud-Wigner-Smith Delays — Coulomb-Laser-Coupling

In the simplified case of an electron transitioning from a streaking-field-free volume to a volume in which a streaking field is present, it is comprehensible that the streaking process only starts with the entry into the streaking volume and the time of transition is encoded in the spectrogram. This simplified model is a good approximation for streaking on the surface of an efficiently screening metal [6, 19]. When considering an isolated atom, this analogy does not readily transfer, due to the lack of a natural border between the streaked and unstreaked volume. Nonetheless, the streaking spectrogram depends on the complex transition matrix element, whose phase may cause a delay in the sense of equation (3.6). However, the current delay definition (3.8) and the subtraction of the long-range Coulomb phase is based on theoretical arguments, which do not necessarily

correspond to the experimental circumstances.

In fact, streaking delays $\tau^{\text{streaking}}$ extracted from numerical simulations taking into account the full streaking experiment, i.e., a hydrogen atom and both, the XUV pump pulse and the streaking laser field, do not coincide with the predictions from equation (3.9) [60, 61]. Furthermore, the retrieved $\tau^{\text{streaking}}$ changes with the streaking laser field oscillation period T_{laser} , but is independent of its strength [62]. For fixed photoelectron kinetic energy and streaking laser field frequency, the negative offset τ^{CLC} between $\tau^{\text{streaking}}$ and the predicted τ^{EWS} does not depend on the exact system, but only the charge of the remaining ion, pointing at a measurement-induced, but correctable offset [35]. The root of this offset is an interplay of the streaking field with the long-range Coulomb potential of the photoion. Therefore, it is referred to as Coulomb-laser-coupling (CLC) or continuum-continuum delay. Because it does not depend on the individual sample, it can be predicted even for complex systems using the difference of the streaking delay from a full hydrogenic streaking simulation and the hydrogenic EWS delay with equal charge Z :

$$\tau^{\text{CLC}}(E_{\text{kin}}, T_{\text{laser}}, Z) = \tau_{\text{hydr.}}^{\text{streaking}}(E_{\text{kin}}, T_{\text{laser}}, Z) - \tau_{\text{hydr.}}^{\text{EWS}}(E_{\text{kin}}, Z) \quad (4.15)$$

With knowledge about its origin, a more illuminative approach is to reconsider the delay caused by the long-range phase term in equation (3.7). The biased assumption that the streaking measurement only samples the Coulomb field for the first quarter of the streaking field oscillation period also yields τ^{CLC} to a high level of accuracy (< 1 as error for $E_{\text{kin}} > 20$ eV and $T_{\text{laser}} > 2\mathcal{T}_{\text{xuv}}$, where \mathcal{T}_{xuv} is the XUV pulse duration) [35, 63]:

$$\tau^{\text{CLC}}(E_{\text{kin}}, T_{\text{laser}}, Z) \approx \frac{Z}{(2E_{\text{kin}})^{\frac{3}{2}}} [2 - \ln(E_{\text{kin}}T_{\text{laser}})] \quad (4.16)$$

Concluding, the attosecond streak camera can measure the short-range EWS delay, even in the presence of a long-range Coulomb potential and cases with ambiguous screening. The definition (3.8) accurately links theoretical phase predictions and experimentally determined delay results. However, an additional but universal, measurement induced offset has to be considered, either by subtracting it from the streaking delay to retrieve the EWS delay or by adding it to the theoretical EWS delay to retrieve the streaking delay. As a reference, CLC delays for photoemission from a neutral system and typical experimental parameters are plotted in figure 4.7. In further equations the superscript streaking will be omitted for brevity.

4.2.5 Disentangling Photoemission Delays from Attosecond Pulse Properties

Streaking spectroscopy reveals extensive information about the involved photoelectron wave packet and the streaking laser field. Upon closer inspection of equations (4.11) and (4.8), this manifold of information comes at a cost: The retrieved photoelectron wave packet is given by the product of the attosecond pulse and the transition matrix element which contains the information specific to the examined system. Thus, an attosecond

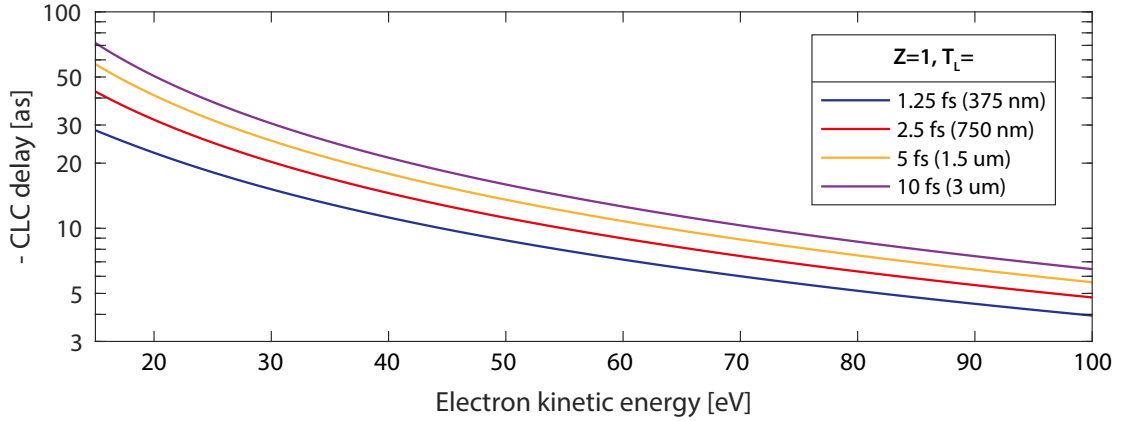


Figure 4.7: Negative Coulomb-laser-coupling (CLC) delay for photoemission from a neutral system and different streaking laser field oscillation periods. Calculated using equation (4.16).

streaking spectrogram contains no information about the source of a phase contribution:

$$\tilde{E}_{\text{xuv}}(E_{\text{kin}} + IP)\tilde{D}(E_{\text{kin}}) = \left| \tilde{E}_{\text{xuv}}(E_{\text{kin}} + IP) \right| \left| \tilde{D}(E_{\text{kin}}) \right| e^{i(\phi_{\text{xuv}}(E_{\text{kin}} + IP) + \phi_{\tilde{D}}(E_{\text{kin}}))} \quad (4.17)$$

A delay introduced by a shift of the attosecond pulse results in the same signature as a photoemission delay, and an uncompressed attosecond pulse looks like an energy-dependent photoemission delay. If the exact attosecond pulse is known, as is for example for simulated data, this is not a problem. The transition matrix element amplitude can then be recovered by dividing the retrieved wave packet amplitude by the attosecond pulse's spectral amplitude. Similarly, the transition matrix element phase, i.e., the photoemission delay and group delay dispersion, can be retrieved by subtracting the attosecond pulse's phase from the retrieved wave packet phase. For experimental sources, the attosecond pulse creation and propagation cannot be predicted to a level straightforwardly allowing this subtraction. By comparing the phase of electron wave packets created from different initial states $|1\rangle$ and $|2\rangle$ with different ionization potentials, the attosecond pulse phase can effectively be canceled, and fundamental system parameters can be explored:

$$\frac{\tilde{E}_{\text{xuv}}(E_{\text{kin}}^{(1)} + IP^{(1)})\tilde{D}^{(1)}(E_{\text{kin}}^{(1)})}{\tilde{E}_{\text{xuv}}(E_{\text{kin}}^{(2)} + IP^{(2)})\tilde{D}^{(2)}(E_{\text{kin}}^{(2)})} = \frac{\left| \tilde{D}^{(1)}(E_{\text{kin}}^{(1)}) \right|}{\left| \tilde{D}^{(2)}(E_{\text{kin}}^{(2)}) \right|} \exp\left\{i\left(\phi_{\tilde{D}^{(1)}}(E_{\text{kin}}^{(1)}) - \phi_{\tilde{D}^{(2)}}(E_{\text{kin}}^{(2)})\right)\right\} \quad (4.18)$$

$$\text{when choosing } E_{\text{kin}}^{(2)} = E_{\text{kin}}^{(1)} + IP^{(1)} - IP^{(2)}$$

Due to its simplicity and accuracy, this technique became the workhorse for experiments examining photoemission delays [6, 7]. On the downside, the technique cannot provide absolute delays, which perplexes interpretation of data and eliminates one degree of freedom in comparisons with theoretical predictions. For example, the propagation time through a screened volume in a condensed matter system mostly cancels in this method [18]. This thesis focuses on overcoming this experimental shortfall for a selection of systems of increasing complexity by referencing photoemission against a well underpinned theoretical reference. With robust knowledge of the energy-dependent transition matrix element, i.e., the photoemission delay for a specific initial state, the exact attosecond pulse can be reconstructed from the measured electron wave packet phase using equation (4.17). This, in turn, allows the absolute characterization of the photoemission timing of any system or state when compared with the reference state.

Chapter 5

Attosecond Correlation Dynamics — Setting an Absolute Reference

In 2010, Schultze et al. reported the first recording of a photoemission delay for atoms in the gas phase [7]. They found that photoelectrons originating from the 2s orbital in a neon atom precede those from the 2p orbitals by (21 ± 5) as when ejected by a ~ 100 eV photon. Consequently, the presence of this relative delay demands the existence of an absolute delay in photoemission, a process that was commonly assumed to be instantaneous. This unexpected result sparked a lively theoretical discussion suggesting different origins and contributions to this delay, for example, CLC [61] and initial state dipole laser coupling [35, 64, 65]. Multiple techniques were employed to reproduce the measured neon delay theoretically, including the R-matrix method [66, 67], a single-active-electron approximation and the relativistic and non-relativistic random phase approximation with exchange [68–70], as well as the eikonal approximation [71]. Apparently, the theoretical treatment of the neon atom is strenuous and not feasible without approximations due to the manifold interaction between its electrons. Currently, all predicted delays are smaller than the measurement's result, leaving a remaining discrepancy between experiment and theory. Very recently, an investigation with increased spectral resolution suggests a slight increase of the observed relative delay due to electrons that participated in a shake-up process [72].

To address the role of electronic correlation and benchmark whether quantum theory correctly describes photoemission, a radically simpler system than neon has to be examined. We therefore investigate the energy-dependent photoemission timing of helium, the simplest stable occurring system affected by electron interaction. Although its photoemission spectrum does not contain features from two comparable initial states, shake-up satellites exist, which can be compared to direct photoemission in a streaking experiment. With shake-up being a prototypical result of electronic correlation, i.e., the Coulomb repulsion of the involved electrons, the experiment allows scrutinizing the role of electron interaction in the photoemission process.

The presented results emerged with theoretical support from the Burgdörfer group, where Renate Pazourek performed ab-initio simulations of the experiment. The results were initially published in the article *Attosecond Correlation Dynamics* [73].

5.1 Absolute Timing of Helium Photoemission

Due to the entanglement of attosecond pulse and sample properties in attosecond streaking spectroscopy covered in section 4.2.5, a streaking experiment does not allow to measure absolute photoemission delays straightforwardly. The currently only feasible way to overcome this drawback is to use a theoretical reference to fully characterize the employed light pulses. To be robust and generally applicable a possible reference has to be reliably grasped by theory and readily available. Obvious choices are noble gases because they do not introduce additional complexity or spectral features due to molecular properties. Complete modeling of a streaking experiment on a neon or argon atom including the interaction of all electrons is not possible, however simulating the behavior of the two electrons in a helium atom is cumbersome, but feasible using supercomputers [74, 75]. These considerations define helium as the best candidate for an absolute reference.

For this purpose, we consult state-of-the-art time-dependent close-coupling ab-initio simulations of our streaking experiments [74, 76–79]. These include the full electron interaction and the XUV attosecond and streaking laser pulses. Electric fields are introduced in the dipole approximation using a velocity-gauge Hamiltonian. During the simulation, the electrons are represented by their radial distribution and their total and individual angular momenta. The system is propagated until correlation is negligible and then projected onto products of bound He^+ and continuum Coulomb states to obtain a photoelectron spectrum as from the experiment. More details on the simulation code can be found in [74, 76].

The simulations provide absolute photoemission timing because all pulse parameters, especially the arrival time of the attosecond pulse maximum at the helium atom, which we define as time-zero, are known. At the same time, because they include all involved electric fields and correctly capture electron-electron interaction, both the direct and the shake-up emission delay is predicted, allowing robust benchmarking against experimental data to verify the accuracy of the predictions. Conversely, if they prove to be accurate, we can reference the predicted direct photoemission delay to achieve an absolute calibration of our photoemission delay measurement.

5.2 Photoemission Pathways in Helium

When a photon with energy $E_{\text{xuv}} > IP_{\text{He}} = 24.6 \text{ eV}$ interacts with a ground state helium atom with ionization potential IP_{He} , it can elevate one of the helium’s electrons from the bound $1s$ orbital to a continuum state with kinetic energy $E_{\text{kin}} = E_{\text{xuv}} - IP_{\text{He}}$. This direct photoemission decreases the electron density around the helium core, resulting in an increased binding energy for the remaining electron, which is why direct emission is sometimes also addressed to as shake-down. The process is grasped by perturbation theory and the single-active-electron approximation. For photon energies exceeding the sum of the ionization potential and the energy difference between the states with principal quantum numbers $n = 2$ and $n = 1$ of singly ionized helium ($E_{\text{xuv}} > IP_{\text{He}} + \Delta E_{\text{He}^+}(n = 1 \rightarrow n = 2) = 65.5 \text{ eV}$), a second ionization pathway becomes accessible: The Coulombic

interaction between the two helium electrons can split the available photon energy between the two electrons, resulting in a continuum electron with decreased kinetic energy and an excited helium ion. This process is called shake-up. Due to its origin, the process is prototypical for the influence of correlation on the photoemission process and cannot be described in a single-electron picture. With increasing photon energy, exciting higher ionic states ($n = 3, 4 \dots$) with energies converging towards the second ionization potential ($\Delta E_{\text{He}^+}(n = 1 \rightarrow n = 3, 4 \dots) \rightarrow IP_{\text{He}^+} = 54.4 \text{ eV}$) becomes possible, resulting in an infinite series of correlation satellites with decreasing excitation cross-section [80]. A graphical representation of the energy allocation during direct and shake-up photoemission, as well as an illustrated streaking experiment and exemplary spectrogram, are found in figure 5.1. Large energy separation between direct and shake-up electrons allows separating both photoemission features, even for bandwidths allowing attosecond pulse durations and enables extracting their emission delay from the abscissa position of the energy modulation caused by the streaking laser field.

Above the double ionization potential ($IP_{\text{He}} + IP_{\text{He}^+} = 79.0 \text{ eV}$), a third photoemission feature appears. The photon energy is now sufficient to also elevate the second electron into the ionization continuum, allowing an arbitrary distribution of the excess energy between both electrons. Therefore, this feature has no discrete structure and appears as continuous background of photoelectrons with kinetic energies ($E_{\text{kin}} \in [0, E_{\text{xuv}} - 79.0 \text{ eV}]$). The relevant features and energies in the neutral helium photoelectron spectrum are summarized in table 5.1.

process	binding energy E_{bin} ($E_{\text{kin}} = E_{\text{xuv}} - E_{\text{bin}}$)
shake-down (direct)	$IP^{\text{He}} = 24.6 \text{ eV}$
shake-up into $n = 2$	$IP_{\text{He}} + \Delta E_{\text{He}^+}(n = 1 \rightarrow n = 2) = 65.4 \text{ eV}$
shake-up into $n = 3$	$IP_{\text{He}} + \Delta E_{\text{He}^+}(n = 1 \rightarrow n = 3) = 72.1 \text{ eV}$
shake-up into $n = 4$	$IP_{\text{He}} + \Delta E_{\text{He}^+}(n = 1 \rightarrow n = 4) = 74.8 \text{ eV}$
...	...
double ionization	1st e^- $IP_{\text{He}} + IP_{\text{He}^+} + E_{\text{arb}} = 79.0 \text{ eV} + E_{\text{arb}}$ 2nd e^- $[0, E_{\text{xuv}} - 79.0 \text{ eV}] \ni E_{\text{arb}}$

Table 5.1: Effective binding energies of initial states and processes occurring in the neutral helium photoelectron spectrum for $E_{\text{xuv}} > 79.0 \text{ eV}$ [80].

5.2.1 Experimental Setup

The shake-up excitation cross-section in helium is nearly a hundred times lower than the photoionization cross-section of the neon 2p orbital, a photoemission line commonly used in attosecond streaking. Therefore, although conceptually simple, a streaking experiment on helium shake-up photoemission was prevented by the low flux of attosecond XUV sources in the past. We were able to overcome previous flux limitations by employing the boosted Ti:Sa chirped-pulse-amplifier FP3, together with optimized high-harmonic generation and low absorption beam-delivery to the experiment in the AS2 beamline.

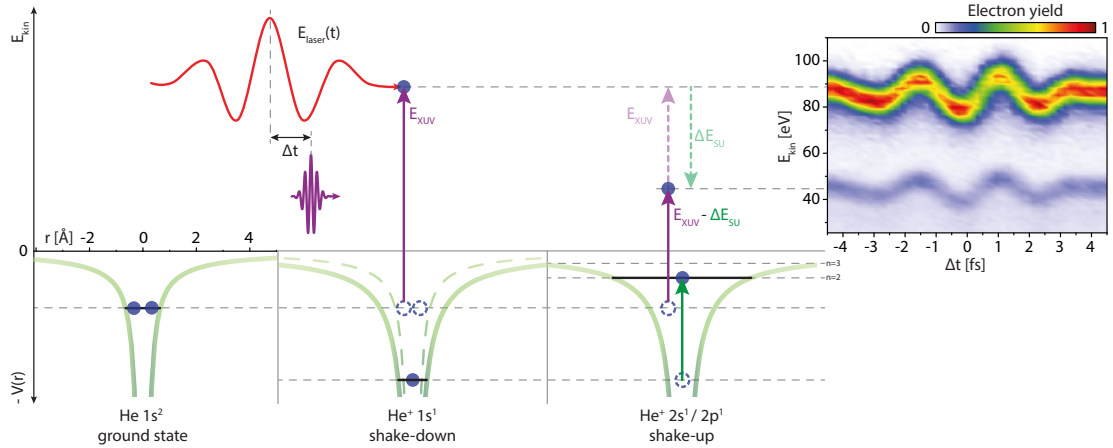


Figure 5.1: Delay investigation of correlated and uncorrelated photoemission from helium. Left column: ground state helium. The effective one-electron potential $V(r)$ is symbolized by the green lines, the two electrons in the ground state as filled blue circles. Middle column: direct photoemission. An XUV photon (purple field) elevates one electron into the ionization continuum, increasing its energy by the photon energy E_{XUV} (purple arrow). The decreased electron density around the helium ion modifies the effective potential, resulting in a stronger bond between the helium core and the remaining electron. The neutral helium states are no longer Eigenstates, however, are still suggested as a reference. Right column: shake-up photoemission into $n = 2$. The interaction of the two electrons excites the helium ion. The required energy ΔE_{SU} (green arrow) is missing from the continuum electron, shifting the photoemission line by 40.9 eV. A coincident NIR laser field (red, E_{laser}) encodes the photoelectron's time of appearance in the continuum as an energy modulation, leading to a streaking spectrogram (inset). Initial publication in [73].

The experimental setup is described in the appendices B.2 and B.5. The optimizations resulted in upwards of 10^7 XUV photons per pulse (0.3 nJ) in the relevant energy region at the measurement position. Phase matching conditions for the efficient generation of high-harmonics limit the maximum usable intensity for each generation medium, see section 4.1.3. When exceeding this maximum intensity, highly non-linear tunnel photoionization quickly creates excessive amounts of plasma, leading to a collapse in conversion efficiency. Nonetheless, higher laser pulse energies allow increasing the total flux by achieving phase matching conditions in larger generation volumes. We used CEP stable ~ 4 fs laser pulses centered around 800 nm wavelength with ~ 1 mJ energy per pulse. For neon as generating target and a collimated beam diameter of ~ 1 cm before focusing into the high-harmonic generation target, we were able to reach phase matching conditions to up to 1.2 m focusing length. Unfortunately, the slow beam size increase after the target destroyed the thin metal filters necessary to separate the generated XUV from the NIR laser pulse and correct for intrinsic high-harmonic chirp. Molybdenum

exhibited a higher damage threshold than zirconium, would however only stand after decreasing the focusing length to 1m.

XUV Pulse Synthesis and Photon Energy Calibration

We created isolated attosecond pulses using intensity gating, i.e., by filtering the high-harmonic cut-off photons generated by carrier-envelope-phase stabilized laser pulses. We were able to tune the high-harmonic cut-off region from >80 eV to >120 eV by adjusting the target pressure and laser intensity. Only a fraction of the respective cut-off region was selected by combining a metal filter and band-pass multilayer or metal mirrors to properly separate the photoemission features. Custom mirrors were manufactured by Alexander Guggenmos. The experiment was conducted at four different central photon energies from 97.2 eV to 113 eV. Figure 5.2 illustrates the respective band-pass setups. Photon pulses centered around 93.9 eV and 97.2 eV could be synthesized using a 150 nm molybdenum filter and a single Mo/Si (93 eV central photon energy design) or La/Mo (100 eV central photon energy design) multilayer mirror. The difference between the final and design photon energy was caused by the high angle-of-incidence dependence of the effective layer thickness for 45° mirrors. Due to the lack of a 108 eV mirror, this energy was selected by conscious detuning of the 100 eV mirror via changing the angle-of-incidence by $\sim 3^\circ$. This detuning causes amplitude oscillations besides the main reflection peak, which were suppressed on the low energy side using a palladium filter and on the high energy side by proper tuning of the cut-off. The resulting angle deviation was corrected using an alloyed gold/palladium mirror. Attosecond pulses centered at 113 eV photon energy were created by spectral filtering using a palladium filter and subsequent reflection off three rhodium mirrors. The lowered angle-of-incidence increases the maximum reflectivity to $>80\%$ per reflection and $>50\%$ for the whole mirror setup. The photon energy of the individual data points was determined in-situ using an XUV spectrometer after the streaking volume. Photon spectra were corrected for the spectrometer transmission and the wavelength to energy Jacobian [81]. The spectrometer was calibrated by imaging the sharp aluminum and silicon L_{III} edges for the 93.9 eV and 97.2 eV data points. The absorption of palladium prevents observation of the aluminum L_{III} edge. Therefore, the spectrometer was calibrated using the silicon L_{II} and L_{III} edges for the 108.2 eV data point, which resulted in a higher uncertainty. Since the XUV spectrum after the rhodium mirror assembly is strongly dependent on the XUV cut-off shape, thus prone to alignment changes, the average central photon energy was determined from the electron spectra for this data point. Finally calibrated photon spectra are depicted in figure 5.3. The resulting attosecond pulse FWHM durations determined via streaking (230 as at 93.9 eV, 180 as at 97.2 eV, 180 as at 108.2 eV, 130 as at 113 eV) are close to those retrieved via Fourier-transformation assuming a flat spectral phase from these spectra, suggesting close to compressed attosecond pulses.

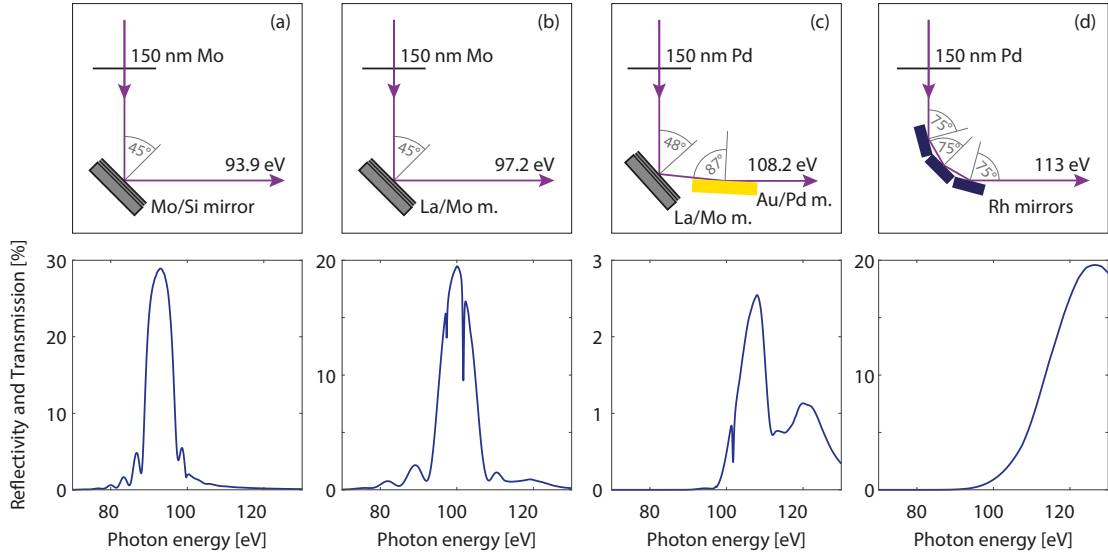


Figure 5.2: Mirror setups employed to synthesize isolated attosecond pulses at different central energies. E_{xuv} represents the central energy and $\Delta E_{\text{xuv}}^{\text{FWHM}}$ the spectral full-width-at-half-maximum (FWHM) intensity bandwidth. Panel (a): 150 nm molybdenum foil and molybdenum/silicon multilayer mirror for $E_{\text{xuv}} = 93.9$ eV, $\Delta E_{\text{xuv}}^{\text{FWHM}} = 6.8$ eV. Panel (b): 150 nm molybdenum foil and lanthanum/molybdenum multilayer mirror for $E_{\text{xuv}} = 97.2$ eV, $\Delta E_{\text{xuv}}^{\text{FWHM}} = 7.5$ eV. Panel (c): 150 nm palladium foil, lanthanum/molybdenum multilayer mirror and gold/palladium mirror for $E_{\text{xuv}} = 108.2$ eV, $\Delta E_{\text{xuv}}^{\text{FWHM}} = 8.4$ eV. Panel (d): 150 nm palladium foil and three rhodium mirrors for $E_{\text{xuv}} = 113$ eV, $\Delta E_{\text{xuv}}^{\text{FWHM}} = 13$ eV. Mirror reflectivities were provided by Alexander Guggenmos.

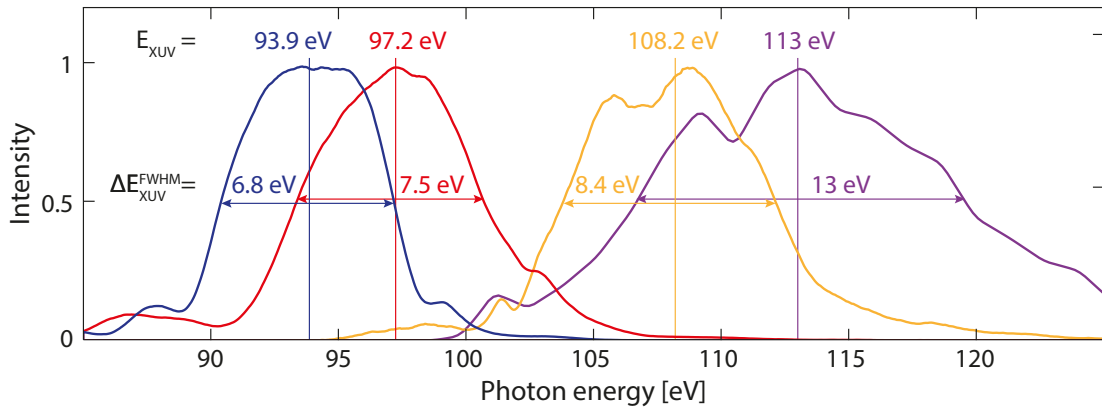


Figure 5.3: Photon spectra of the synthesized attosecond pulses used in the streaking experiment.

Electron Detection and Angle Effects

Photoelectrons were detected along the streaking laser polarization axis to maximize the delay-revealing energy modulation. To account for the high difference between the direct and shake-up photoemission cross-sections, the electron acceptance angle was increased to $\sim 15^\circ$ full angle for shake-up electrons using an electrostatic Einzel lens, equalizing the number of detected electrons in both photoemission features. The transmission of each lens setting was calibrated using the continuous inelastically scattered electron background from graphite and corrected before data analysis to avoid lens-chirp effects on the photoemission delay [82]. An exemplary unstreaked electron spectrum before and after calibration, as well as an expected spectrum folded with the XUV bandwidth at 108.2 eV photon energy, and the corresponding electrostatic lens transmission, are shown in figure 5.4. To ensure that the different angle acceptance does not affect the

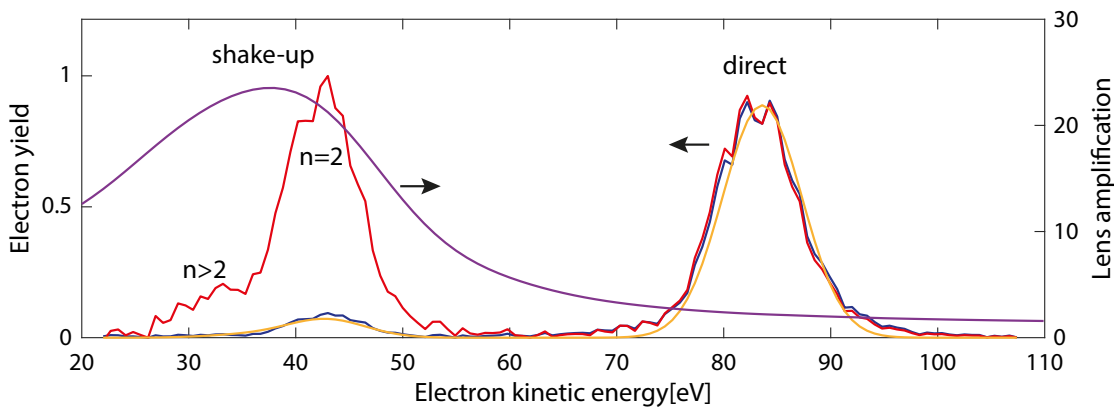


Figure 5.4: Electron spectrometer lens transmission and correction at 108.2 eV photon energy. The measured spectrum (red) is divided by the measured and smoothed lens amplification factor (purple) to mitigate effects of the electrostatic lens. The final spectrum (blue) is reproduced by synchrotron data folded with the XUV bandwidth (yellow). Initial publication in [73].

comparability of the photoemission features, ab-initio spectrograms were modeled for several angle acceptance ranges and evaluated for the photoemission delay. Results are summarized in figure 5.5 and show no dependence of both, the direct and shake-up photoemission delay, on the angle acceptance to up to 20° full angle.

5.2.2 Delay Retrieval and Experimental Results

At each central photon energy, we collected ~ 35 spectrograms over the course of multiple days to minimize the chance of hypothetical alignment induced errors. The pre-processing of all experimental spectrograms is described in the appendices A.6 and A.7. Relative photoemission delays were extracted using the restricted TDSE retrieval, described in detail in appendix A.2. The photoemission spectrum was modeled using one isolated direct feature and a composite shake-up feature as an incoherent sum of multiple photoemission

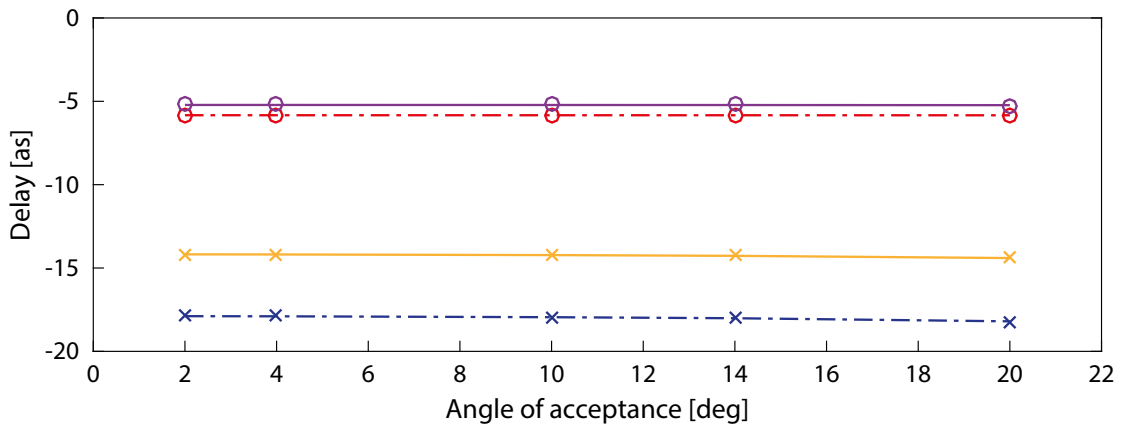


Figure 5.5: Acceptance angle independence of the photoemission delay for shake-up (crosses) and direct (circles) emission. Data for 95 eV (dashed) and 100 eV (solid) central photon energy is shown. Initial publication in [73].

lines, with their spacing and amplitude fixed to synchrotron data [80]. The treatment of multiple shake-up satellites as a composite feature was chosen because all shake-ups into states with principal quantum numbers $n > 2$ form a shoulder on the low energy side of the major $n = 2$ feature. This shoulder could not be spectrally separated due to the high XUV bandwidth necessary to achieve an attosecond pulse, see figure 5.4. All individual spectrograms were fitted by parametrizing the electron wave packet envelopes as Gaussians and assigning both features individual group delays and group delay dispersions. The features' bandwidths and the NIR streaking laser field, parametrized as a linearly chirped field with Gaussian envelope, remained coupled during the fitting process. Wave packets were parametrized in the spectral domain to avoid an unphysical coupling of the electron wave packet chirp and bandwidth as described in appendix A.4. Figure 5.6 shows an exemplary spectrogram and its retrieval.

The restricted TDSE retrieval suppresses the influence of the shoulder caused by shake-up into $n > 2$ to the composite shake-up delay. Therefore, the restricted TDSE retrieval maintains the delay of electrons that participated in shake-up into $n = 2$ as the dominating contribution to the measured shake-up composite delay. Modeling allows to artificially isolate electrons that participated specifically in shake-up into $n = 2$ and hence to examine this effect. Figure 5.7 shows the consequences for the measured streaking delay. For direct photoemission and an isolated shake-up into $n = 2$, the results of a simple COE retrieval and the restricted TDSE retrieval match. However, for a realistic composite feature, the delay retrieved via the COE method is heavily influenced by electrons from shake-up into $n > 2$, even though those account for only $< 15\%$ of the electrons in the feature. Contrary, the restricted TDSE method maintains the delay of the major $n = 2$ part. To ensure comparability, all data, including the ab-initio spectrograms, was thus evaluated using the restricted TDSE retrieval.

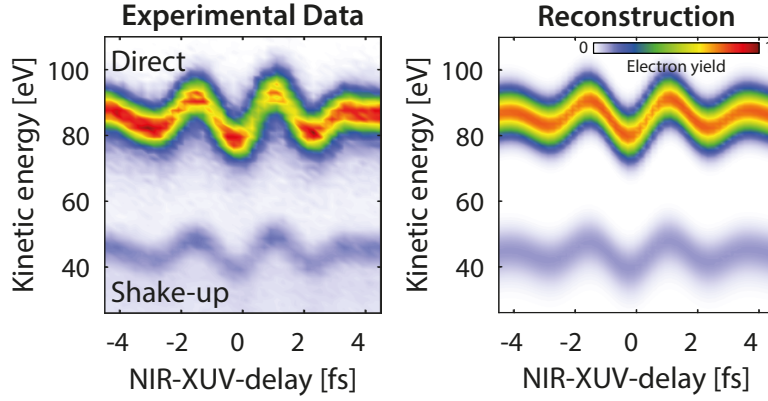


Figure 5.6: Exemplary streaking spectrogram of a helium shake-down vs. shake-up timing measurement at 108.2 eV central photon energy and its restricted time-dependent Schrödinger equation (TDSE) reconstruction. The relative delay retrieved from this individual measurement is $\Delta\tau_{\text{direct-SU}} = -7$ as.

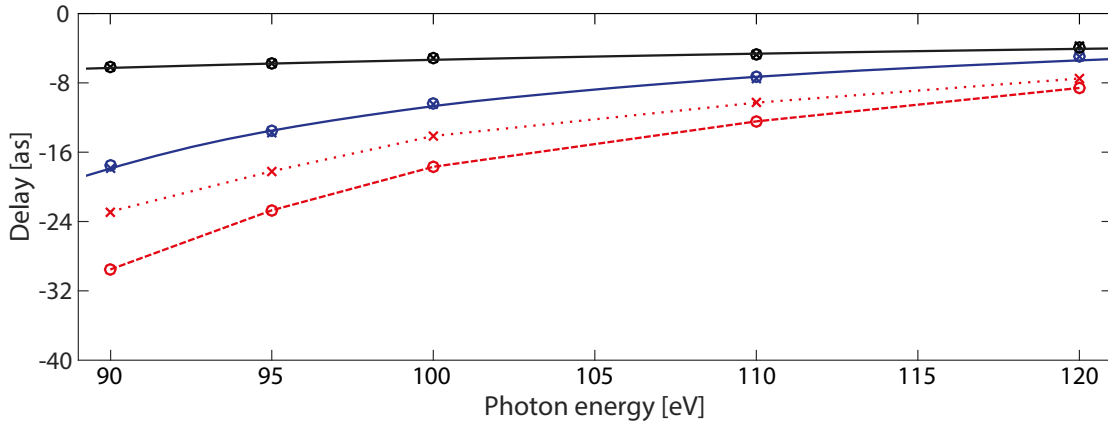


Figure 5.7: Comparison of the COE (circles) and the restricted TDSE retrieval (crosses) methods for isolated and composite photoemission features in helium (modeled). The delay results of both methods agree for direct (black) and isolated $n = 2$ (blue) shake-up photoemission with theoretical predictions (black and blue lines, the predictions are discussed in section 5.3). For a realistic composite shake-up feature (red), the COE method is heavily influenced by small $n > 2$ contributions, while the restricted TDSE retrieval (crosses) mitigates minor admixtures and retrieves values close to the isolated $n = 2$ delay. Initial publication in [73].

Statistical Evaluation

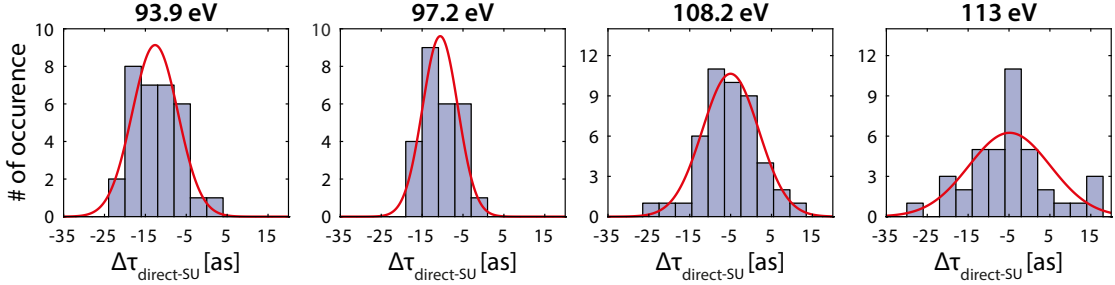


Figure 5.8: Histograms of all individual measurements of the streaking delay between direct and shake-up photoemission from helium $\Delta\tau_{\text{direct-SU}}$ (blue) and fitted normal distributions (red). Initial publication in [73].

All experimentally determined photoemission delays $\Delta\tau_{\text{direct-SU}}$ between direct and shake-up photoemission are summarized in figure 5.8. Means and uncertainties of the individual photon energy data points were calculated assuming a normal distribution of the individual measurements. Average results, standard deviations, and standard errors are summarized in table 5.2. For three data points, small standard deviations and a high number of scans allowed to achieve standard errors on the order of 1 as, providing tight margins to benchmark theory. The highest energy data point has a slightly higher standard deviation, probably due to increased photon energy and bandwidth fluctuations permitted by the less restrictive spectral filtering of the XUV radiation. Due to the implementation of a parameter-less differential background subtraction (appendix A.7) and automatic starting guess determination from simplified fitting schemes (appendix A.2), the influence of the evaluator on the results is limited to cropping experimental spectrograms. We find a negligible influence of cropping parameters on the average delay values for reasonable choices. Shake-up emission precedes direct electron emission for all examined photon energies. The negative delay magnitude $\Delta\tau_{\text{direct-SU}}$ between shake-up and direct emission decreases with increasing photon energy. This trend corroborates the predictions for hydrogenic systems (see figures 3.4 and 4.7) of an increasing delay magnitude with decreasing photoelectron energy.

photon energy [eV]	# of scans	$\Delta\tau_{\text{direct-SU}}$ [as]	std. deviation [as]	std. error [as]
93.9	32	-12.6	5.6	0.99
97.2	26	-10.6	4.3	0.85
108.2	46	-5.0	6.9	1.01
113.0	39	-4.9	10.0	1.60

Table 5.2: Experimental averages and uncertainties for $\Delta\tau_{\text{direct-SU}}$.

Estimation and Correction of Attosecond Pulse Chirp Influence

Artificial relative delay contributions due to the coupling of an energy-dependent photoemission cross-section and attosecond pulse chirp, as described in appendix A.5, are limited because the shake-up and direct photoemission cross-sections exhibit parallel energy dependencies in the relevant energy region [80]. Moreover, XUV pulses with low group delay dispersion were synthesized for the experiment to further mitigate possible effects. Residual effects were estimated and accounted for using the energy-dependent photoionization cross-sections from synchrotron measurements [80] and the attosecond XUV pulse’s group delay dispersion retrieved from the direct emission’s electron group delay dispersion. Direct helium photoemission introduces close to negligible intrinsic delay dispersion, shown for example in figure 5.9, and therefore allows direct extraction of the group delay dispersion. The changes due to this correction are ≤ 1 as for each central photon energy and are summarized in table 5.3.

photon energy [eV]	$\Delta\tau_{\text{direct-SU}}$ uncorrected [as]	average chirp correction [as]	$\Delta\tau_{\text{direct-SU}}$ corrected [as]
93.9	-13.0	0.4	-12.6
97.2	-11.0	0.4	-10.6
108.2	-5.1	0.1	-5.0
113.0	-5.9	1.0	-4.9

Table 5.3: Estimation and correction of chirp influence on the measured average photoemission delays.

Comparison of Theoretical Predictions and Experimental Results

Table 5.4 compares experimental results and their theoretical counterpart. Modeling

photon energy [eV]	$\Delta\tau_{\text{direct-SU}}$ [as] experiment	$\Delta\tau_{\text{direct-SU}}$ [as] simulation	standard error [as] experiment	deviation [as]
93.9	-12.6	-12.7	1.0	0.1
97.2	-10.6	-11.0	0.9	0.4
108.2	-5.0	-5.9	1.0	0.9
113.0	-4.9	-5.8	1.6	0.9

Table 5.4: Comparison of experimental averages and theoretical predictions for the $\Delta\tau_{\text{direct-SU}}$ delay.

reproduces the experiments within error margins. The near-perfect agreement for all data points sets the upper limit for systematic errors in both the streaking experiments and the quantum modeling to below 1 as. The reproduction of this complex relative delay demonstrates the accuracy of state-of-the-art ab-initio modeling and verifies its predictions. These can thus serve as an absolute reference in photoemission timing. Furthermore, it limits the contribution of effects not grasped by the non-relativistic

Schrödinger equation to below 1 as. We can therefore switch to an absolute scale by using direct photoemission as an absolute reference and adding our relative measurements to retrieve the absolute delay of the shake-up photoemission feature. The direct feature is the preferred reference due to its cross-section, spectral isolation and the simple predictability of its delay. This step is illustrated in figure 5.9.

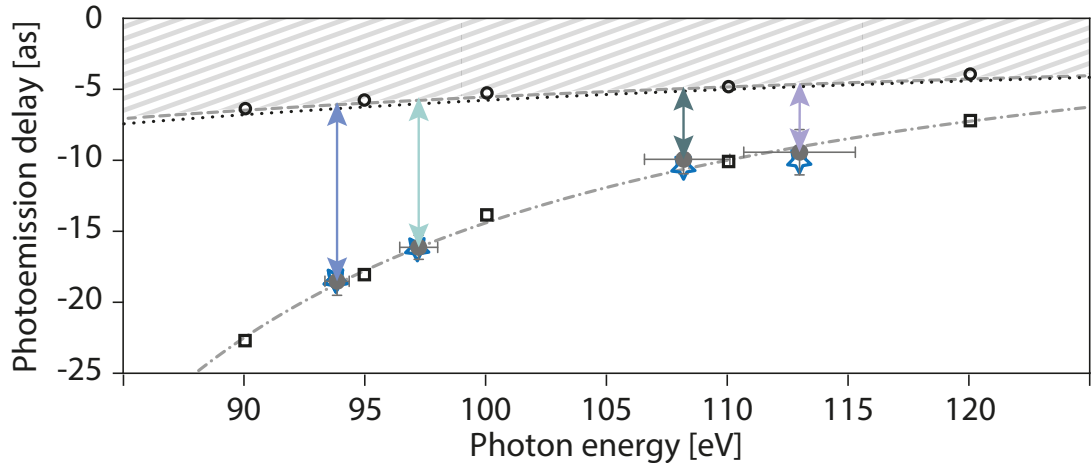


Figure 5.9: Absolute photoemission delays for helium. The direct photoemission reference obtained from ab-initio modeling (black circles), exterior complex scaling calculations (grey dashed line) and a single-active-electron simulation (black dotted line) agree. Absolute shake-up photoemission delays (full grey dots) are obtainable by adding the measured direct-to-shake-up delays (arrows) to the reference. Experimental results agree with ab-initio modeling results for experimental pulse parameters (blue stars) and a fit (grey dashed-dotted line) of equation (4.16) to the ab-initio results for standard pulse parameters (black squares). Initial publication in [73].

5.2.3 High Order Photoemission Phase Terms

To additionally check the accordance of modeling and experiment, we consider a generalized-projections type retrieval of our data, as described in appendix A.3. This retrieval type can extract the energy-dependent group delay without assumptions about its shape. We run the retrieval algorithm for all individual scans, with two central momenta set to the individual wave packet central energies to minimize errors due to the central momentum approximation. The two energy areas are coupled by mixing their retrieved NIR electric fields between steps. We then shift the central electron energy to the central photon energy and subtract the electron wave packet group delay retrieved for the direct photoemission feature from the shake-up feature to eliminate attosecond pulse parameters. The unchanged procedure is applied to measured and calculated spectrograms. We find that the relative delay at the central position is predicted more

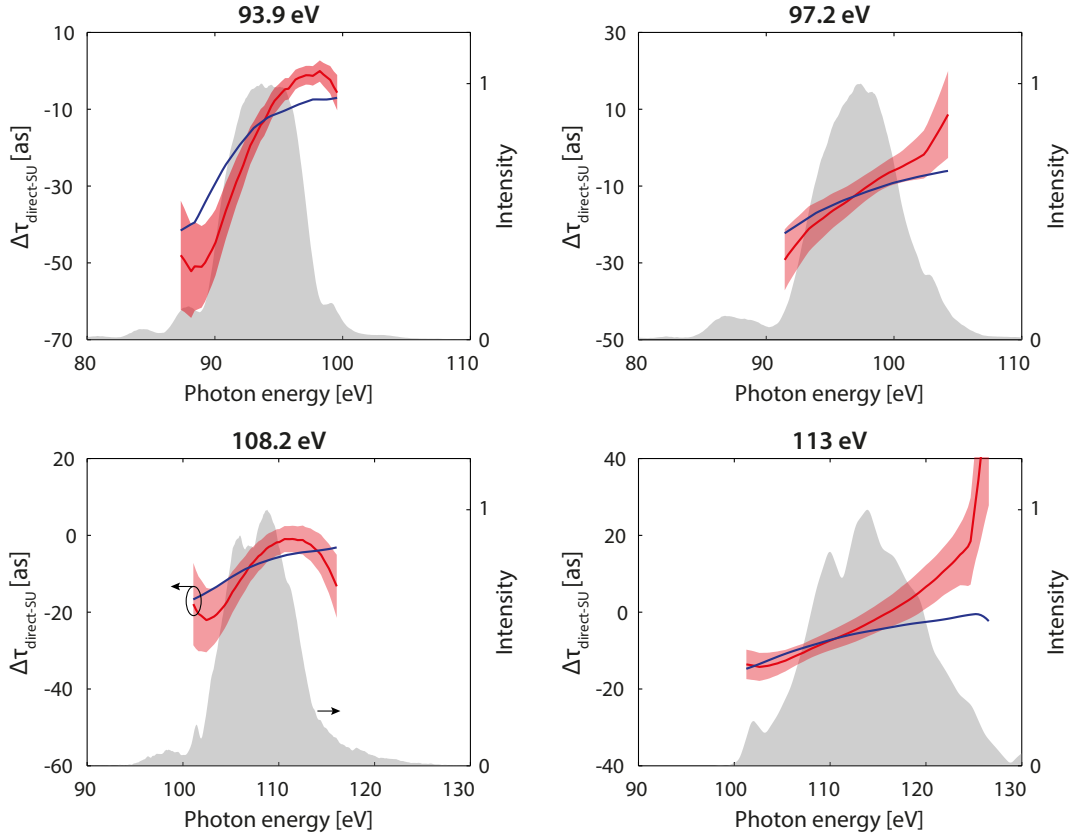


Figure 5.10: Generalized-projections retrieval of the energy-dependent relative photoemission delay in helium. Photon spectra in the measurement (grey), experimental results (red lines) and standard errors (red shaded areas), as well as theory results (blue lines) are shown. Initial publication in [73].

accurately by the restricted TDSE method. However, higher order terms are reproducibly extracted by the generalized-projections algorithm. The higher order phase terms in the energy-resolved group delay match between the experiment and theoretical modeling, further promoting the accuracy of the attosecond streak camera and ab-initio simulations.

5.2.4 Isolation of the $n=2$ Shake-Up Delay

Up to this point, the composite delay of the entire shake-up feature was treated. An in-depth analysis of delay contributions benefits from a clear state-assignment, i.e., treating only shake-up into a single state. To isolate the $n = 2$ shake-up delay, we compare the results of the restricted TDSE method and the generalized-projections method in figure 5.11. The generalized-projections retrieval can extract the photoemission delay over the whole bandwidth of the attosecond pulse, while the restricted TDSE retrieval only extracts the emission delay at the attosecond pulse's central energy. The energy-resolved

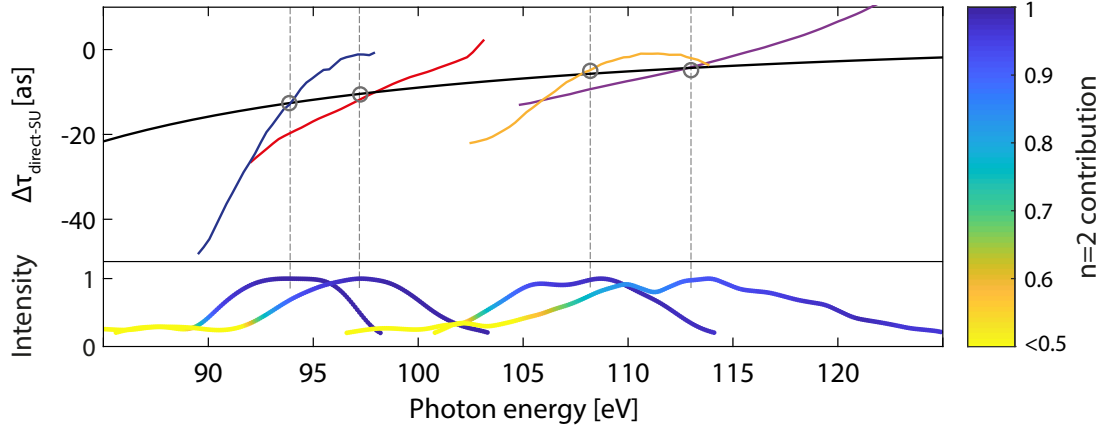


Figure 5.11: Relative electron wave packet group delay extracted using the generalized-projections method (blue, red, yellow, purple lines) and the restricted TDSE method (grey circles). A fit through the restricted TDSE results is shown as a guide to the eye (black line). Error bars are omitted for clarity but can be found in figures 5.9 and 5.10. The calculated $n = 2$ contribution to the composite shake-up wave packet intensity is illustrated as color graded lines.

delay should thus fill the energy regions between the four employed central attosecond pulse energies, an in-depth example of this is shown and discussed in figure A.4. However, for the direct-to-shake-up composite delay, we find a significant discrepancy between the expected result and the group delay retrieved using generalized-projections. Both, the group delay dispersion and third-order dispersion in figure 5.11 are increased compared to the curve suggested by the restricted TDSE retrieval. Especially conspicuous are the jumps of the group delay between the different energy areas. The source of this behavior must be in the spectral overlap of the $n > 2$ shake-ups with the $n = 2$ shake-up because the direct photoemission peak is spectrally isolated. They are positioned at the low energy side of the shake-up feature, where the biggest discrepancy is found. The restricted TDSE retrieval is rather immune to these additions and can grasp the linear group delay dispersion without distortion of the measured delay. Third-order dispersion, i.e., the second derivative of the group delay in figure 5.11, is not accounted for and its existence can influence the delay, because of its symmetry around the central energy. To estimate the influence for $n > 2$ shake-up contributions, we therefore fit the generalized-projections group delay curve measured for each photon energy with a linear and quadratic model and assume a linear photon energy dependence of the overall correction to estimate the error. To avoid compensating third-order dispersion intrinsic to the isolated $n = 2$ shake-up, we also estimate this difference for the curve obtained from the restricted TDSE retrieval. This calculation yields a 2.7 as to 0.5 as correction to isolate the $n = 2$ shake-up delay from the composite shake-up delay but also increases the uncertainty. The isolated $n = 2$ shake-up photoemission delay is shown in table 5.5. It can be compared to the ab-initio prediction, from which we can either isolate the

$n = 2$ shake-up delay using the same technique or, more convenient, by eliminating higher shake-ups artificially by projecting only onto final states where the remaining bound electron is found in the $n = 2$ state. Both methods match with our experimental values within the standard error.

photon energy [eV]	$\Delta\tau_{\text{direct-SU}}$ [as]	$\Delta\tau_{\text{direct-}n=2}$ [as]	standard error [as]	$\tau_{n=2}$ [as]
93.9	-13.0	-9.9	2.2	-15.8
97.2	-11.0	-8.2	1.8	-13.8
108.2	-5.1	-4.0	1.8	-8.8
113.0	-5.9	-4.4	2.6	-8.9

Table 5.5: Isolation of the average relative and absolute $n = 2$ shake-up photoemission delay from the average composite delay.

5.3 Contributions to the Photoemission Delay

On an absolute scale, many of the contributions to the photoemission delay are unentangled, allowing to separate the streaking delay into individual parts. These can then be used to estimate the influence of such delay constituents on other species or measurements.

5.3.1 Direct Photoemission

Even though the direct photoemission delay is known from ab-initio modeling, the data is not significantly easier to interpret than an experiment. Being ab-initio, interaction mechanisms cannot straightforwardly be changed or switched. Therefore, simplified models which exclude defined parts of the experiment can contribute to the understanding of data retrieved from ab-initio modeling. Direct photoemission can be grasped by many levels of theory because it is mainly a one-electron process. Figure 5.12 compares predictions for the direct helium photoemission delay achieved using different theoretical methods. A single-active-electron calculation excluding electronic correlation but including both electric fields allows to isolate possible correlation effects and a calculation of the two-electron transition matrix element without streaking field based on exterior complex scaling [83], provided by the Burgdörfer group, allows examining the influence of the streaking laser field. Additionally, we performed a calculation using the ePolyscat [84, 85] scattering code provided by Robert Lucchese and the ePSproc scripts by Paul Hockett [86] and extracted the photoemission delay from the asymptotic electron wave packet phase. Only the single-active-electron calculation reproduces the ab-initio delay at first glance. However, acknowledging that the other simulations all disregard the streaking laser field, the universal CLC delay has to be added manually according to equation (4.15) before comparing the EWS delay and the streaking delay from the ab-initio calculation. When including the CLC delay for 800 nm streaking wavelength, all predictions coincide within 0.5 as. We can hence confirm that the streaking delay is given by the sum of both, the

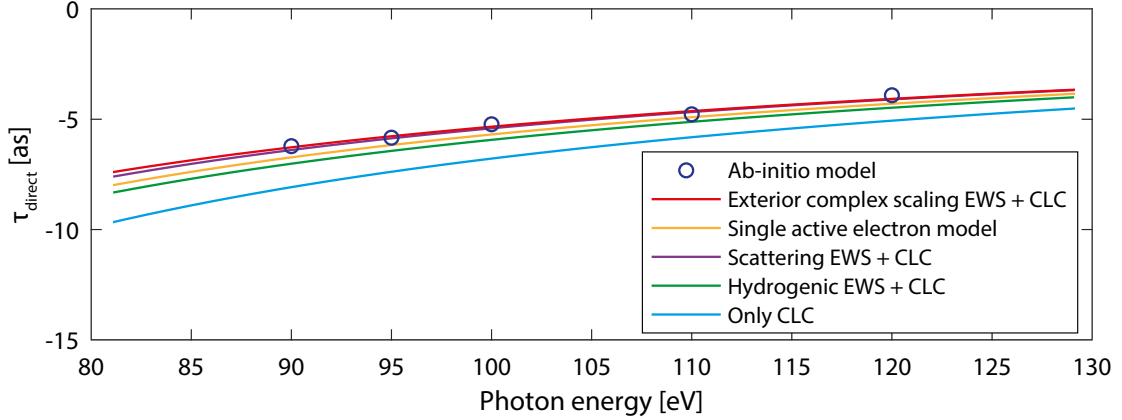


Figure 5.12: Predictions for the absolute direct helium photoemission streaking delay τ_{direct} calculated using different theoretical methods.

EWS and the CLC delay.

$$\tau_{\text{direct}} = \tau_{\text{direct}}^{\text{EWS}} + \tau_{\text{direct}}^{\text{CLC}} \quad (5.1)$$

In this case, the streaking delay is dominated by the CLC delay. Astonishingly, even the hydrogenic prediction of the photoemission delay using equation (3.9) does not deviate by more than 0.8 as, highlighting the simplicity of this emission process. The agreement across all modeling methods corroborates the absolute result of the ab-initio calculation and the use of direct helium photoemission as an absolute reference. In an experiment focussing on attosecond pulse parameters, the small energy dependence of ≤ 0.15 as/eV over the whole energy range allows to directly extract the attosecond pulse's group delay dispersion and duration to high precision even without photoemission delay correction.

5.3.2 Shake-Up Photoemission into n=2

More challenging is the timing of the shake-up process, due to its origin in electron interaction. Due to the same reason, only the ab-initio and two-electron exterior complex scaling methods can grasp this process. While the ab-initio calculation reproduces the experimentally measured value, surprisingly, even after adding the CLC contribution to the EWS delay from the streaking field free method, a significant discrepancy remains, see figure 5.13. The shake-up streaking timing therefore has to include an additional delay term τ^{e-e} :

$$\tau_{n=2} = \tau_{n=2}^{\text{EWS}} + \tau_{n=2}^{\text{CLC}} + \tau_{n=2}^{e-e} \quad (5.2)$$

Because τ^{e-e} only appears in the correlated emission path, it will be called correlation delay further on. Its origin must also be related to the presence of the streaking field since it is not captured by the two-electron transition matrix element. However, it should be noted that the EWS delay as well contains multi-electron-interactions since these

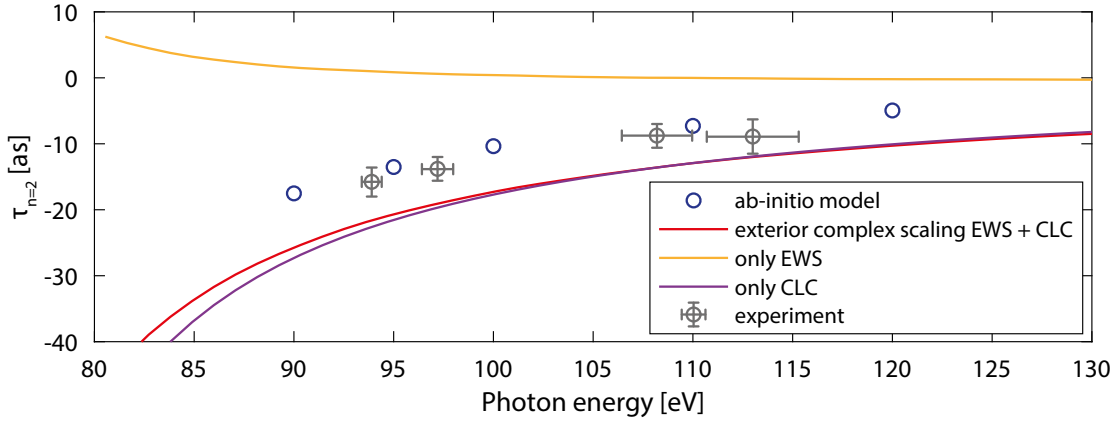


Figure 5.13: Experimental data, ab-initio predictions and predicted contributions for the photoemission delay of electrons participating in shake-up into $n = 2$.

define the effective potential from which the photoelectron has to escape. Subtracting the EWS and CLC delays from the isolated $n = 2$ streaking delay yields the separated correlation delay, which is presented in table 5.6.

photon energy [eV]	$\tau_{n=2}$ [as] experiment	$\tau_{n=2}^{\text{EWS}} + \tau_{n=2}^{\text{CLC}}$ [as]	$\tau_{n=2}^{e-e}$ [as] experiment	$\tau_{n=2}^{e-e}$ [as] ab-initio
93.9	-15.8	-21.6	5.8	7.3
97.2	-13.8	-18.8	5.2	6.9
108.2	-8.8	-13.6	4.8	5.8
113.0	-8.9	-13.3	3.1	5.4

Table 5.6: Average correlation delay for photoelectrons participating in shake-up into $n = 2$.

5.4 Correlation Delay

According to selection rules, the angular momentum should not be changed during the shake-up process, because it is a monopole transition [87, p. 479]. Nonetheless, experiments find a significant population in the 2p state after shake-up [88]. With populating both, the 2s and 2p state, the shake-up excitation creates a state with a non-zero electric dipole moment $d_{n=2}^{\text{eff}}$ due to the symmetry and interference of the states. This process is especially pronounced in singly ionized helium because the lack of intra-atom electron-electron interaction leads to all states in a principal quantum number being close to degenerate, e.g., all $n = 2$ states are spaced by less than 1 meV [89]. The beating between two coherently populated states is defined by their energy spacing, i.e., this dipole oscillates only on a picosecond timescale.

When the photoelectron leaves its parent ion, the Coulomb repulsion pushes the

electron remaining with the ion to the opposite side of the helium core, which creates a dipole between the positively charged helium core and the remaining electron. We detect photoelectrons only in a limited angle region around the XUV polarization axis. Therefore, all detected electrons left an ion with defined electric dipole moment and orientation. The calculated probability densities of the remaining electron after selective excitation into $n = 2$ and $n = 3$ are plotted in figure 5.14. Integration around the direction of photoelectron escape demonstrates the increased electron density behind the ion's core. Ab-initio modeling reveals that the resulting dipole moment rises with the principal shake-up quantum number.

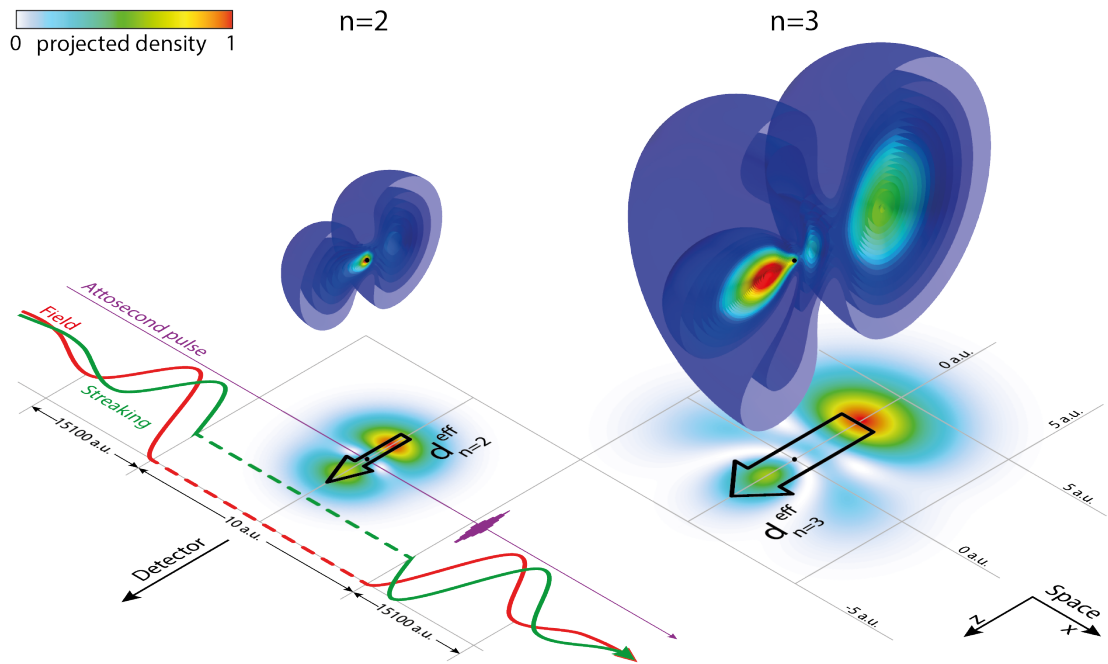


Figure 5.14: Electronic charge density isosurfaces [90] around the helium core (black dots) after shake-up photoemission into $n = 2$ and $n = 3$. False color plots represent the density integral around the direction of photoelectron escape (detector direction, full black arrow), the resulting dipole moments d^{eff} are indicated as hollow black arrows. The streaking shift of the photoelectron is determined by the streaking field vector potential (green line) at the XUV pulse center (purple line). Creation of the dipole moments causes an additional photoelectron energy modulation, which is in phase with the streaking field (red line). Due to the time confinement of the photoelectron birth, the electric field and vector potential are approximately constant during the process. Initial publication in [73].

Changing the dipole moment during an attosecond streaking experiment can influence the photoemission delay as has been proposed by Baggesen et al. [64, 65, 74]. When

the XUV transition modifies the dipole moment in the presence of the streaking laser electric field, additional energy has to be accounted for due to the linear Stark effect at the instant of photoionization. This energy variation evolves in phase with the streaking field because it is linear in the applied electric field strength and hence phase-shifted compared to the streaking modulation, which follows the streaking field vector potential. As a result, the additional shift translates to a delay which depends on the orientation of the dipole change and the laser field. The phase relation of the Stark and streaking modulation and the orientation of the dipole and detector are illustrated in figure 5.14.

In light of the fact that only alternating fields are involved in the transition, a quadratic Stark shift is intuitively expected. However, because the relevant time of emission is defined by the duration of the XUV pulse, which is short compared to the streaking laser field period, the alternating nature of the streaking field is obscured.

To retrieve the induced emission delay, the final electron energy calculated from equation (4.4) has to be extended by the Stark shift of the initial state with dipole moment \vec{d}_i and the negative Stark shift of the final state with dipole moment \vec{d}_f . Choosing $\vec{E}_{\text{laser}}(t) = \vec{E}_{\text{laser}} \cos(\omega_{\text{laser}}t)$, thus $\vec{A}_{\text{laser}}(t) = -\frac{\vec{E}_{\text{laser}}}{\omega_{\text{laser}}} \sin(\omega_{\text{laser}}t)$, allows to use a trigonometric relation to calculate the phase shift and delay of the streaking modulation $\Delta E_f(t)$ [63]:

$$\begin{aligned} \Delta E_f(t) &= \frac{1}{2} \vec{A}_{\text{laser}}^2(t) - \vec{p}_i \cdot \vec{A}_{\text{laser}}(t) + (\vec{d}_f - \vec{d}_i) \cdot \vec{E}_{\text{laser}}(t) \\ &= \frac{1}{2} \vec{A}_{\text{laser}}^2(t) + \frac{\vec{p}_i \cdot \vec{E}_{\text{laser}}}{\omega_{\text{laser}}} \sin(\omega_{\text{laser}}t) + (\vec{d}_f - \vec{d}_i) \cdot \vec{E}_{\text{laser}} \cos(\omega_{\text{laser}}t) \\ \vec{d}_f \parallel \vec{d}_i \parallel \vec{E}_{\text{laser}} &\frac{1}{2} A_{\text{laser}}^2(t) + \text{const.} \times \sin(\omega_{\text{laser}}(t + \tau^{e-e})) \quad \text{with} \end{aligned} \quad (5.3)$$

$$\tau^{e-e} = \frac{1}{\omega_{\text{laser}}} \tan^{-1} \left(\frac{(d_f - d_i)\omega_{\text{laser}}}{p_i} \right) \quad (5.4)$$

The dipole delay has no streaking field intensity dependence because the Stark shift and the streaking modulation are coincidentally linear in the electric field amplitude. If the orientation of the dipole moment change is random, the additional energy variation cancels when averaging over an ensemble, e.g., in the case of unoriented molecules. In case of helium shake-up emission, the final dipole is always pointing along the direction of electron detection due to the electron repulsion in the exit channel.

While not predicting the correlation delay, the time-independent exterior complex scaling calculation predicts the dipole moment change due to the XUV transition, which agrees with the dipole moments predicted by the ab-initio model. The resulting correlation delay can thus be calculated using equation (5.4) and accounts for the difference of the measured streaking delay and the time-independent exterior-complex-scaling calculation in figure 5.13. This dependence is illustrated in figure 5.15, which links correlation delay, photon energy and dipole moment.

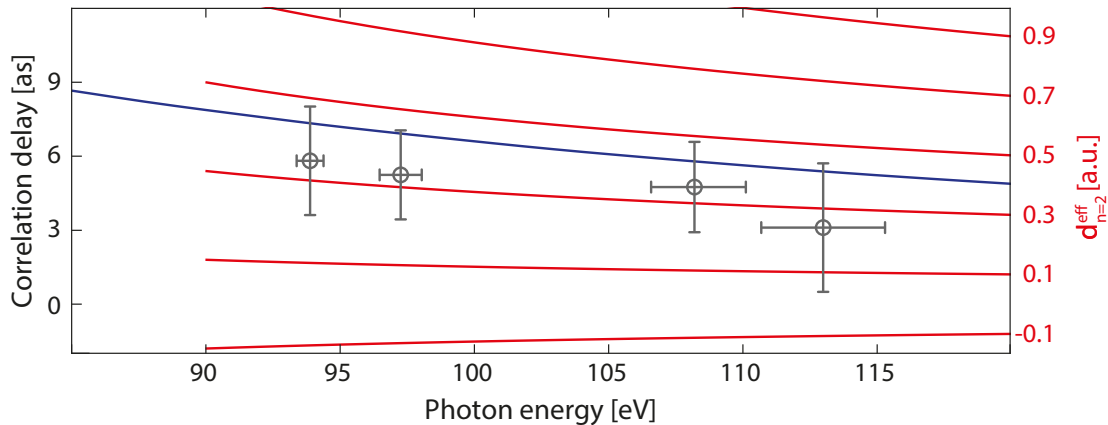


Figure 5.15: Correlation delay and dipole moment energy dependence for streaking using 800 nm wavelength light. Red lines illustrate the nonlinear conversion between induced dipole moment and correlation delay. The correlation delay calculated using the dipole moments from the two-electron transition matrix elements (blue line) agrees with the experimental correlation delay (grey circles). Initial publication in [73].

5.5 Shake-Up into $n > 2$ States

Examining excitation into higher shake-up states is a viable way to further solidify the presented composition of delays and correlated dipole-delay mechanism. Due to the decreasing state spacing and excitation cross-section with increasing shake-up quantum number, an extraction of meaningful delays is not possible from our experimental data without additional information such as detection of the fluorescence photon from the shake-up excitation's decay [74]. The ab-initio method relies on projecting onto asymptotic product states of the photoelectron and the remaining ion to isolate shake-up into the different principal quantum numbers, which is rather similar to detecting fluorescence photons. However, even the extraction from ab-initio data poses unexpected problems: Because the streaking laser photon energy is comparable to all energy spacings $\Delta E_{\text{He}^+}(n > 3 \rightarrow n > 4)$, the streaking field can efficiently drive transitions. This fact is evident from the asymptotic population of the states for different moments of XUV excitation during the streaking laser field, which is plotted in figure 5.16. For field strengths above those used for streaking, even the population in $n = 2$ can be modified. Such a population change in the ion after the XUV excitation destroys the assignment of a photoelectron with its initially excited state, which renders results of both theory and experiment ambiguous. We therefore resorted to a computationally more expensive, but stable, approach. By modeling photoemission from helium by a compressed 1.3 eV bandwidth XUV pulse (corresponding to 1400 as FWHM intensity duration), $n = 3$ is sufficiently spectrally separated from both $n = 2$ and $n = 4$. To still achieve streaking for a long ionizing pulse we also changed the carrier wavelength of the streaking laser pulse

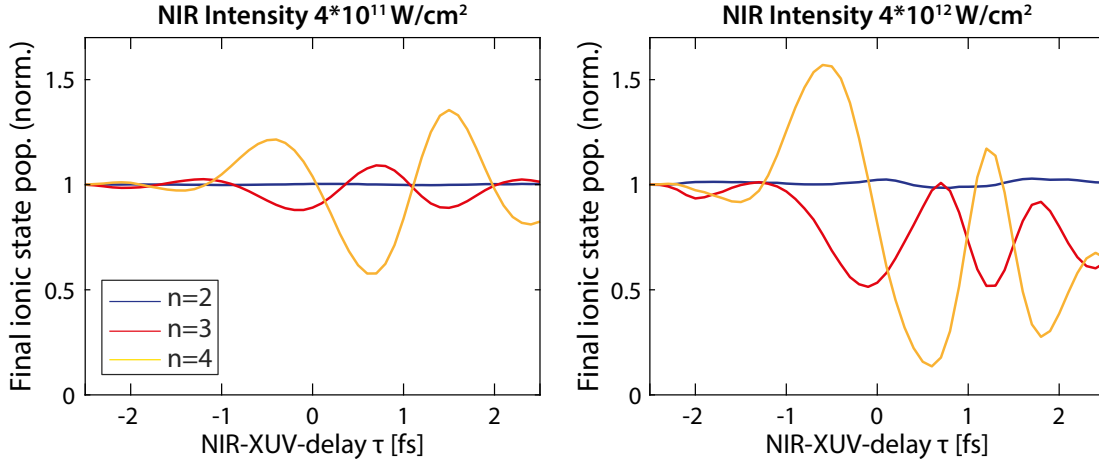


Figure 5.16: NIR-XUV delay dependent shake-up state population after all electric fields have vanished. At moderate intensity (left panel), the $n = 2$ population is stable but the streaking field transfers population between higher shake-up states. For higher intensity (right panel), the streaking field also influences the $n = 2$ population. Initial publication in [73].

to 1500 nm (5 fs period). These changes allowed extracting the isolated $n = 2$ and $n = 3$ streaking delay from the full calculated spectrogram using the restricted TDSE retrieval. Furthermore, the coupling of the states due to the streaking laser field is suppressed due to the lower streaking photon energy. For 100 eV XUV excitation photon energy and shake-up into $n = 3$, predictions are an EWS delay of -1 as, a CLC delay of -29 as and a correlation delay of 38 as. The increased CLC advance compared to the experiment is caused by the longer streaking field wavelength and lower photoelectron kinetic energy, while the highly increased correlation delay is mainly caused by the increased electric dipole moment of the excited $n = 3$ manifold. The absolute value extracted from the ab-initio calculation is 10 as, in close agreement with the sum of the above, the $n = 2$ delay also matches its prediction.

5.6 Complete Measurement of a Quantum State

The helium ground state cannot possess a permanent electric dipole moment. Therefore, the full dipole change can be attributed to the final state. Consequently, equation (5.4) directly links the observed correlation delay with the dipole of the final ionic state, allowing to extract the created dipole moment from the experimental photoemission delay.

Coming back to the origin of this electric dipole moment allows to gain further insight into the synthesized final state: the electric dipole moment $d_{n=2}^{\text{eff}}$ of the $n = 2$ state after excitation is given by the relative amplitude c_{2s}/c_{2p} and phase $\Delta\phi_{2s-2p}$ between the two populated $n = 2$ sub-states, as well as the maximum dipole moment $d_{n=2}^+ = 3/2$ at. u. of

one electron in a $n = 2$ Stark state [74].

$$d_{n=2}^{\text{eff}} = 2d_{n=2}^+ \cos(\Delta\phi_{2s-2p}) \frac{|c_{2s}/c_{2p}|}{1 + |c_{2s}/c_{2p}|^2} \quad (5.5)$$

The 2s/2p amplitude ratio has been measured using the lifetime difference between the metastable 2s and the fast decaying 2p state [88]. All quantities except $\Delta\phi_{2s-2p}$ in equation (5.5) are known, allowing to retrieve the relative 2s-2p quantum phase from the correlation delay. Experimental results for the 2s-2p phase are displayed in figure 5.17, as well as the partial excitation cross-sections c_{2s}^2 and c_{2p}^2 from [88]. The phase is only weakly depending on the amplitude ratio, mitigating propagating errors in the amplitude ratio. We find no dependence of the phase on the XUV photon energy which initiates photoemission in the examined energy region. Ab-initio calculations allow varying the streaking field and show that the phase and thus the dipole is also independent of the field strength in the $1 \times 10^9 \text{ W/cm}^2$ to $1 \times 10^{12} \text{ W/cm}^2$ intensity range. In case of the

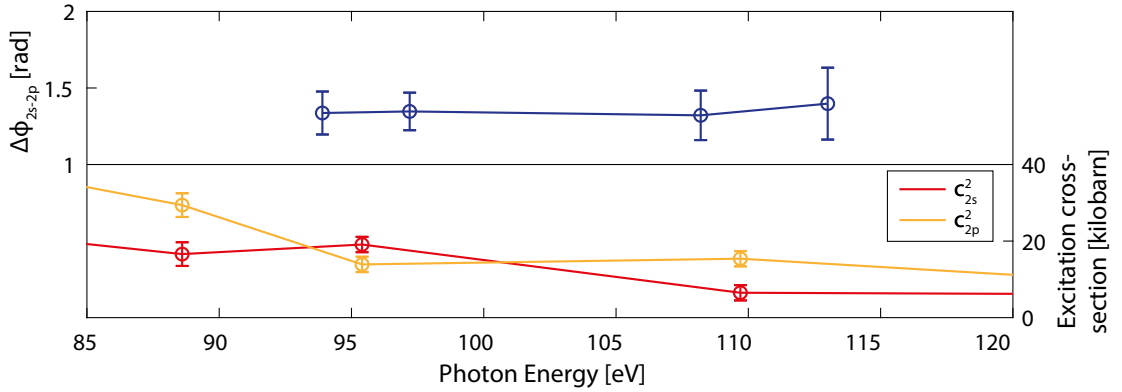


Figure 5.17: The measured 2s-2p quantum phase $\Delta\phi_{2s-2p}$ calculated from the correlation delay (blue) and the partial excitation cross-sections c^2 for the 2s (red) and 2p (yellow) state from [88].

isolated excitation of $n = 2$, attosecond streaking spectroscopy can thus use the entangled electron emission process to determine not only the photoelectron wave packet but also the complete quantum state of the photoion after photoemission, including the starting phase and hence the time evolution of the dipole oscillation.

Chapter 6

Absolute Photoemission Delays from Small Molecules

With an established absolute reference, we can examine the dynamics during unresolved photoemission processes. A discussed topic in atomic physics is the origin of giant dipole resonances in the above-threshold photoabsorption spectrum of atomic orbitals with $n > l + 1$ [91]. Prominent atomic orbitals that show this absorption resonance are the argon 3p and the 4d shells in atoms with charge numbers near xenon. The name stems from nuclear physics, where excitable collective oscillations of the nuclear constituents lead to a broad increase in the absorption of MeV photons [92, 93]. Due to similar properties, this notion was adopted to describe broad resonances in the absorption spectrum of atoms, which were analogously explained by collective oscillations in the electronic shell [94, 95]. This explanation is however controversial because higher order excitations have not yet been observed [93]. A competing description from a scattering viewpoint is that the effective radial potential for the photoelectron has well-like structure due to competition of the attractive and repulsive Coulomb forces and the repulsive angular momentum barrier. If the well is below critical strength, no bound states exist. Low energy scattering states cannot permeate into the well. Above the threshold, scattering states start to penetrate and then show increased probability density inside the well. Because the initial states are located close to the atom, this raises the transition probability to these states, which is seen as resonance in the photoionization spectrum. This scenario is illustrated in figure 6.1. The observed broadness of atomic giant resonances is explained by excessive lifetime broadening due to the short sojourn of such high-lying scattering states in the well. Resonances with similar origin occur in the photoemission spectra of molecules, in the form of shape resonances [10]. However, none of these two explanations straightforwardly predicts the giant resonance cross-sections quantitatively.

To check whether a delay accompanies photoemission through a giant dipole resonance, we present an absolute attosecond streak camera measurement on photoemission from iodine core orbitals in small molecules, which show a broad giant resonance at ~ 94 eV photon energy in the $4d \rightarrow \epsilon f$ channel [97]. For this purpose, we applied the tested helium reference. We chose an absolute measurement not only for convenience but also because iodine 5s and 5p electrons copy the behavior of the 4d cross-section in the vicinity of the giant dipole resonance. Hence, unambiguous referencing is not possible against electrons originating from molecular valence orbitals.

We chose to examine iodine over xenon because it can be reused as a gauged reference

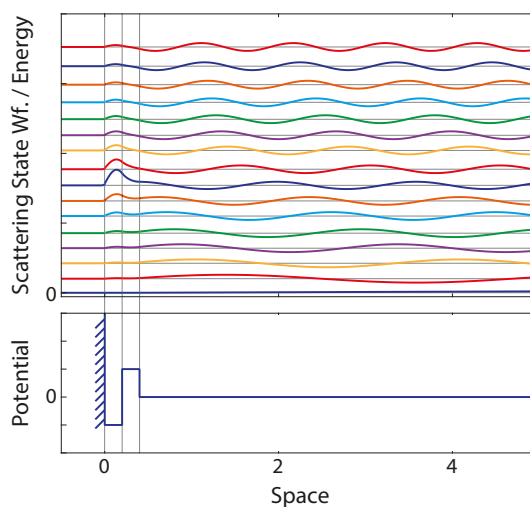


Figure 6.1: Above threshold resonance in a model potential. Initial bound states (not shown) are located close to the origin. The effective photoelectron potential does not support bound states. The scattering state vacuum amplitude is normalized, and the states shifted by their energy. Above a certain energy, the scattering states penetrate the potential barrier and show an increased probability density inside the well, which overlaps with the initial states. Therefore, the transition matrix element is increased and a resonance is observed in the photoemission cross-section. A real atomic potential calculation can be found in [96].

for surfaces, which will be discussed in chapter 7.

Using the absolute helium reference to examine other gas phase samples is facilitated by streaking a mixture of helium and the investigated sample. With helium being an inert gas, no interaction between the two species occurs for common target pressures and temperatures. If all features of interest can be spectrally separated, the relative streaking delay can be extracted from the combined spectrograms and gauged by the absolute helium offset. If substantial spectral overlap of the species cannot be avoided or its effects mitigated, helium can still be used as a reference by assigning the photoelectrons to coincidentally detected photoions [98]. Afterwards one can also use the gauged species as a new absolute reference if helium is not fit for an experiment, though at the cost of slightly increased uncertainty.

6.1 Measurement of the Absolute Iodine 4d Photoemission Delay

Experiments were performed in the attosecond laboratories of the Technical University of Munich. Because iodine does not occur in atomic form naturally, we performed photoemission timing measurements on iodine-containing molecules. To quantify eventual delay differences stemming from the molecular attachments, we measured and examined

the timing of iodomethane (CH_3I) and iodoethane ($\text{C}_2\text{H}_5\text{I}$) which were bought from commercial suppliers (Sigma-Aldrich, Inc., I8507 and I7780).

6.1.1 Preparation of Gas Mixtures

Both iodoethane and iodomethane are liquid at room temperature, but build up sufficient vapor pressure to perform a gas phase experiment. Before transferring the harmful molecules to a vacuum-capable reservoir connected to the beamline, the liquids were cooled to -20°C to reduce their vapor pressure. The molecules were then frozen by cooling the container using liquid nitrogen and the remaining trapped air was removed. Subsequently, the samples were purified by continuously evacuating the reservoir while warming up to room temperature. A large volume of gas mixture was prepared before the timing measurements to maintain a constant helium-to-molecule ratio and backing pressure during the experiment. For this purpose, molecules were filled up to their vapor pressure into a large bottle and then diluted with helium. The helium-to-molecule ratio was chosen such that the photoelectron yields from the iodine 4d orbitals ($[\text{I}]4d$) and direct helium 1s emission ($[\text{He}]1s$) were comparable.

6.1.2 Laser, Beamline, and Electron Detection Setup

The attosecond beamline at the Technical University of Munich is driven by a modified commercial Femtopower oscillator and amplifier with custom white-light generation, see appendices B.3 and B.4. High-harmonic radiation was created in a neon gas target and attosecond pulses synthesized via intensity gating. Spectral filtering was achieved using a 150 nm zirconium foil and a near normal incidence $\sim 5^\circ$ reflection from a multilayer band-pass filter. This setup is stable against detuning due to tilting (1 eV detuning requires $\sim 10^\circ$ deviation). Therefore, the XUV photon energy was not calibrated in-situ. The experiment was performed at two central photon energies, 92 eV achieved using a molybdenum/silicon mirror and 105 eV utilizing a lanthanum/molybdenum mirror. These energies are directly at and ~ 11 eV next to the giant dipole resonance in iodine. A new time-of-flight electron spectrometer was assembled to detect photoelectrons. Due to a high voltage electrostatic lens, its acceptance angle can be increased uniformly for the whole energy region accessible by high-harmonic radiation. Details can be found in [99]. We detected electrons emitted into a cone of $\sim 10^\circ$ (full angle) around the XUV and streaking laser polarization. Because the molecules in the experiment were not oriented, only measurement induced angle effects could have affected the photoemission delay. These are only expected above $\sim 30^\circ$ deviation from the streaking polarization axis [14], i.e., not in the current experiment.

Photoelectron spectra of both molecules with and without helium recorded using the measurement attosecond XUV pulses are shown in figure 6.2, more accurate spectral investigations are available in [100–103]. The spin-orbit-splitting between $[\text{I}]4d_{5/2}$ and $[\text{I}]4d_{3/2}$ and spectral differences between CH_3I and $\text{C}_2\text{H}_5\text{I}$ are not resolved due to the high XUV bandwidth required for the delay measurements. Two main components make up the molecules' photoelectron spectra, a weak and broad composite feature emitted

from molecular orbitals above ~ 14 eV binding energy and the [I]4d peak around 57 eV binding energy. The molecular orbital to [I]4d cross-section ratio is slightly higher at 92 eV photon energy, which is expected when extrapolating data from [103]. For 105 eV central photon energy, the $N_{4,5}VV$ Auger emission is found below ~ 30 eV kinetic electron energy [102], for 92 eV photon energy the Auger electrons overlap with the [I]4d peak on the low energy side. Individual Auger lines are not resolved because the feature is formed by a zoo of different lines spread over 5 eV bandwidth [102, 104]. For pure helium, we find the [He]1s peak at ~ 24.6 eV binding energy. Furthermore, helium shake-up photoemission and double ionization are expected to occur. These are not visible due to their small cross-section and because the electrostatic lens was not set to amplify the shake-up energy region.

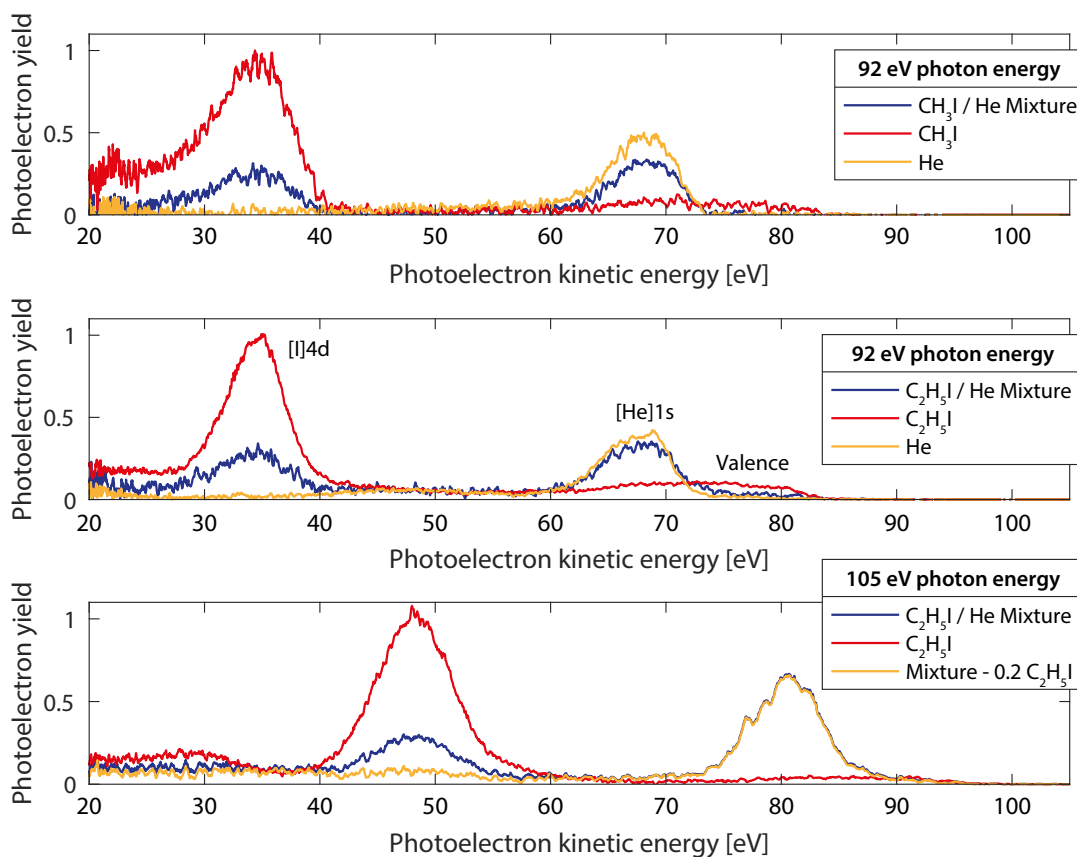


Figure 6.2: Experimental spectra recorded at 92 eV and 105 eV central photon energy for iodomethane, iodoethane, helium and mixtures thereof.

6.1.3 Data Retrieval and Statistical Evaluation

We collected ~ 50 streaking measurements for each molecule and central photon energy. An exemplary streaking spectrogram of a He/ $\text{C}_2\text{H}_5\text{I}$ mixture recorded at 105 eV photon

energy and its retrieval are shown in figure 6.3. All spectrograms were analyzed using the

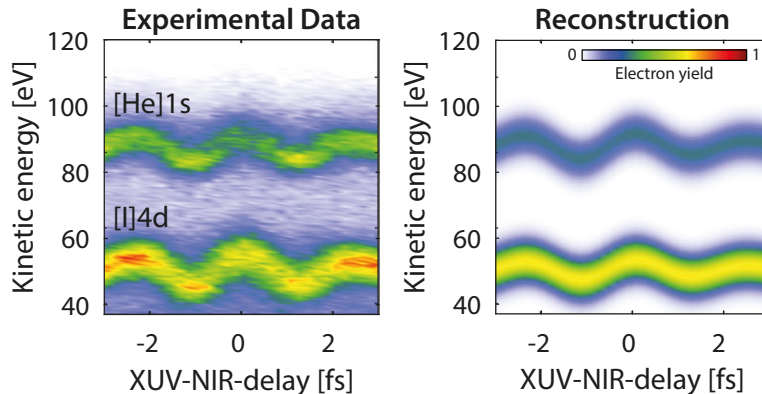


Figure 6.3: Exemplary streaking spectrogram of a He/C₂H₅I mixture at 105 eV central photon energy and its restricted TDSE reconstruction. The relative delay retrieved from this individual measurement is $\Delta\tau_{[I]4d-[He]1s} = 19$ as.

restricted TDSE retrieval algorithm that was also employed in the pure helium experiment. The spin-orbit-split [I]4d peak was represented by a double feature with coupled delay and chirp, defined using synchrotron data [101], and the [He]1s peak was modeled as an isolated feature. Background electrons were subtracted using the differential method to exclude experimenter influence (described in appendix A.7). Attosecond pulse chirp influence was accounted for, but only yields minor changes (<1 as). All individual results are summarized in figure 6.4, means and uncertainties assuming a normal distribution of the individual values are found in table 6.1. We find a significant delay between electrons emitted from [He]1s and [I]4d orbitals, with helium photoemission preceding that from iodine in all examined cases. Furthermore, the delay is increased on-resonance. The [I]4d-[He]1s timing of CH₃I and C₂H₅I coincides within the standard error at both photon energies. Delays induced by scattering of the photoelectrons from their parent ion can thus at most have subsidiary effect in the angle-integrated photoemission delay. It should however be noted that these could still significantly change the angle-resolved delay, see section 6.2. In the following, measurements for both molecules will therefore be conflated.

6.1.4 Estimation of Molecular Orbital and Shake-Up Influences

Spectral overlap of helium shake-up electrons and photoelectrons from molecular orbitals with the examined [I]4d and [He]1s peaks cannot be avoided due to the XUV bandwidth necessary to achieve attosecond time resolution. During the experiments, we controlled our helium to molecule gas ratio to keep all foreign electron contributions below 10 % of the respective examined feature. According to the weighting of our retrieval method (see figure A.2), this limits their influence on the examined delays to below 4 %. Combined with a small shake-up photoemission delay and no expectation of an extreme molecular

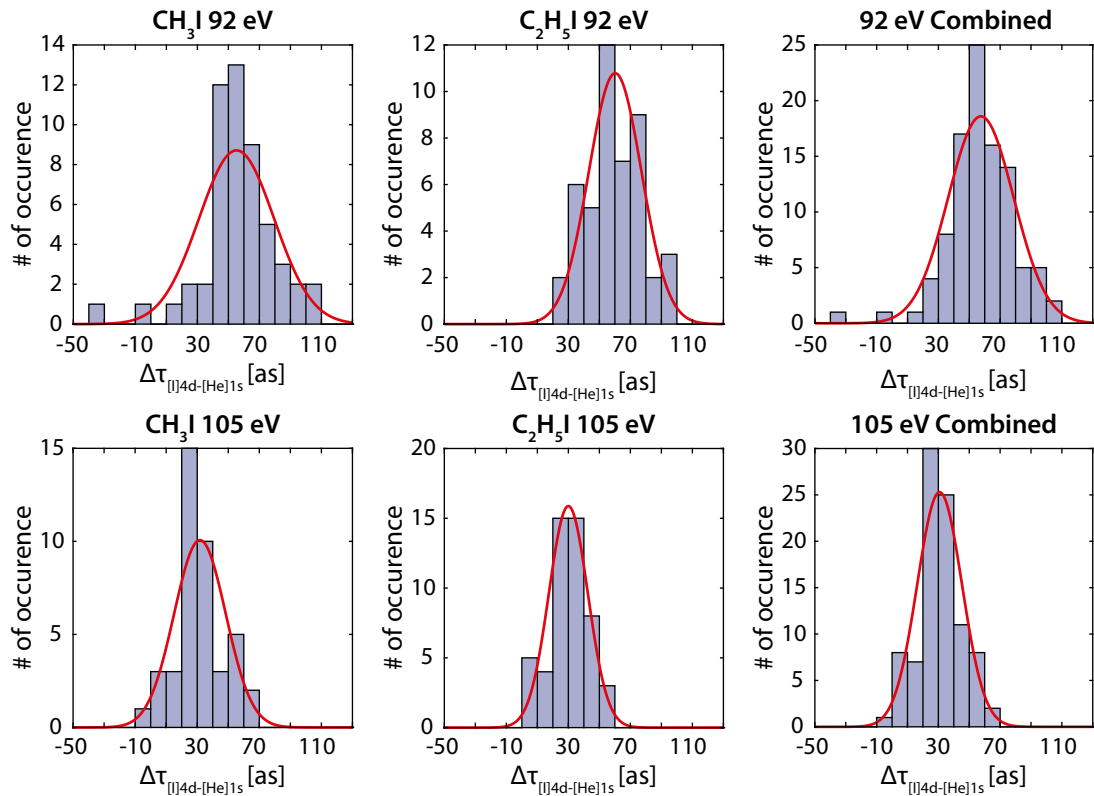


Figure 6.4: Experimental [I]4d-[He]1s delay distributions. Histograms of the individual measurements (blue areas) and normal distribution fits (red lines).

photon energy [eV]	molecule	# of scans	$\Delta\tau_{[I]4d-[He]1s}$ [as]	std. deviation [as]	std. error [as]
92	CH ₃ I	53	55.2	24.3	1.8
92	C ₂ H ₅ I	46	60.2	17.0	2.6
105	CH ₃ I	42	31.7	16.6	2.6
105	C ₂ H ₅ I	50	30.0	12.6	1.8
92	all 92 eV scans	99	57.5	21.3	2.2
105	all 105 eV scans	92	30.8	14.5	1.6

Table 6.1: Experimental averages and uncertainties for the [I]4d-[He]1s photoemission delay.

orbital delay at the employed photon energies, this should not yield deviations beyond the standard error of the relative delay. To verify this experimentally, we varied the ratio of helium to C_2H_5I , changing the relative peak intensities by up to a factor of four. The results of this variation are plotted in figure 6.5. A fit to the data reveals no deviation out of the standard error when extrapolating to either a helium- or an iodine-dominated spectrum. We therefore find no impact of the mix ratio on the measured photoemission delays in a large interval on each side of the measurement setting, confirming that the influence of overlapping electrons on the examined features is negligible.

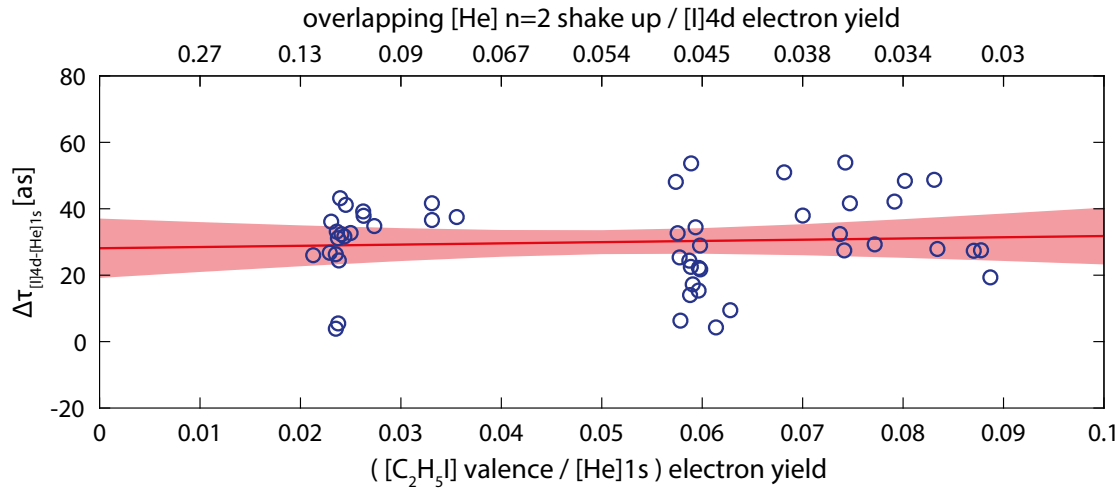


Figure 6.5: Mixing ratio dependence of the C_2H_5I [I]4d to [He]1s photoemission delay at 105 eV photon energy. Individual measurements (blue circles), a linear fit (red line) and the 95 % confidence interval of the fit (red shaded area) are shown.

6.1.5 Estimation of Auger Influence

The Auger feature overlapping with [I]4d photoemission at 92 eV excitation energy is more precarious, not due to its amplitude but its high delay. Although the streaking effect is suppressed for long electron wave packets, a time-dependent signature is still occurring for few-fs long electron wave packets (see appendix A.1). This modulation has already been used to examine a core-hole lifetime and the associated Auger process speed [105].

We investigated the error introduced due to this Auger admixture at 92 eV photon energy by generating streaking spectrograms replicating experimental conditions, which consist of the [I]4d and the overlapping Auger electron feature. We then retrieved the delay change due to the Auger peak using the experimental retrieval algorithm. Auger electron streaking was modeled using equation (4.11) and an exponentially decaying time domain electron wave packet, justified by the Lorentzian spectral shape of the Auger emission. Figure 6.6 illustrates isolated Auger electron streaking for exemplary lifetimes.

The measured linewidth of the individual vibrational features in the molecules' 4d emission is ~ 320 meV, hinting at a minimum core-hole lifetime of 2.1 fs [101]. This is significantly broader than the value measured in other iodine-containing compounds [106], possibly due to other broadening mechanisms. For core-hole lifetimes between 1.6 fs (400 meV natural linewidth) and 6.6 fs (100 meV natural linewidth), we find a maximum increase of the retrieved [I]4d photoemission delay of 5.2 as. At the reported linewidth of 320 meV, we see a change of 4.2 as. To safely account for this deviation, we extend the lower error bar at 92 eV photon energy by 5.2 as.

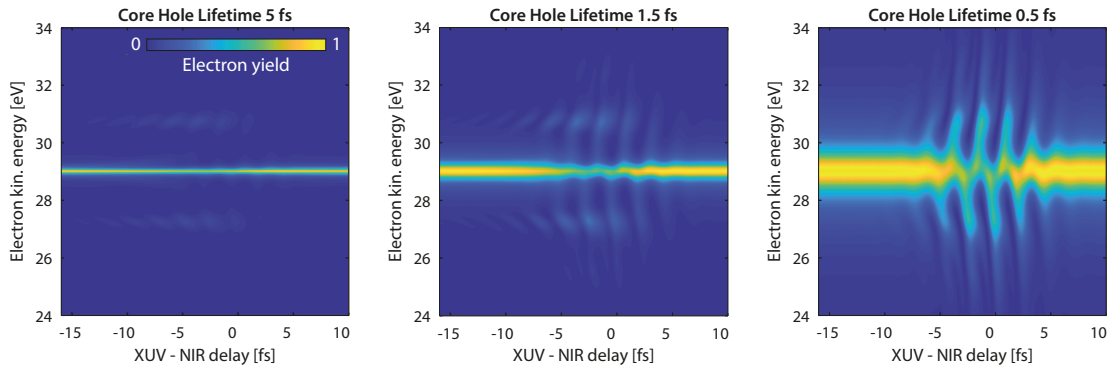


Figure 6.6: Simulated streaking of Auger electrons ejected during the filling of core holes with different lifetimes. The streaking signature is distorted due to the asymmetric wave packet shape. Time structure is suppressed for long core-hole lifetimes, but still discernible at 5 fs lifetime.

6.1.6 Absolute Streaking and Wigner Delay for Iodine 4d Photoemission

We use the established helium reference to transfer the [I]4d delay onto an absolute timescale. From figure 5.12 we find an absolute streaking delay of direct helium photoemission of -6.1 as at 92 eV photon energy and -5.0 as at 105 eV. Due to the low photon energy dependence of the direct helium photoemission delay, uncertainties due to an imperfect photon energy calibration are limited to <0.1 as. Consequently, the absolute streaking delay for [I]4d photoemission is slightly decreased compared to the measured relative delay. Figure 6.7 illustrates the absolute delay determination for 92 eV photon energy.

The measurement dependent CLC contribution does not contain information about the sample and can therefore be subtracted to isolate the [I]4d specific EWS delay. We determine the CLC delay from an ab-initio simulation of hydrogen photoemission streaking and the error assuming a generous uncertainty of ± 1 eV in the photon energy calibration. The [I]4d EWS delay can then be isolated from the relative streaking delay $\Delta\tau_{[I]4d-[He]1s}$ using the absolute [He]1s delay, the CLC delay, and equation (6.1). All values are summarized in table 6.2. The energy dependence of the isolated EWS delay is increased by the high energy dependence of the CLC delay. Opposed to helium, where

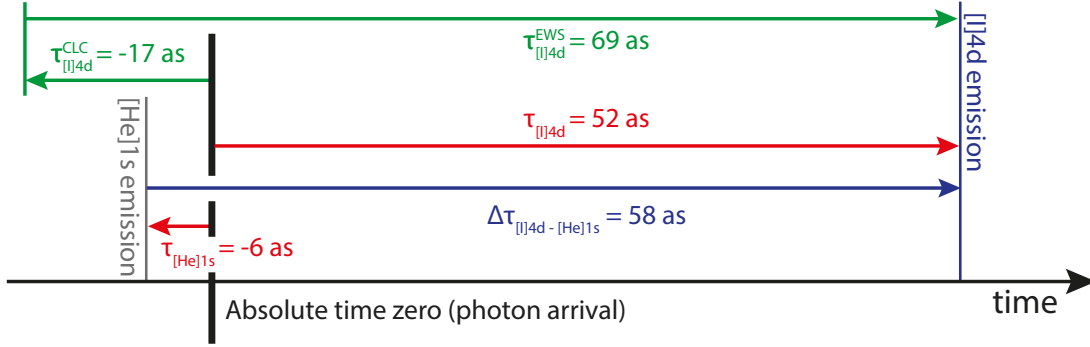


Figure 6.7: Determination of the absolute [I]4d photoemission delay at 92 eV photon energy. Absolute delays are indicated in red, the measured $\Delta\tau_{[I]4d-[He]1s}$ in blue. The [I]4d emission delay consists of the CLC and the EWS contributions (green).

CLC is the main delay contribution, the EWS delay dominates the [I]4d streaking delay in the resonance region.

$$\tau_{[I]4d}^{EWS} = \Delta\tau_{[I]4d-[He]1s} + \tau_{[He]1s} - \tau_{[I]4d}^{CLC} \quad (6.1)$$

photon en. [eV]	$\Delta\tau_{[I]4d-[He]1s}$ [as]	$\tau_{[He]1s}$ [as]	$\tau_{[I]4d}$ [as]	$\tau_{[I]4d}^{CLC}$ [as]	$\tau_{[I]4d}^{EWS}$ [as]
92	$57.5^{+4.3}_{-8.5}$	$-6.1^{+0.1}_{-0.1}$	$51.5^{+4.3}_{-8.5}$	$-17.5^{+0.6}_{-0.7}$	$68.9^{+4.9}_{-9.2}$
105	$30.8^{+3.0}_{-3.0}$	$-5.0^{+0.1}_{-0.1}$	$25.8^{+3.1}_{-3.1}$	$-11.8^{+0.3}_{-0.4}$	$37.6^{+3.4}_{-3.5}$

Table 6.2: Results for the average absolute [I]4d photoemission delay and contributions to it. Error margins represent the 95 % confidence interval.

6.2 Simulation of Photoemission from Small Molecules

To accompany our experimental results and scrutinize photoemission dynamics distinct to the [I]4d shell and molecular components, we performed scattering calculations on photoemission from CH_3I and some smaller iodine-containing molecules. The program ePolyScat [84, 85] was provided by Prof. Dr. Lucchese and has already been employed for the calculation of photoemission delays due to shape resonances in small molecules [10, 86].

It uses wave functions obtained from quantum chemistry codes and the Schwinger variational principle to calculate the continuum electron state after photoemission from an N electron initial to an $N - 1$ electron molecular final state [86], which is then used to calculate the complex transition matrix element. Electron interaction during scattering is treated in the local density approximation [107]. The initial states were determined

using GAMESS-US [108–110], a triple-zeta basis set [111, 112] and a CAM-B3LYP exchange–correlation functional which reproduces the experimental molecule geometry better than the local density approximation [113]. To exclude artifacts due to switching the correlation potential between calculations, we verified the simulations using initial states determined in the local density approximation but find no qualitative difference. ePolyScat employs a spherical harmonics expansion for the description of states and transition matrix elements. To focus precision on [I]4d photoemission, we centered the expansion around the iodine atom and expanded to a maximum angular momentum of 55, achieving a normalization error of less than 0.03% for all orbitals except the [C]1s orbital, for which the normalization error is <0.9%. However, results do not change significantly when only expanding to a maximum angular momentum of 22. The post-processing suite ePSproc [86] was modified to calculate the molecular frame photoelectron angular distributions, whose phase contains the photoemission delay. Because our experiment was conducted with fixed XUV polarization and electron detection angle, but unoriented molecules, we rotated all unique (using molecular symmetries) laser polarizations into the molecular frame and obtained the photoemission amplitude and phase along this direction. We tested our delay retrieval routine and frame definition for atoms and molecules of different symmetry. For simple (helium) to complicated (xenon) atoms, we find uniform emission along the laser polarization direction for all molecule to polarization angles, expectable due to their spherical symmetry. The predicted EWS delay for direct helium photoemission is in good agreement with more advanced time-dependent calculations, see figure 5.12. The difference of the relevant frame to a molecular or laboratory frame is probably most evident in this case: Photoemission from most atoms is known to be angle-dependent, with the exact characteristic often described using the β -factor. This is such because the observed emission angle is varied relative to the polarization angle of the emitting radiation. In the current case, no angle dependence is occurring because electrons are always detected along the polarization axis. For molecules with C_∞ symmetry, we find angle dependence for molecule orientations in the plane defined by the polarization axis and the molecular axis. All other rotations are equivalent to a rotation around the molecule axis and thus indiscernible. CH₃I has C_{3v} symmetry, i.e., three-fold mirror plane symmetry and hence retains two relevant rotation angles.

The molecule-orientation-dependent photoelectron distribution and photoemission delay for emission along the direction of XUV polarization of the [I]4d orbitals in CH₃I at 105 eV photon energy are shown in figure 6.8, along with the angle definition and projections. The three-fold molecular symmetry is reproduced in the photoelectron distribution due to scattering of the photoelectron with the parent ion. The delay weakly reflects the three-fold symmetry of the CH₃I molecule. Along the other rotation, a stronger influence is caused by scattering of the outgoing electron wave packet from the molecule. It increases the photoemission delay for electron exit along the molecular axis, with a maximum increase of up to ~ 39 as in a small angle range when exiting through the methyl group. At low photon energies, the angular dependence of the photoemission delay is increased, suggesting that the angle-dependent photoemission delay of low kinetic energy electrons could be used as attosecond probe for the molecular potential in the

instants after photoemission.

Because we did not align molecules in the experiment, we calculated the incoherent weighted average over all relevant rotations to obtain photoemission cross-sections and delays comparable with experimental data. These are shown in figure 6.9 and discussed further down.

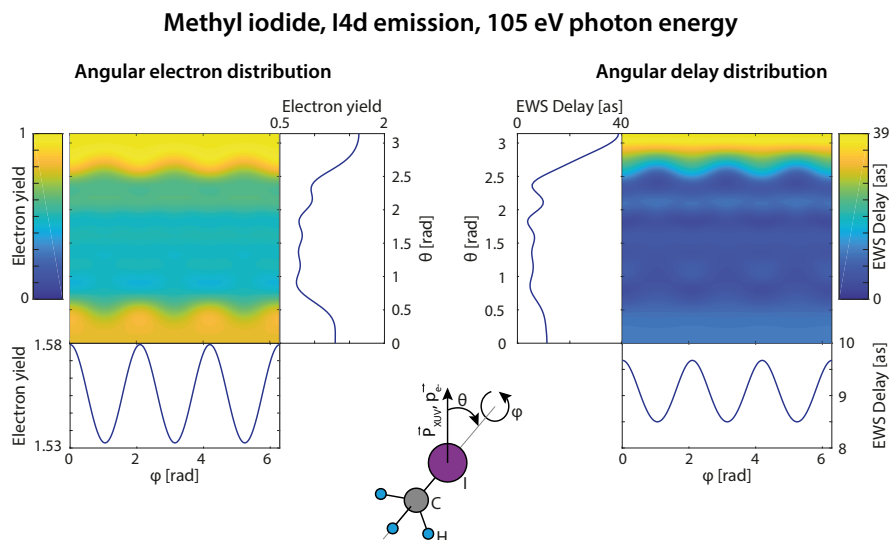


Figure 6.8: Simulated polarization-molecule angle-dependent 105 eV photon energy photoemission cross-section and delay from the [I]4d orbitals in CH_3I for electrons exiting in direction \vec{p}_e along the XUV polarization axis \vec{P}_{xuv} and integrals over the two relevant rotation angles.

6.3 Time Domain Evaluation of the Giant Dipole Resonance in Iodine

The measured EWS delay can be compared to the EWS delay of a hydrogenic system to work out the effects of the giant dipole resonance. Using equation (3.9), one finds hydrogenic delays of 7.5 as (92 eV) and 4.6 as (105 eV) for emission into an f-wave and 2.9 as (92 eV) and 1.7 as (105 eV) for emission into a p-wave. The giant dipole resonance increases the EWS delay compared to a pure hydrogenic sample at least eightfold and dominates the photoemission delay in the resonance region.

Eisenbud already examined the trapping effect of resonances on the scattering delay in his thesis and predicted that a resonance with Breit-Wigner (Lorentzian) cross-section profile causes a scattering delay of twice the lifetime of the compound state [29, p. 92]. He considered the Eigenphase, which might have introduced a factor of 1/2 compared to this work's phase definition. Current publications find a time delay of four times the lifetime when considering scattering of a particle from a potential, i.e., twice that

of Eisenbud [114]. Because the uncertainty principle governs the lifetime, it is given by the inverse of the resonance's breadth when ignoring other broadening mechanisms. Therefore, the scattering delay can be estimated from the resonance width.

A discussion in the context of photoemission delays can be found for photoemission through an autoionizing state [115, 116]. Such states cause Fano-shape resonances in the photoemission cross-section of most atoms, however, these are spectrally narrower than the giant dipole resonance. Altogether, it should be considered that the presented discussion is stemming from the treatment of narrow resonances and deviations might occur at the extreme width of the giant dipole resonance. Because a Breit-Wigner shape is captured by the Fano framework in the infinite asymmetry parameter limit, only the latter will be presented. For a single resonance at energy E^{res} , with width Γ , a Fano asymmetry parameter, i.e., the ratio of the autoionizing and direct transition probabilities to the continuum, q and amplitude σ^{res} , the energy dependence of the cross-section is described by [117, 118]:

$$\sigma(E) = \sigma^{\text{res}} \frac{(q + \epsilon)^2}{1 + \epsilon^2} \quad \text{with} \quad \epsilon = \frac{E - E^{\text{res}}}{\Gamma/2} \quad (6.2)$$

Disregarding the phase due to the initial excitation into the autoionizing state and only treating emission into the dominating partial wave, the photoemission delay τ^{res} caused by the resonance is given by the energy derivative of the transition matrix element between the autoionizing state and the continuum.

$$\tau^{\text{res}}(E) = \frac{\partial \arg(D(E))}{\partial E} = \frac{1}{(1 + \epsilon^2)} \frac{1}{\Gamma/2} \quad \text{with} \quad D(E) \propto \frac{q + \epsilon}{i + \epsilon} \quad (6.3)$$

Following this line of arguments, the delay is independent of the q-factor, has Breit-Wigner-shape and reaches its maximum of twice the inverse resonance width at the resonance energy. Returning to the half-scattering picture for photoemission, this corresponds to a complete scattering delay of $\Gamma/4$, i.e., the quadruple lifetime. The [I]4d photoemission cross-section is available from literature [97, 102]. These and fits to the reported [I]4d cross-sections are plotted in figure 6.9. The literature cross-section measurements scatter in bandwidth, central energy, and amplitude. Furthermore, the shape is not satisfyingly representable using a Fano profile. Nonetheless, to gain an estimate for the expectable magnitude of the photoemission delay caused by the [I]4d giant dipole resonance, figure 6.9 also shows the emission delay calculated using the fit data and equation (6.3). The best fit q-factors are ~ 10 , which suggests that most electrons exit the iodine atom through the resonance and direct transitions to the continuum are unlikely. Therefore, close to all cross-section in the resonance energy region can be attributed to the $4d \rightarrow \epsilon f$ channel because the $4d \rightarrow \epsilon p$ channel cannot exhibit a resonance and its cross-section decreases monotonously above the threshold [119]. As a comparison, the delay of hydrogenic emission into an f-wave, calculated using equation (3.9), is also shown. While this simple model reproduces the general trend of the observed photoemission delay, no quantitative agreement is found. The model underestimates the delay at resonance by at least 11 as.

We now apply the same discussion to the simulated half-scattering delays. The calculated angle-integrated CH_3I photoemission cross-section is dominated by the giant

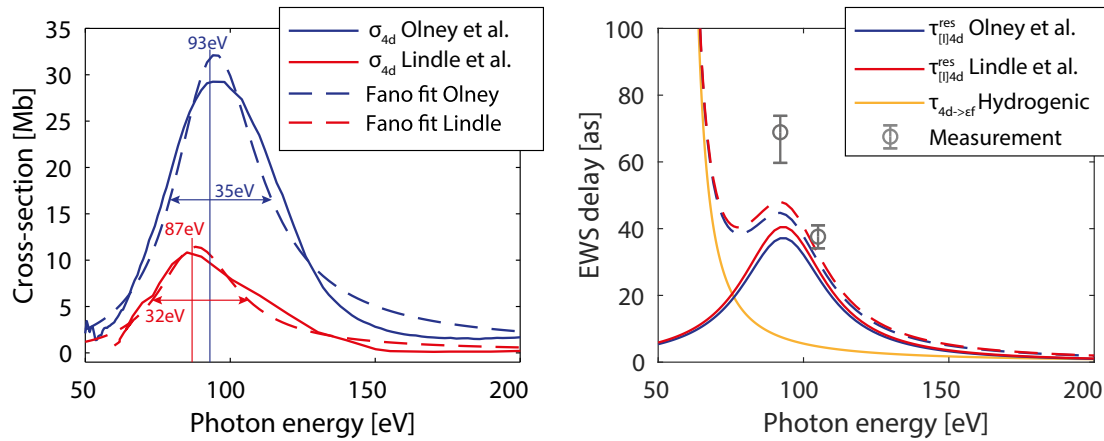


Figure 6.9: Left panel: the angle-integrated photoemission cross-section for [I]4d electrons σ_{4d} in CH_3I from electron energy loss spectroscopy (blue) [97], photoelectron spectroscopy (red) [102], and least-squares fits of a Fano profile to the data. Right panel: the EWS delays calculated using cross-section fit parameters and equation (6.3) (red and blue lines), as well as the hydrogenic EWS delay for a $4d \rightarrow \epsilon f$ transition (yellow line) and sums (dashed). The measured EWS delay shape (grey) is reproduced but the magnitude underestimated. Error bars represent the sum of the 95% confidence interval and the maximum deviation due to photon energy uncertainty.

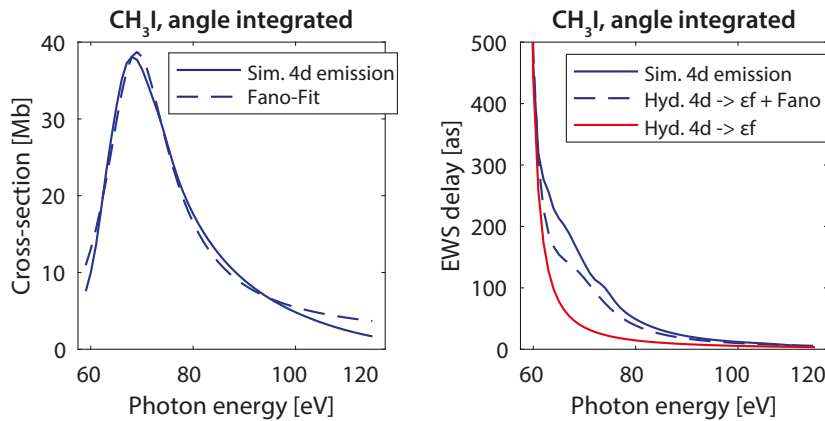


Figure 6.10: Left panel: simulated angle-integrated photoemission cross-section (blue line) showing the giant dipole resonance and a Fano-model fit to the cross-section (blue dashed line). Right panel: simulated angle-integrated photoemission delay of [I]4d in CH_3I (blue line), as well as the hydrogenic delay prediction for emission into an f-wave (red line) and the sum of the hydrogenic prediction and the delay expected from the Fano-model fit to the resonance in the cross-section (blue dashed line).

dipole resonance at 68 eV photon energy. Unfortunately, the resonance appears at lower photon energy than in the experiments and with roughly half of the linewidth. The best fit q -factor is also lower than in the experiment but still confirms that emission is happening prevalently through one channel. This discrepancy between experiment and theory has been observed before and can only be overcome by the inclusion of interchannel-coupling [120]. However, trends in the time delay of the resonance and the self-scattering of photoelectrons from the parent molecule can still be examined. The angle-integrated photoemission delay (figure 6.10) at low energy is reproduced by the hydrogenic approximation for $4d \rightarrow \epsilon f$ emission. The giant resonance determines the photoemission delay at intermediate electron energies until the delay again approaches the hydrogenic prediction for $4d \rightarrow \epsilon f$ at high photoelectron energies. The minor unevenness of the delay is caused by scattering from molecular orbitals and disappears in the angle-integrated delay at higher energies. It should thus be negligible at the photon energies used in the experiment.

In the intermediate region, we fit equation (6.2) to the cross-section to estimate the delay introduced by the giant dipole resonance (although this certainly is not comparable with experimental data, it is still interesting to check if the Fano approach reproduces the simulation). The resulting resonance delay is underestimated by $\sim 30\%$. To distinguish if this discrepancy is caused by scattering from molecular orbitals or applying the Fano-model is oversimplifying the giant dipole resonance delay, we performed further simulations. We examined an isolated xenon atom, whose 4d photoemission behavior is conformable to that of iodine, and diatomic molecules containing iodine which cause maximum charge distortion at the iodine atom (iodine monofluoride, lithium iodide, hydroiodic acid). While not changing the delay magnitude, these allow to enhance and modify the angle-resolved molecular scattering delay, though only minorly change the angle-integrated delay at photon energies beyond 30 eV above the threshold. Xenon shows no additional structure due to scattering off molecular constituents, and the delay shape can be modeled using the hydrogenic and a resonance delay. Nonetheless, the Fano cross-section fit underestimates the resonance delay in all cases, again by 25% to 35%. Peculiarly, a correction of the resonance delay estimation by this magnitude also unifies the experimental delay measurements and the delay predictions from experimental cross-sections in figure 6.9. This trend suggests a more complicated resonance structure than grasped by the simple model, which ignores interchannel coupling and correlation effects.

There is still considerable research interest focused on understanding the mechanism behind the giant dipole resonance. Reports on iodine-similar xenon predict two resonances contributing to the overall giant dipole resonance shape [121] and theoretical papers that focus on the photoemission delay find conflicting values ranging from -16 as to 42 as at the resonance [122, 123]. Furthermore, a recent paper finds two-photon effects in the photoemission delay of autoionizing resonances, which could also apply to the iodine giant dipole resonance delay but require insight in the radiative coupling of the autoionizing state to the continuum [116]. Because giant dipole resonances do not evolve through a distinct separate state, transferring the reported two-photon delay is not straightforward.

We explored the absolute photoemission timing of the giant dipole resonance in iodine. So far, only the photoemission cross-section was available to benchmark and tune theoretical models describing giant dipole resonances. The current measurement provides phase access as an alternative way to contemplate the nature and mechanism behind giant dipole resonances. It reveals that electron emission is significantly delayed by them, which suggests a resonance origin that can be assigned a lifetime. The Fano framework describes the energy dependence of this delay increase, however, quantitative disagreement highlights the complexity of the resonance. From molecular scattering simulations, we find that the angle-dependent photoemission delay from molecules probes the local potential traversed during the electron exit. The photoemission delay of oriented molecules can therefore be employed as a non-equilibrium probe into the dynamics during photoionization.

Chapter 7

Absolute Timing of Condensed Matter Photoemission and Adsorbates

The first reported photoemission timing measurement was performed on a crystal surface [6]. Using the attosecond streak camera, Cavalieri et al. determined the photoelectron exit timing from the 110 surface of a body-centered-cubic tungsten crystal. They found that electrons created by a 92 eV XUV light pulse exit the crystal faster by ~ 100 as when they originate from the conduction band than when they are escaping from a tungsten 4f core level. The setup used in this and many subsequent crystal timing experiments is sketched in figure 7.1.

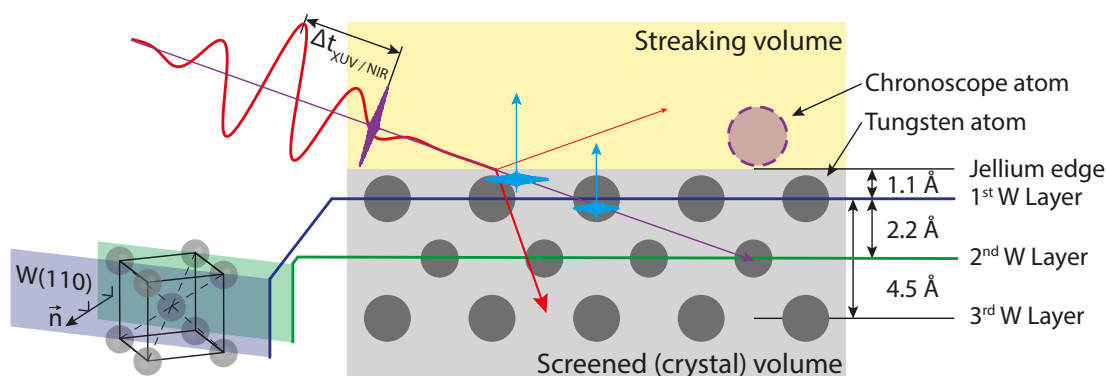


Figure 7.1: Attosecond streaking at a crystal surface. The streaking laser pulse (red) is reflected and refracted at the crystal surface resulting in a negligible streaking field along the surface normal inside the crystal. The XUV pulse (purple) is negligibly influenced by entering the solid. It creates electron wave packets (light blue) that travel towards the crystal surface but only start streaking upon passing the Jellium edge. Depending on the depth of the electron origin within the crystal, the electron movement towards the streaking volume causes a transport delay. The crystal cut corresponding to the W(110) surface is also illustrated. In the case of an absolute measurement, atomic chronoscopes (purple dotted) are adsorbed into the streaking volume above the crystal surface such that electrons originating from the chronoscopes do not experience a transport delay.

In a metallic crystal, the streaking field perpendicular to the crystal surface is highly suppressed due to reflection and refraction. The depth at which the streaking field is effectively negligible is on the order of one crystal layer spacing [19, 124]. Delays in the photoemission from a metal surface are thus much more intuitively understandable than from an atom or molecule because there is a spatial separation between the streaking volume and the photoelectron origin. Electrons travel undisturbedly inside the crystal and only start streaking upon their exit, which makes the attosecond streak camera an invaluable tool to examine the nanoscopic electron transport inside a solid [19], electron scattering in metals [21] and dielectrics [20] or band structure effects [22]. A recent study found that EWS delays originating from the atomic potential can still occur inside a solid, closing the bow to the atomic case [125].

All these measurements are relative, either comparing several initial states or photon energies due to the reason described in section 4.2.5: Being pump-probe, an absolute measurement of crystal exit delays requires precise knowledge of the experimental laser and XUV pulses. First pushes to resolve this source of ambiguity used a spatially separated streaking experiment to perform a delay calibration up to a constant offset in a gas phase streaking experiment and subsequently refocused both laser pulses onto a solid target [126, 127]. However, propagation [126, 127], Gouy phase effects [128, 129] and field distortions due to reflection off the surface limit the accuracy of this technique to a few tens of attoseconds, on the order of the crystal exit delays expected at ~ 100 eV photon energy.

7.1 The Atomic Chronoscope Method

It is not possible to directly transfer an absolute clock as described in chapter 6 to a crystal by flowing helium over its surface because the streaking volumes of the gas and crystal surface would differ and Gouy effects would cause significant errors. We therefore introduce and apply the atomic chronoscope method, which can determine absolute surface photoemission timing while maintaining errors below 10 as by transferring the absolute helium reference onto the surface using a two-step experiment. First, atomic adsorbates are placed on the surface and mark the light pulses' arrival time to up to the atomic photoemission delay from the reference orbital. All propagation and reflection effects are eliminated by placement of the reference in the surface's streaking volume. This chronoscope scheme is also indicated in figure 7.1.

The constant reference orbital photoemission delay offset from the light pulse arrival is then determined and corrected in a gas-phase gauge measurement by comparing the chronoscope species to [He]1s photoemission. We chose using atomic iodine chronoscopes on the W(110) surface to maintain comparability to the initial streaking experiment [6]. The central examined photon energy was slightly increased to 105 eV which avoids overlap of Auger electrons with all relevant photoelectron features. The complete experimental timing scheme is illustrated in figure 7.2. The adsorbate species has to fulfill specific prerequisites to achieve a meaningful atomic chronoscope measurement: The chronoscope atoms must offer a core level that is accessible by photoemission spectroscopy using

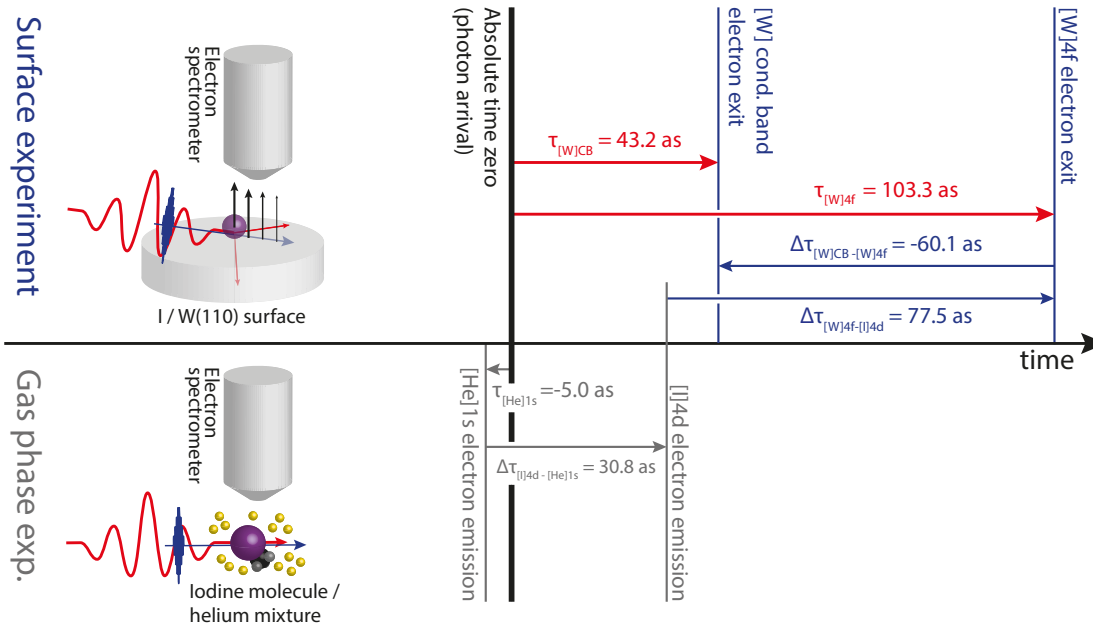


Figure 7.2: Left part: experimental streaking schemes. Right part: full timing sequence of the atomic chronoscope experiment. Surface delay measurements are illustrated in blue, gas-phase measurements in grey. The absolute results are indicated in red. Initial publication in [130].

XUV radiation at the desired photon energy and spectrally separable from all examined photoemission features of the crystal to pose as unambiguous reference. Valence levels are unfit because the formation of molecular orbitals can change their EWS delay. Possible influences of the chronoscopes on crystal photoemission timing due to a shift of the streaking volume due to screening can be minimized by using a dielectric chronoscope overlayer. Furthermore, to quantify effects of the overlayer on the surface timing, the reference level needs to exhibit high enough photoionization cross-section to support measuring photoemission delays for varying surface coverages of the adsorbate. The coverage dependent photoemission delay then contains the chronoscope influence and extrapolation to zero surface coverage can exclude residual effects.

7.2 Experimental Photoemission Timing of I/W(110)

The coverage dependent photoemission delay of atomic iodine adsorbates on a tungsten W(110) surface was investigated in collaboration with Johann Riemensberger during my master's thesis [131, 132], the findings of which will be combined with chapters 5 and 6 to obtain the absolute timing of a W(110) surface. The following will hence only briefly outline the surface experiment before focusing on the results enabled by the introduction of an absolute scale.

Using iodine as chronoscope species and [I]4d as reference level fulfills all prerequisites mentioned in section 7.1. The giant dipole resonance increases the [I]4d cross-section in the relevant energy region such that coverages down to a tenth of the tungsten surface density can be reliably detected and their photoemission delay determined. The same considerations are also valid for xenon. However, xenon atoms only adsorb on W(110) below 80 K. The fragile binding and critical temperature dependence combined with the incident streaking laser field prevent meaningful delay measurements below 1 monolayer coverage [82]. Therefore, residual screening effects cannot finally be excluded.

7.2.1 Sample Preparation

Iodine forms a dissociative bond with the tungsten surface which allows maintaining stable sub-monolayer coverages [133, 134]. We fabricated samples by preparing clean W(110) surfaces through argon sputtering, ten oxidation/desorption cycles and finally thermal annealing at 2400 K. Surface quality and cleanliness were ensured via x-ray photoelectron spectroscopy and low energy electron diffraction. Iodine overlayers were grown by dosing gaseous iodine on the surface at room temperature, at which the iodine density saturates at $\frac{7}{12}$ th of the W(110) surface atom density [135]. Saturation provides an intrinsic reference for determining the surface coverage through static photoelectron spectroscopy. After taking a full monolayer calibration spectrum, iodine atoms were gradually removed from the surface by thermal desorption to achieve sub-monolayers. Exemplary electron spectra used in the coverage determination and a clean spectrum are compared in figure 7.3. Three expected effects are occurring along decreasing adsorbate coverage: A decrease in the [I]4d core level photoemission intensity due to decreasing source density, an increase of the [W]4f core level intensity due to decreasing inelastic electron scattering in the overlayer and a shape change of the valence electron feature towards the bare W(110) shape.

7.2.2 Data Retrieval and Statistical Evaluation

Experiments were performed using the FP2 laser system, the AS3 surface beamline (see appendices B.1 and B.6) and the exact 105 eV bandpass mirror as in the gas phase iodine/helium measurements. All data was re-evaluated with the new restricted TDSE algorithm and differential background subtraction to guarantee comparability. The data set consists of 79 streaking spectrograms recorded for 9 individual coverages from a saturated monolayer down to 17% of the saturated surface density. An exemplary spectrogram and its retrieval are depicted in figure 7.4. All individual relative delay results between [I]4d and [W]4f, or valence electron photoemission respectively, are shown in figure 7.5.

Electrons originating from inside the crystal are delayed compared to iodine reference photoemission. The delay between [W]4f core electron exit and [I]4d reference photoemission shows close to no adsorbate coverage dependence, confirming negligible screening of the streaking field inside the overlayer. The weak coverage dependence of the observed

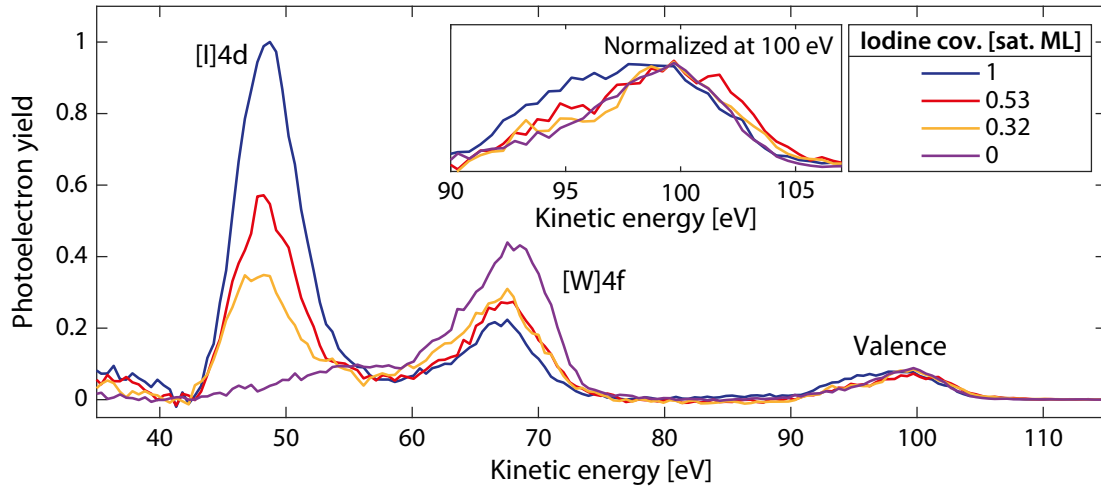


Figure 7.3: Shirley background corrected static photoemission spectra of I/W(110) for three different iodine coverages and a clean W(110) surface. The coverage is measured in units of saturated monolayers (sat. ML). Spectra are normalized to slow secondary electron emission from deep in the crystal. The inset highlights the valence electron feature and is normalized at 100 eV kinetic electron energy to magnify shape changes. Initial publication in [130].

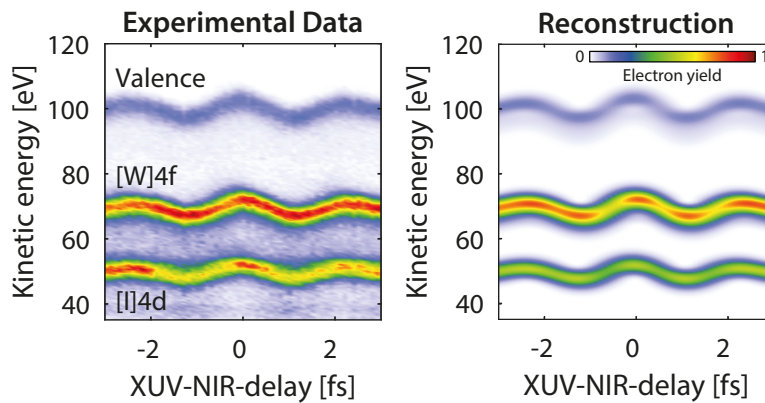


Figure 7.4: Exemplary streaking spectrogram of a I/W(110) surface at 33% of the saturated iodine coverage at 105 eV central photon energy and its restricted TDSE reconstruction. The relative delays retrieved from this individual measurement are $\Delta\tau_{[W]4f-[I]4d} = 81$ as and $\Delta\tau_{\text{Valence}-[I]4d} = 14$ as. Initial publication in [130].

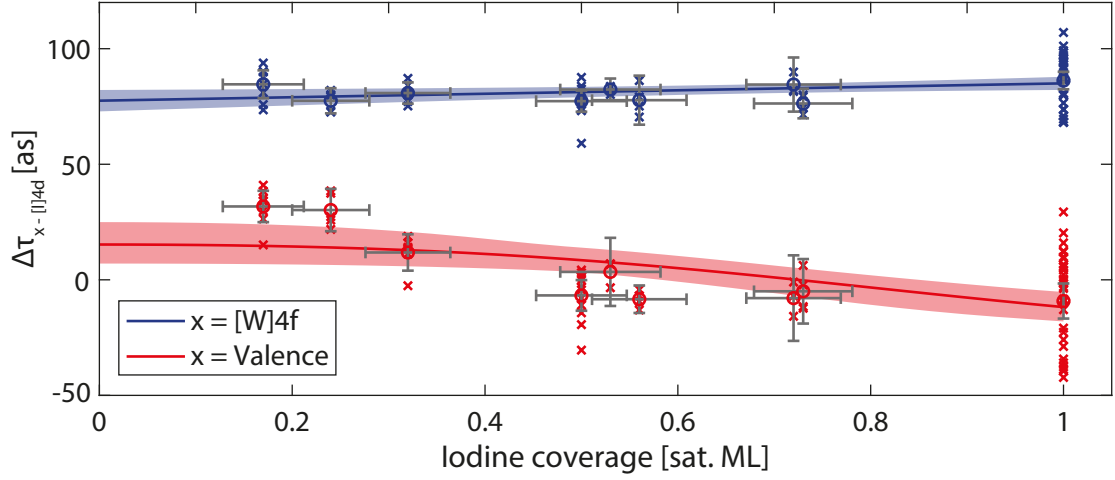


Figure 7.5: Experimental relative photoemission delay for I/W(110). Individual measurements are indicated as crosses, the mean for individual coverages as circles. Vertical error bars were determined assuming a Student t's distribution and represent 95 % confidence. Horizontal error bars represent maximum uncertainty. Lines represent model fits (described in the text) to the data and shaded areas their 95 % confidence interval. [W]4f-[I]4d related quantities are represented in blue, valence-electron to [I]4d related quantities in red. Initial publication in [130].

delay allows describing the relative timing using the linear function

$$\Delta\tau_{[W]4f-[I]4d}(\theta) = (77.5 \pm 4.6) \text{ as} + \theta(7.5 \pm 6.2) \text{ as} \quad (7.1)$$

where θ is the fractional iodine coverage in units of saturated monolayers. Extrapolation to zero surface coverage eliminates residual chronoscope effects on the surface and reveals $\Delta\tau_{[W]4f-[I]4d} = (77.5 \pm 4.6) \text{ as}$ as the [W]4f-[I]4d delay in the negligible iodine coverage limit.

Due to spectral mixing of iodine adsorbate valence states ([I]V) and the tungsten conduction band ([W]CB), the behavior is different for valence electrons. Their emission delay compared to reference photoemission decreases significantly with increasing coverage of the surface. We use equation (7.2) and the coverage dependent intensities $I_{[I]V}(\theta)$ and $I_{[W]CB}(\theta)$ of the constituents to model the valence emission delay. The squared intensities in equation (7.2) account for the weighting of overlapping peaks in the restricted TDSE retrieval (see appendix A.2).

$$\Delta\tau_{\text{Valence-[I]4d}}(\theta) = \frac{I_{[W]CB}^2(\theta)\Delta\tau_{[W]CB-[I]4d} + I_{[I]V}^2(\theta)\Delta\tau_{[I]V-[I]4d}}{I_{[W]CB}^2(\theta) + I_{[I]V}^2(\theta)} \quad (7.2)$$

The best model fit to the data is achieved by $\Delta\tau_{[W]CB-[I]4d} = 15.3_{-8.3}^{+9.7} \text{ as}$ and $\Delta\tau_{[I]V-[I]4d} = -25.1_{-20.7}^{+32.3} \text{ as}$ and is shown in figure 7.5. The given errors include uncertainties in the

iodine valence to tungsten conduction band electron yield ratio. Tungsten [W]4f core emission is delayed with respect to conduction band electron exit by

$$\Delta\tau_{[W]4f-[W]CB}(\theta = 0) = \Delta\tau_{[W]4f-[I]4d}(\theta = 0) - \Delta\tau_{\text{Valence-[I]4d}}(\theta = 0) = 62.2_{-9.5}^{+10.7} \text{ as.} \quad (7.3)$$

To verify the validity of this conduction band exit delay, we furthermore consult measurements performed on a bare W(110) surface using the same XUV bandpass mirror [132, 136]. Those were also re-evaluated using the new retrieval algorithm and yield a relative core to conduction band delay $\Delta\tau_{[W]4f-[W]CB} = (60.1 \pm 5.6)$ as, in good accordance with the zero coverage delay retrieved in equation (7.3).

7.2.3 Estimation of Surface Influences on Iodine 4d Photoemission

Contrary to influences of the adsorbates on the surface, the back-action cannot be minimized by decreasing the adsorbate density. We therefore estimated possible influences theoretically. Hybridization of the chronoscope orbitals could change their emission delay in either the surface or the gauge measurement. The effect should be mitigated by using core orbitals. Nevertheless, we used the quantum chemistry code GAMESS-US [108–110], a triple-zeta basis set [111, 112] and a CAM-B3LYP exchange–correlation functional to calculate the [I]4d orbitals in a W-I and a C-I bond. The resulting orbitals’ overlap integral is greater than 99 %, stressing immunity of the core orbitals. Another difference between the surface and gauge measurement is the orientation of electron detection to the bond angle. The gauge measurements were performed on an unoriented sample, thus average over all possible electron exit angles compared to the iodine bond. When the iodine is adsorbed on a fixed surface, detected photoelectrons are emitted prevalently in the direction opposite to the bond angle. To estimate this effect, we use the angle-resolved scattering simulation for CH₃I, see figure 6.8. We find less than 2 as difference between the angle-integrated delay and electron emission exclusively opposite to the bond. In the experiment, this effect is further mitigated by a slight angle offset between electron detection and bond angle, as well as the finite detector acceptance angle. Furthermore, the giant dipole resonance might be disturbed by the bond, which could influence the resonance delay. Literature reports a general independence of the giant dipole resonance width and amplitude of the iodine’s chemical environment [97, 137] and even ionization state [138]. Because these properties are closely linked to the emission delay of a resonance, a disturbance in the rather comparable chemical environments is unlikely.

7.3 Absolute Timing of Crystal and Surface Photoemission

Absolute emission delays for the crystal surface can now be calculated by adding the reference absolute [I]4d iodine emission delay $\tau_{[I]4d} = (25.8 \pm 3.1)$ as to the relative measurements. Results are summarized in figure 7.6.

For [W]4f photoemission, we find an absolute exit delay from a clean crystal surface $\tau_{[W]4f} = \Delta\tau_{[W]4f-[I]4d}(\theta = 0) + \tau_{[I]4d} = (103.3 \pm 5.6)$ as. The absolute scale allows to directly decompose the delay into its constituents.

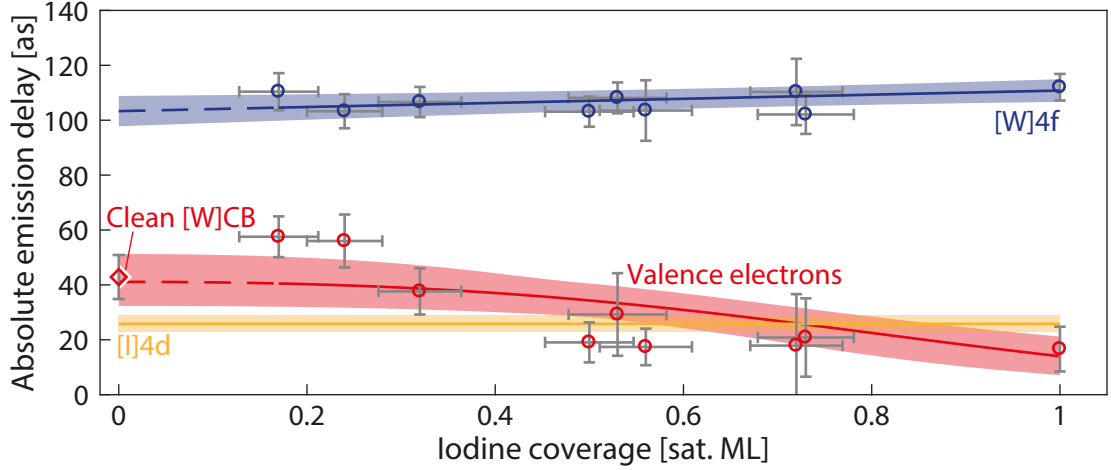


Figure 7.6: Absolute coverage dependent electron exit timing for the I/W(110) surface. The [I]4d reference is represented by yellow, [W]4f emission by blue and the valence feature emission by red symbols. A red diamond represents the result of an alternative method to retrieve the bare W(110) conduction band exit delay, referencing clean tungsten surface timing measurements to the absolute [W]4f timing. Individual coverage averages (circles) and model fits (lines) to the measurements are shown. All errors correspond to 95 % confidence. Initial publication in [130].

The three-step model of solid photoemission [139] separates the process into: first, the birth of the photoelectron, i.e., its excitation into a high-lying Bloch-state within the crystal. Second, its travel to the surface, and last its transmission from the crystal bulk to the vacuum, which changes the electron momentum perpendicular to the surface and is especially important in angle-resolved photoemission spectroscopy. A recent paper showed that intra-atomic EWS delays still apply in solid environments and estimates $\tau_{[W]4f}^{\text{EWS}} = 10$ as at 105 eV photon energy, which accounts for the first step. The remainder of the absolute delay can then be attributed to the transport between the electron origin and the streaking volume, in this case, ~ 93 as for [W]4f electrons. In a semiclassical picture, the chance for an electron to leave the crystal without losing energy due to inelastic scattering, i.e., the chance for an electron to contribute to the main photoemission feature with defined phase, decreases exponentially with its birth distance from the surface [139]. The decay constant λ is called inelastic mean free path (IMFP) and together with the electron velocity v defines the classical transport delay [82]:

$$\tau_{[W]4f}^{\text{transport}} = \frac{\int_0^\infty dx \exp\left(-x/\lambda_{[W]4f}\right) \frac{x}{v_{[W]4f}}}{\int_0^\infty dx \exp\left(-x/\lambda_{[W]4f}\right)} = \frac{\lambda_{[W]4f}}{v_{[W]4f}} \quad (7.4)$$

Cavalieri et al. explained the large observed relative [W]4f-[W]CB delay at 92 eV photon energy using a significantly decreased group velocity for [W]4f electrons due to the crystal

band structure [6]. Because the IMFP in this electron energy region is extrapolated from optical data it is afflicted by uncertainty, estimates for [W]4f electrons excited by our photon energy range from 4.2 Å [140] to 6.0 Å [141]. Assuming free-electron-like dispersion in the solid [82], these IMFPs predict a transport delay of 80 as to 114 as, in good agreement with the observed transport delay. Our results therefore contradict the early hypothesis of Cavalieri et al. for 105 eV excitation photon energy and suggest that [W]4f photoemission is governed by free-electron-like transport.

The absolute tungsten conduction band exit delay can either be determined by extrapolation of the I/W(110) valence electron data to zero coverage or by referencing the relative [W]CB-[W]4f delay from a bare W(110) surface to the absolute [W]4f delay:

$$\tau_{[\text{W}]_{\text{CB}}}^{\text{extrap.}} = \Delta\tau_{\text{Valence-}[I]_{4d}}(\theta = 0) + \tau_{[I]_{4d}} = 41.1_{-8.9}^{+10.2} \text{ as} \quad (7.5)$$

$$\tau_{[\text{W}]_{\text{CB}}}^{\text{bare}} = \Delta\tau_{[\text{W}]_{4f-[I]_{4d}}}(\theta = 0) + \tau_{[I]_{4d}} + \Delta\tau_{[\text{W}]_{\text{CB}-[\text{W}]_{4f}} = (43.2 \pm 7.9) \text{ as} \quad (7.6)$$

The results of both methods agree and reveal an absolute conduction band exit delay on the order of 40 as. No EWS delays have been reported for the tungsten conduction band, but their general trend is to decrease with increasing kinetic energy and smaller angular momentum. Apart from resonances, the magnitude of the conduction band EWS delay is thus likely smaller than that of [W]4f. Using the reported IMFPs (4.1 Å to 5.6 Å [140, 141]), the free-electron-like transport delay for conduction band electrons would amount to 67 as–91 as, significantly exceeding the observed delay. Therefore, using scattering as the lone factor limiting the emission depth from the bulk requires a doubled group velocity of the electron wave packet, which is not justified by calculated tungsten band structures, which predict close to free electron velocity or below [141, 142]. Vice versa, when assuming free-electron-like propagation, the observed delay amounts to an electron traveling a distance of (2.6 ± 0.6) Å in the screened volume. Efficient streaking of electrons starts at the Jellium edge, which is located half of the effective lattice spacing in the surface normal direction above the uppermost layer of atoms [19]. Relevant dimensions of W(110) are inscribed in figure 7.1. Hence, the average electron stems from between the first and second atom layer of the surface, revealing a significantly raised coupling of the top layer over the bulk to the vacuum continuum. For the literature IMFPs, a minimum of $\sim 71\%$ of all electrons must stem from the top crystal layer to explain the observed delay.

As cross-check, Peter Feulner provided high-resolution synchrotron photoemission spectra of the W(110) surface valence emission recorded at photon energies between 87 eV and 130 eV, two of which are displayed in figure 7.7. Compared to core levels, which show two distinct photoemission peaks from the surface and bulk layers, the low spacing and broadening of valence features aggravate the assignment of valence electrons. Nonetheless, surface states can still be recognized by an excitation energy independent binding energy because their excitation energy is not required to match a final band. In the spectra, three constant surface states were identified, which appear slightly shifted when compared to a literature reference recorded at 60 eV photon energy [143]. In the spectra recorded at 93 eV and 110 eV photon energy, most close to that used in the timing experiment (105 eV), the surface state electron yield accounts for a large part of the

spectral intensity in the conduction band energy region. This pronounced surface state emission supports the above interpretation of the absolute conduction band timing, even though the surface state effect could be weakened by the higher electron detection angle in the timing experiment. The absolute delay therefore reveals that tuning the photon energy allows to effectively select to emit surface electrons and create electron wave packets from crystals close to as fast as from isolated atoms.

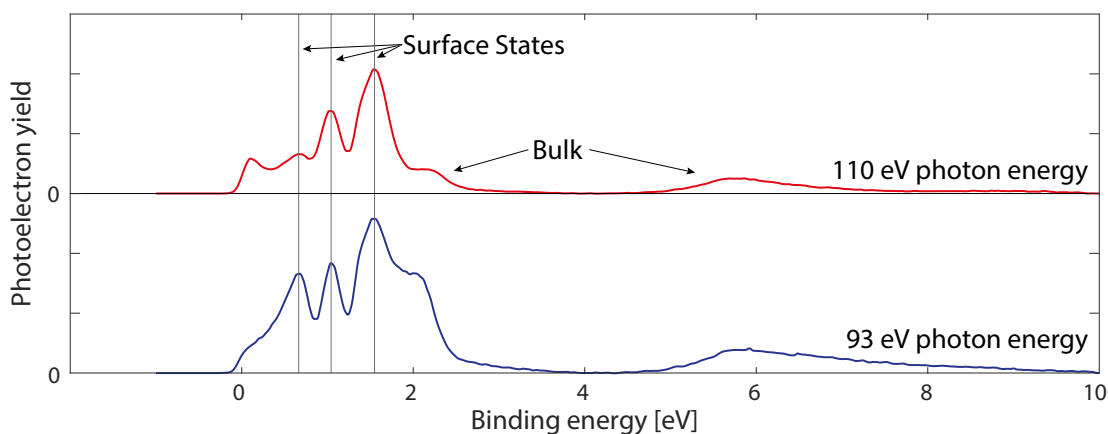


Figure 7.7: High-resolution conduction band synchrotron spectra at 93 eV and 105 eV photon energy. Clearly assignable surface and bulk states are indicated. Courtesy of Peter Feulner.

7.4 Adsorbate State Photoemission Delays

Another unique opportunity of this experiment is to investigate the photoemission dynamics of surface-adsorbate states. Atomic adsorbates correspond to the smallest usable building blocks for future solid-state devices. Furthermore, their timing can pose as a probe for the effective potential close to a surface, which is relevant for a multitude of technologically relevant processes such as heterogeneous catalysis or the properties of organic solar cells.

To scrutinize the role of adsorbate emission, we compare the valence electron spectra of a clean and iodine covered surface in figure 7.8 (b). The high kinetic energy side of the valence feature can be assigned to tungsten while the low kinetic energy electrons stem mainly from adsorbate states. We hence used the generalized-projections algorithm and referenced to [I]4d to retrieve energy-resolved photoemission delays. To increase statistics, figure 7.8 groups measurements at low, medium and full coverage.

The tungsten core level photoemission delay from the restricted TDSE retrieval is reproduced and shows no significant group delay dispersion or coverage dependence, confirming the validity of the retrieval. As expected, the high kinetic energy tungsten conduction band region also does not exhibit coverage dependence. The low kinetic

energy valence emission region, where adsorbate emission is occurring, possesses a strongly coverage dependent emission delay. At low iodine concentration, the emission is still dominated by tungsten electrons and thus comparable to the high kinetic energy region, which is dominated by tungsten conduction band electrons at all coverages. Contrary, the emission delay in the adsorbate region decreases considerably with increasing coverage, matching the behavior expected from a shift of the photoelectron origin to above the crystal surface. The picture suggests a freely adjustable photoemission delay when varying the iodine adsorbate density. While this is valid for the average photoemission delay of all electrons, achieving the same in single electron emission, i.e., in a wave packet picture, requires coherent emission of adsorbate and tungsten electrons. Due to the small maximum emission delay difference, this is hard to verify in the current experiment because the expected interference pattern peak spacing exceeds the excitation bandwidth.

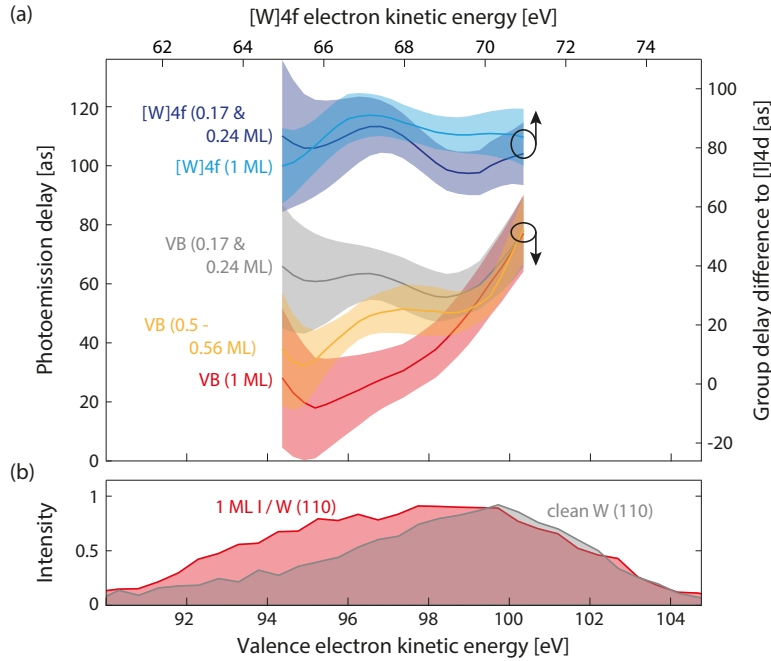


Figure 7.8: Isolation of the adsorbate photoemission delay. Panel (a): energy and adsorbate coverage resolved photoemission delay of valence and core level photoemission from I/W(110) (lines). Shaded areas mark 95% confidence. The half-covered [W]4f delay is omitted for clarity. Panel (b): valence electron spectra of a bare W(110) (grey shaded area) and an iodine covered I/W(110) (red shaded area) surface. Initial publication in [130].

The lowest point of the valence electron delay, 18 as, can be used as an upper limit for the pure adsorbate emission delay. Accounting for the remaining tungsten contribution, we find a pure adsorbate emission delay $\tau_{\text{IV}} = (8 \pm 19)$ as, in agreement with that retrieved from the restricted TDSE extrapolation. Adsorbates therefore seem to enable virtually

instant photon-photoelectron interconversion, which has before only been observed for independent atoms.

The helium time reference can be transferred from the gas phase onto crystal surfaces using a gauged intermediate chronoscope species. Dilute dielectric chronoscope atoms only weakly influence the crystal core electron exit timing. The remaining influence can be corrected using a coverage dependent study and extrapolation to negligible chronoscope surface coverage. A subsequent experiment on a bare crystal surface allows determining the absolute conduction band exit timing. For W(110), we find that [W]4f timing is explained by transport from inside the crystal to the surface and inelastic scattering limits the maximum emission depth. Contrary, conduction band electron exit is dominated by its spatial origin due to strong photoemission from surface states, which cause an unexpectedly low photoemission delay. The emission delay can furthermore be decreased when examining photoemission from valence states in atomic iodine adsorbates. From these, free electrons can be created in less than 18 as.

Chapter 8

Strongly Correlated Materials — The Opportunities of Photoelectron Timing

A field of major research interest is strongly correlated materials, in which the interaction between electrons has a defining influence on properties and even invokes new behavior, such as charge density waves, metal to insulator transitions and high-temperature superconduction [144]. Photoelectron timing and its understanding have advanced to a level that allows to determine delays with sub-attosecond uncertainties and separate their contributions. We found a significant influence of correlation on the photoelectron escape from simple systems. Therefore, attosecond streaking spectroscopy should as well be sensitive to correlation in these complex specimen, opening a new point of view to understand this still oracular class of materials.

As proof-of-principle, we conducted an attosecond streaking study on bismuth-strontium-calcium-copper-oxide (BiSCCO or BSCCO) high-temperature superconductors. Single crystalline BiSCCO-2212 was provided by Dr. Robert A. Kaindl, from which pristine surfaces were prepared in-situ by cleaving. Optimally oxygen doped BiSCCO can enter a superconducting phase below ~ 90 K. The doping can be reduced to decrease the critical temperature or entirely preclude superconduction [145, 146]. Such samples, referred to as *underdoped* in the following, do enter the *pseudogap* phase when cooled, which — as the superconducting phase — has its Fermi-level in a band-gap, however does not possess superconducting properties. At room temperature, all specimens behave like strange metals, but the strange-metal-pseudogap transition in underdoped BiSCCO happens gradually with decreasing temperature [147]. To scrutinize the influence of different phases on the photoemission timing, electron emission from superconducting and underdoped samples was timed at room temperature as well as at ~ 20 K, where the optimally doped crystals are in the superconducting phase. Measurements were performed using the FP2 laser system and AS3 surface beamline (see appendices B.1 and B.6). The sample temperature was estimated using a PT100 resistor placed as close as possible to the crystals using silver enriched epoxy resin. At 112 eV XUV photon energy, the samples show two separated features, valence band electrons and bismuth core electrons from the 5d orbitals ([Bi]5d). Because the photoelectron distribution was found to possess high angular dependence, the acceptance angle of the TOF detector was limited to $\pm 2^\circ$.

A streaking spectrogram of a sample in the superconducting phase can be found in figure 8.1. Electron emission from [Bi]5d precedes valence band electron emission in all

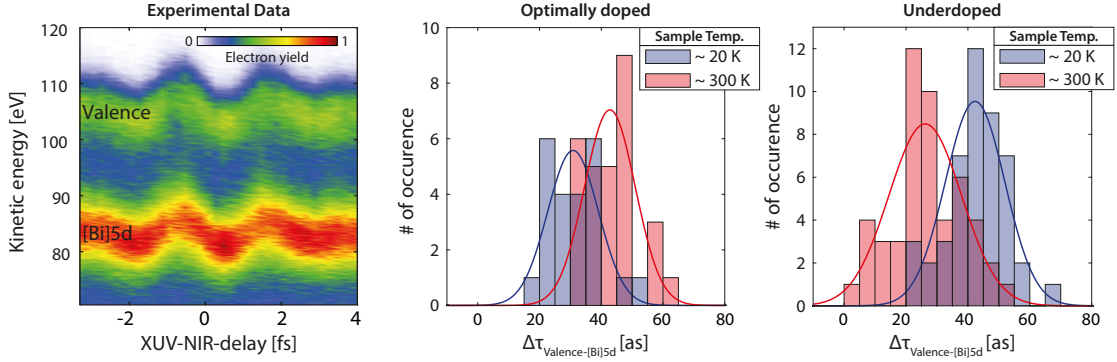


Figure 8.1: Photoemission timing of superconducting and underdoped BiSCCO at 112 eV XUV photon energy. Left panel: streaking spectrogram of BiSCCO in the superconducting phase. Middle panel: photoelectron timing of optimally doped BiSCCO in the superconducting phase and at room temperature. Right panel: electron timing of underdoped BiSCCO at ~ 20 K and room temperature.

cases by ~ 35 as, which is consistent with the layer order in a cleaved BiSCCO crystal. The cleaved crystal separates between two bismuth oxide layers such that [Bi]5d electrons stem exclusively from the surface layer while valence band electrons can also originate from deeper layers. A direct comparison of the photoemission delays of the respective specimen reveals significant phase impact. The doping and phase-resolved valence band to [Bi]5d delay measurements are shown in figure 8.1 and are summarized in table 8.1.

The valence band to [Bi]5d photoemission delay of optimally doped BiSCCO decreases by (12 ± 5) as when the samples are cooled below the critical temperature. Interestingly, underdoped samples in the pseudogap phase show opposite behavior than in the superconducting phase, their emission delay increases by (16 ± 6) as compared to the room temperature measurement.

sample type	$\Delta\tau_{\text{Valence-[Bi]5d}, 300 \text{ K}}$ [as]	$\Delta\tau_{\text{Valence-[Bi]5d}, 20 \text{ K}}$ [as]
optimally doped	43 ± 3	31 ± 3
underdoped	26 ± 4	42 ± 4

Table 8.1: Doping and phase-resolved BiSCCO photoemission delay averages. Errors represent 95% confidence.

Although it is questionable if the Cooper-pair binding is robust enough to directly influence the photoemission delay, the superconducting phase is accompanied by a multitude of property modifications, e.g., electron relocalization and charge-density waves [146], gap-opening and screening [148] and structural changes, which can influence the emission delay. Opposing changes in the reflectivity after NIR excitation of the pseudogap and superconducting phase were reported [148], but their magnitude seems

small compared to the observed delay change.

This peculiar behavior proves that attosecond streaking spectroscopy is sensitive to the phases of strongly correlated materials and that the variety of competing effects in strongly correlated materials require extensive experiments and sound theoretical support. The time resolution and sensitivity of streaking spectroscopy, combined with the number of available materials open a virtually infinite playing field for physicists to isolate and scrutinize the attosecond dynamics of the diverse phases in this rich class of new materials.

Chapter 9

Summary

This thesis introduces the absolute time axis to photoemission timing. The first time domain recording of direct and correlated photoelectron exit from a helium atom is presented. By refining and reformatting the experimental and evaluation tools, uncertainties below one attosecond were achieved in this measurement. Sub-attosecond agreement of the experimental timings with ab-initio modeling verifies the predicted absolute delays and establishes direct helium photoemission as gauged time-zero marker for attosecond spectroscopy.

The absolute scale allows scrutinizing what defines the phase of a photoelectron. We find that the direct photoemission delay is correctly captured by the phase accumulated during the emission process and a coupling of the ionic Coulomb potential with the streaking laser field.

The shake-up photoemission delay from helium allows understanding how the interaction of electrons modifies the photoemission process on an attosecond scale. We observe a correlation delay that additionally slows down photoelectrons when they participate in the correlated shake-up process. Electron repulsion during the photoelectron exit prepares the parent ion in a state that possesses a slowly oscillating and oriented electric dipole moment. Due to the rapidity of the emission process enforced by the attosecond XUV pulse, this dipole couples to the streaking field via the dc-Stark effect and back-action to the photoelectron causes the correlation delay. This delay is then exploited to determine not only the phase of the photoelectron wave packet but also the dipole's oscillation phase and therefore enables the complete reconstruction of the prepared ionic quantum state. The magnitude and occurrence of the correlation delay in the ground state photoemission of atoms are limited, though in systems that possess permanent electric dipole moments, i.e., oriented molecules, dipole delays can be very apparent.

To prove the universality of the new reference after being applied to atoms, the work introduces ways to apply it to molecules and condensed matter.

In a mixed-species gas-phase measurement the helium clock was used to absolutely time electron escape through the iodine giant dipole resonance. The experiment reveals that the resonance significantly slows down electron exit and that its delay outweighs that of a pure hydrogenic system eightfold. This delay increase suggests a resonance origin that can be assigned a lifetime. In the time domain, the giant dipole resonance behavior resembles an autoionizing resonance, even though no explicit intermediate state is involved. The delay found from the experiment and scattering calculations however exceeds that predicted by the Fano formalism, hinting at a complicated resonance structure. Scattering

calculations furthermore show that the angle-resolved photoemission delay is sensitive to molecular structure and potentials.

The results of the helium and iodine measurements were then combined with the results of two measurement campaigns on tungsten surfaces. Gauged atomic iodine clocks placed on top of a tungsten surface were used as an absolute marker to determine the photon arrival time at the surface. The absolute tungsten [W]4f core level electron exit timing proves that the transport of core photoelectrons at the examined energy is governed by free-electron-like dispersion inside the crystal. Their delay is defined by their average emission depth which is limited by inelastic scattering.

The absolute timing of conduction band electrons was determined by referencing relative measurements on a clean tungsten surface to the absolute [W]4f timing. Contrary to core level emission, we find that conduction band electrons exit the crystal significantly faster than expected from inelastic scattering and free-electron-like transport. Because band structure calculations exclude considerably increased group velocities, the speed-up can be attributed to the spatial origin of the photoelectrons. High-resolution synchrotron conduction band photoelectron spectra contain prominent surface states, supporting this theory. We hence find that two different regimes define how vacuum electron wave packets are created from core orbitals and the conduction band in tungsten: transport and scattering dominated electron exit and origin dominated exit.

By examining the coverage dependent and energy-resolved valence electron emission delay, the photoemission timing of I/W(110) surface-adsorbate states was measured. We find a miniscule electron emission delay for iodine valence states. It is as small as from isolated atoms, introducing a way to create free electrons from solid devices without latency. This fact can be used to achieve more simplified absolute timing schemes for solids in the future.

Introducing the absolute zero to photoemission timing allows to experimentally assign an unambiguous photoemission delay to the orbitals and processes observed in a photoemission spectrum. These can straightforwardly be decomposed into constituents. The experiments presented in this work pioneer the application of the helium reference and identified and isolated photoemission delay contributions caused by the short-ranged photoelectron potential, the interaction of the long-range Coulomb potential and the streaking laser, the correlation of electrons, resonances, transport and the point of origin of photoelectrons.

Chapter 10

Outlook

It is evident that, just as the human understanding expects, every physical interaction is accompanied by a delay. Even though magnitudes in the attosecond realm led to their neglect in the past, photoemission delays are well defined, and the proper tools allow their quantification. The photoemission delay contains as much information as the photoabsorption cross-section, an observable that has shaped our understanding of quantum physics. Especially the complementary use of these quantities grants deep insight into the mechanisms and potential that precede the chemical answer to photoionization.

Photoemission delay measurements are evolving from proof of principle experiments to measurement tools, and their theoretical framework grows more sophisticated and standardized, promoting their application to material science. At the same time, the efficient and clean harvesting, storage, and transport of power crystallize as central questions for science. The search for new materials that outperform state-of-the-art devices in properties such as charge separation after photoabsorption, energy storage, conductivity or chemical reaction efficiency is in full swing. As a method that completes conventional techniques such as angle-resolved photoemission spectroscopy by unraveling the complex part of the photoelectron wave function, photoemission timing provides a rapidly progressing perspective to understand what defines the initial answer of matter to light.

We are only starting to exploit its possibilities, most of which will probably only be recognized in future research. New applications already became apparent during the research for this thesis:

- Simulations show that angle-resolved delay measurements on oriented molecules or adsorbates can sense the angle-resolved photoelectron potential energy surface, which is responsible for many chemical reactions such as catalysis or charge separation in organic solar cells. Developing photoelectron timing as a tool that can commonly retrieve these potentials can be used to systematically identify the governing factors and might in the future help to design molecules that reach or even surpass nature's counterpart.
- Semiconductor structures are quickly approaching atomic dimensions. Attosecond delay measurements allow following the creation and transport of electrons with attosecond time and Ångstrom-level spatial resolution. We therefore already have a tool to examine the ultimate size limits for technology, which can be applied to

explore the high-lying conduction bands in semiconductor materials and atomic scale devices.

- Highly-correlated materials can offer vastly superior properties due to new phases defined by electron-electron interaction. We found that the photoemission timing is a sensible probe for these phases and their properties. In-depth examination, especially with found theoretical support can thus reveal valuable information about the evading fundamentals of these new states of matter.

Appendix A

Photoemission Delay Retrieval

Three types of retrievals were used in the research supporting this thesis, center-of-energy (COE), restricted TDSE and generalized-projections retrieval. These will be discussed in this chapter along with the necessary pre-processing steps energy calibration, electrostatic lens correction, background subtraction and the correction of systematic errors due to attosecond pulse chirp.

A.1 Center-of-Energy Retrieval

A method to retrieve the NIR probe laser field from a spectrogram is to reduce its dimensionality by considering the COE, i.e., the first-moment, of the electron kinetic energy distribution $I(E_{\text{kin}}, \Delta t)$ for each individual XUV-NIR delay Δt using equation (A.1).

$$E_{\text{COE}}(\Delta t) = \frac{\int_0^\infty I(E_{\text{kin}}, \Delta t) p \, dp}{\int_0^\infty I(E_{\text{kin}}, \Delta t) \, dp} \quad (\text{A.1})$$

In the limit of a much shorter XUV pulse duration \mathcal{T}_{xuv} than streaking laser oscillation period, $\mathcal{T}_{\text{xuv}} \ll \frac{2\pi}{4\omega_{\text{laser}}}$, this directly yields the probe vector potential, see equation (4.4). For longer attosecond pump pulses, the recorded COE amplitude deviates significantly from the amplitude expected from the streaking electric field strength, since the pump pulse averages over a significant part of the probe beam. For very long XUV pulses, the recorded signal is distorted and eventually lost. Figure A.1 displays three examples for different XUV pulse durations. The recognizable streaking picture disappears for increasing XUV pulse lengths but the shape of the NIR field is still extractable, even when the XUV pulse duration is comparable to the streaking laser oscillation period, $\mathcal{T}_{\text{xuv}} \approx \frac{\pi}{\omega_{\text{laser}}}$. The amplitude dependence of the recorded energy shift is universal when considering the attosecond pulse duration divided by the streaking laser oscillation period, $\mathcal{T}_{\text{xuv}}/T_{\text{laser}}$, which can be used to calculate the real field strength in the experiment if the XUV pulse duration is known. Multiple photoemission lines in a spectrogram can be examined by cutting the spectrogram into energy regions each containing a single feature. This is aggravated if the streaking amplitude is high and these energy regions overlap, which can in part be overcome by modeling the overall spectrum, for example by least-squares fitting multiple Gaussians to the individual delay slices of the spectrogram.

By comparing the relative delay shift of the first-moments of different photoemission features, relative photoemission delays can be extracted, a technique used in early works,

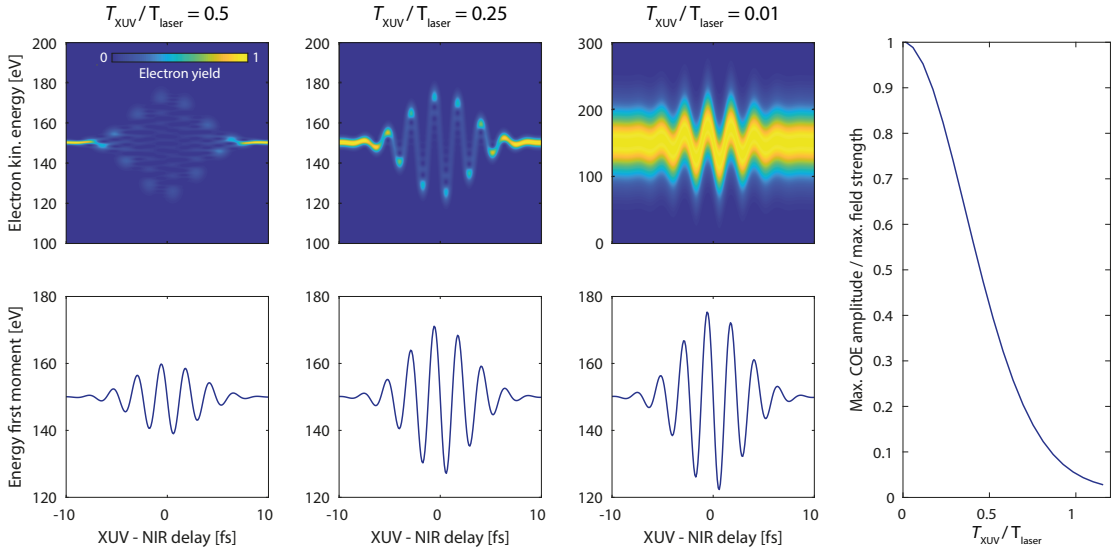


Figure A.1: Scaling of the energy first-moments with the XUV pulse duration. Upper Panels: simulated streaking spectrograms using compressed XUV pulses with different durations (energy bandwidths) and the same streaking laser field. A sideband-pronounced structure changes to an isolated shift when decreasing the XUV pulse duration. Lower Panels: the shape of the energy first-moments resembles the vector potential of the streaking field, but the amplitude decreases significantly for long XUV pulses. Right panel: the decrease in the center-of-energy (COE) streaking amplitude is universal against the quotient of the XUV pulse duration and the streaking laser oscillation period $\mathcal{T}_{\text{xuv}}/\mathcal{T}_{\text{laser}}$. The plotted curve can be used to retrieve the actual streaking field strength if the XUV length is known.

e.g. [6]. The shift can be extracted by either fitting an analytic pulse shape with an individual delay to each photoemission feature's first-moments or directly evaluating the group delay via Fourier transform. However, the decrease in dimensionality leads to a loss of information. Thus, parameters also crucial to the proper post-processing of photoemission delays, such as the XUV group delay dispersion cannot be extracted from the first-moments. Therefore, the XUV pulse duration cannot be retrieved. In principle, bootstrapping classical retrievals such as the COE method for the group delay and a bandwidth evaluation such as in [56] for the group delay dispersion is possible. Nonetheless, those methods fail for long XUV pulses and are not much simpler than the methods treated below.

A.2 Restricted Time-Dependent Schrödinger Equation Retrieval

To characterize both, the XUV pulse and streaking field, the straightforward way is to resort to a quantum description of streaking, i.e., equation (4.11). If it is possible to reasonably approximate the involved pulse shapes using analytical equations, the number of free parameters decreases to a number that permits using a conventional least-squares minimization to extract the main pulse parameters [7]. In principle, equation (4.11) can directly be used, but the integration is numerically expensive. Therefore, we apply the central momentum approximation, which allows evaluating the integral as a much cheaper fast-Fourier-transform. The used form, as well as limitations, are given in appendix A.3. In our case, a Gaussian pulse shape and a parabolic phase for both the XUV and NIR pulse, parametrized as in appendix A.4, resembled the actual pulse shapes well. Each electron wave packet and the streaking field is hence described by an amplitude, central frequency, bandwidth, group delay and group delay dispersion. Additionally, the streaking field needs a CEP for its correct description. Wave packets were parametrized in the spectral domain to avoid unphysical coupling of the electron pulses' group delay dispersions to their bandwidth, the necessary equations are also presented in section A.4. The photoemission delay and delay dispersion of the first peak are entangled with the XUV pulse parameters, each additional peak adds an additional amplitude, relative delay and group delay dispersion. Depending on the number of peaks and additional degrees of freedom, this results in 12 or more not necessarily orthogonal parameters. Thus, the speed and reliability of the method are significantly boosted by robust starting guesses. The COE method provides reliable start values for the streaking field parameters, the amplitude, and bandwidth of the electron wave packets can be evaluated from an unstreaked spectrum, allowing decreasing the free parameters without proper start value to three largely independent ones per photoemission feature. The main strengths of the technique are the retrieval of the electron wave packet and the possibility to fix known parameters to introduce additional stability, such as the photoemission cross-sections, which are often available from synchrotron measurements. Hence, we address it as *restricted TDSE retrieval*. No reliable expansion could be achieved to individually determine the photoemission delay of features with strong spectral overlap. However, the restricted TDSE retrieval allows fixing the delay of such features, which allows extracting a well-defined delay for the composite feature. This composite delay is dominated by the largest of the overlapping features. Figures A.2 and A.3 examine the formation of such a composite delay for two overlapping photoemission lines of which the major photoemission peak has zero delay, and the minor side peak's delay is varied. Both, a fit to the first-moments of the composite feature and the restricted TDSE retrieval are linear in all features' delays, as can be seen from the invariance of the fractional delay in figure A.2, panels (c) and (d). The weight of the peaks to the composite delay differs significantly between the methods. The COE method weights all contributions to the composite delay strictly linear in their intensities, independent of the peak spacing and XUV bandwidth, for example see figure A.2, panel (b). Therefore, minor side peak contributions can have a significant influence on the COE composite delay. Such a

linear weighting only applies to the restricted TDSE retrieval in the limit of perfectly overlapping peaks, i.e., zero energy spacing between the peaks or a much larger spectral bandwidth of the XUV pulse (figure A.3 (d), right edge). For peak distances on the order of the XUV bandwidth, e.g., a few eV (see figure A.2 (a)), the restricted TDSE method weights delay contributions quadratically with their intensity. This weighting causes high suppression of small side peaks. Nonetheless, the composite delay stays linearly dependent on the mixed delays (figure A.3 (c)). As shown in figure A.3 (d), the maximum effect of small contributions in this bandwidth regime is found if the XUV bandwidth is equal to the peak spacing, which is the case considered in figure A.2. Figure A.2 thus displays a worst-case scenario. Nonetheless, up to 33% minor side peak contribution, which corresponds to a minor/major peak ratio of 1/2, the weight of the side peak to the composite delay is less than 7%. Thus, the restricted TDSE method can reliably retrieve photoemission delays, even if small interfering peaks with up to half of the major feature's intensity are present.

A.3 Generalized-Projections Retrieval

Generalized-projections based retrievals are outstanding for the extraction of arbitrary streaking and electron pulses from a spectrogram. The technique has a solid record in the field of ultrafast optics because it is routinely used for the evaluation of FROG-traces [149]. However, the algorithm type can generally be applied to reconstruction problems, as long as the measured signal can be reorganized to the form (A.2). The two involved light fields are referred to as pulse (also probe) $P(t)$ and gate $G(t)$.

$$S_{\text{GP}}(\omega, \Delta t) \propto \left| \int_{-\infty}^{\infty} dt P(t + \Delta t) G(t) \exp(i\omega t) \right| \quad (\text{A.2})$$

The quantum mechanical description of streaking in the strong-field approximation, equation (4.11), is close to that form [150, 151]. There are multiple choices to approximate equation (4.11) such that the requirements of equation (A.2) are fulfilled. In our implementation, we followed [58], which assigns the complex time domain electron wave packet envelope $\tilde{\chi}(t + \Delta t)$ to pulse and the Volkov-phase exponential to gate [58]. This choice explicitly acknowledges that the transition matrix element causes a difference between the XUV pulse's time structure and the electron wave packet. To avoid momentum dependence in the gate, the central momentum approximation $e^{i\phi_V(p,t)} \approx e^{i\phi_V(p_0,t)}$ is applied, which replaces the momentum in the Volkov-phase with the center of the unstreaked momentum distribution p_0 . In the case of streaking, this is a good approximation as long as the streaking amplitude is not comparable to the unstreaked electrons' kinetic energy. The final expression is

$$S_{\text{GP}}(E_{\text{kin}}, \Delta t) \propto \left| \int_{-\infty}^{\infty} dt \tilde{\chi}(t + \Delta t) e^{i\phi_V(\sqrt{2E_{\text{kin}}}, 0, t)} e^{it(E_{\text{kin}} - \omega_{\text{xuv}} + IP)} \right|^2. \quad (\text{A.3})$$

From the retrieved Volkov phase, the streaking electric field can be calculated. No assumptions apart from the interaction mechanism are necessary. Therefore, arbitrary

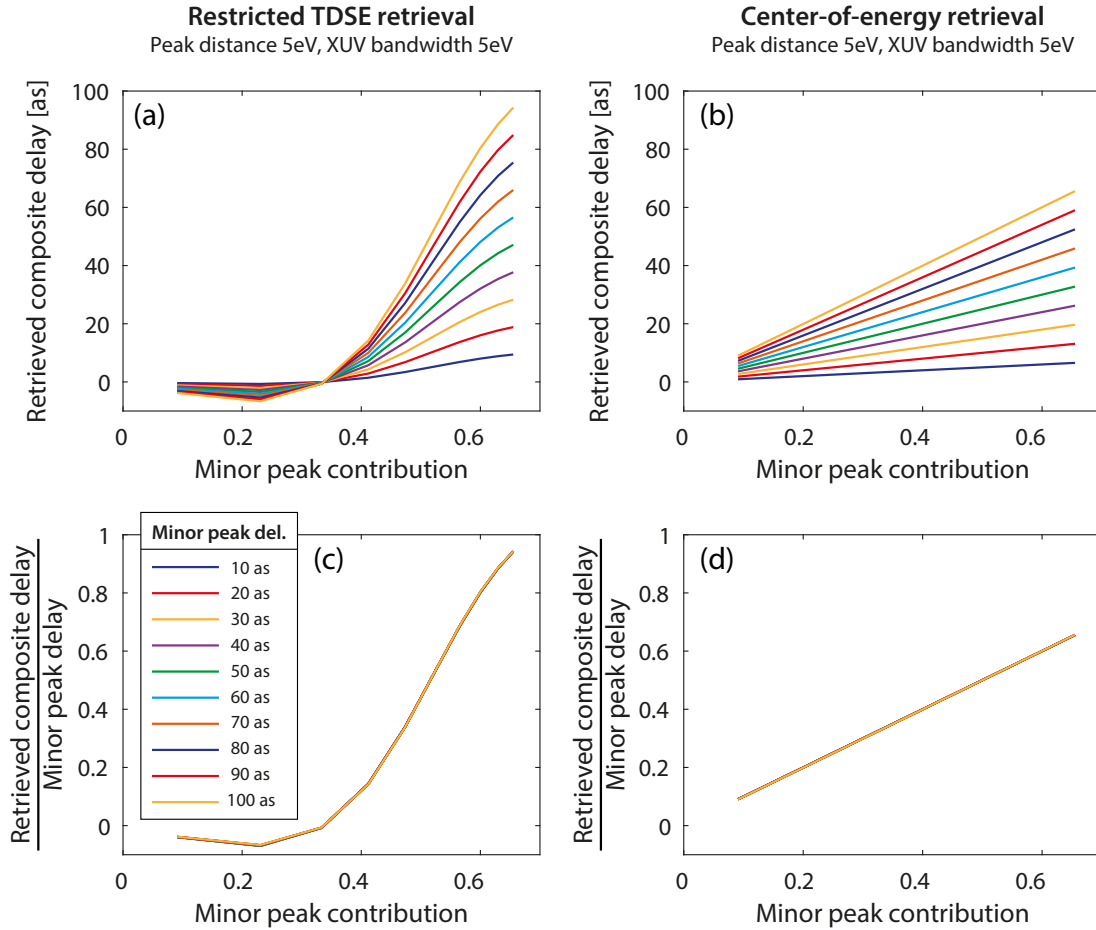


Figure A.2: Retrieved composite delay for simulated overlapping photoemission peaks. The major peak has zero delay, the minor side peak delay and intensity is varied. Panels (a) and (c): results of the restricted TDSE method. The influence of the minor side peak on the composite delay is linear in its delay but quadratic in its contribution to the composite feature. Panels (b) and (d): results of the COE retrieval. The side peak influence is linear in both, its delay and its contribution.

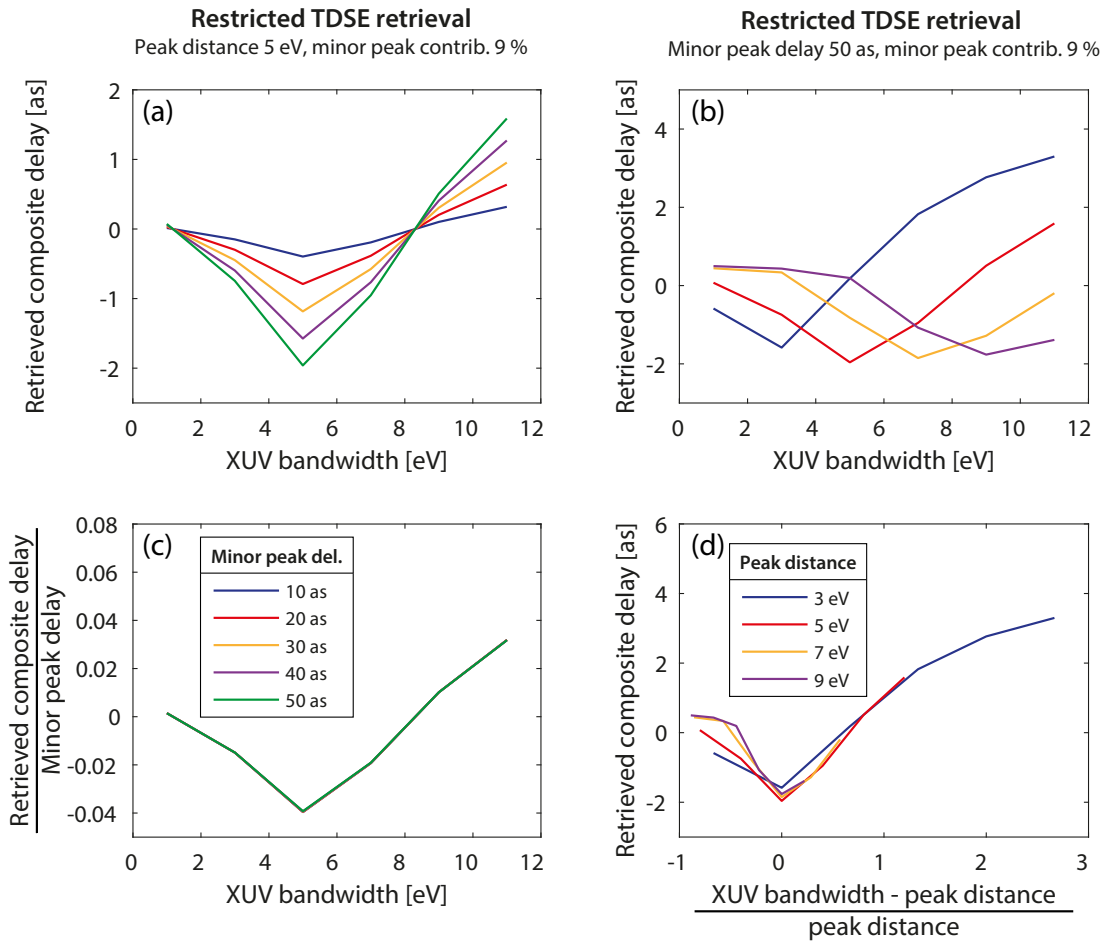


Figure A.3: Retrieved composite delay for simulated overlapping photoemission peaks. Only results for the restricted TDSE method are displayed because the examined parameters do not influence the COE retrieval. Panels (a) and (c): the minor side peak delay and the XUV bandwidth is varied. The side peak contribution is linear in its delay. Panels (b) and (d): the peak energy distance and the XUV bandwidth is varied. Two regimes are found: for large XUV bandwidth or small peak spacing, the peaks become indistinguishable, and the weighting becomes linear. For comparable XUV bandwidth and peak spacing, contributions to the composite delay are weighted quadratically. The biggest influence is found if the XUV bandwidth is equal to the energy spacing between the peaks.

electric fields and electron wave packets are retrievable, allowing application of the technique to complicated waveforms. The algorithm achieves the fitting of many hundred degrees of freedom by projecting between two sets of waveforms, defined by different constraints. The solution is found at the intersection of these sets. Starting from a random guess, a spectrogram (signal) is calculated and then projected onto the measured data constraint by replacing the spectral amplitudes of the calculated signal by the measured amplitudes. Subsequently, the signal is Fourier-transformed to the time domain and the second constraint which demands that the signal can theoretically be generated from the probe and gate via the specified mechanism is enforced. This step is more complicated and is achieved by varying the electric field and electron wave packet such that the distance between the transformed signal and a signal simulated from the currently guessed field and wave packet is minimized [149]. With the new field and wave packet calculated, the process is repeated until convergence is reached. Convergence is not guaranteed mathematically because the two sets of waveforms are not convex. Practically the algorithm finds reasonable solutions in close to all cases.

Generalized-projections algorithms are distinguished by their fast convergence and the possibility to retrieve the full spectral phase of the involved pulses. With the large freedom, allowing to fully model the involved pulses, comes the drawback that inter-peak photoemission delays are not retrievable from experimental data to the same level of precision as with the restricted TDSE scheme. Intra-peak photoemission delays, e.g., the group delay dispersions introduced by the energy dependence of the transition matrix elements, are correctly captured by the algorithm [58].

Implementations of generalized-projections to attosecond streaking are available [151] but focus on the retrieval of the laser and attosecond pulse from streaking an isolated photoemission peak. In the course of this thesis' research, a new implementation of such an algorithm, focused on the treatment of photoemission delays, was programmed and commissioned.

Its overall construction follows [151], as well as the minimization step, which was implemented via a least-squares optimization. To treat photoemission delays, the algorithm simultaneously runs on two partial spectrograms, created by cutting the full spectrogram into sections containing only a single photoemission feature. The partial spectrograms remain coupled by averaging the streaking laser fields between reconstruction steps, which prevents arbitrary photoemission delays due to a relative streaking field walk-off. One could retrieve the photoemission delay also from fitting a full spectrogram, which would result in a heavily modulated retrieved temporal shape due to interference of the different photoemission features, which the algorithm assumes to be coherent. Though, if fitting a full spectrogram, the central momentum approximation is often inappropriate and deteriorates results. The algorithm was tested on ab-initio simulations of helium photoemission. Thus, neither the strong-field nor the central-momentum approximation, which are employed for the retrieval, were used in the simulation. Test data was kindly provided by Renate Pazourek [74]. The resulting spectrograms include only two well-separated features, called shake-up ($n = 2$) and shake-down ($n = 1$) with different photoemission delay and group delay dispersions. The processes and simulations are described in detail in

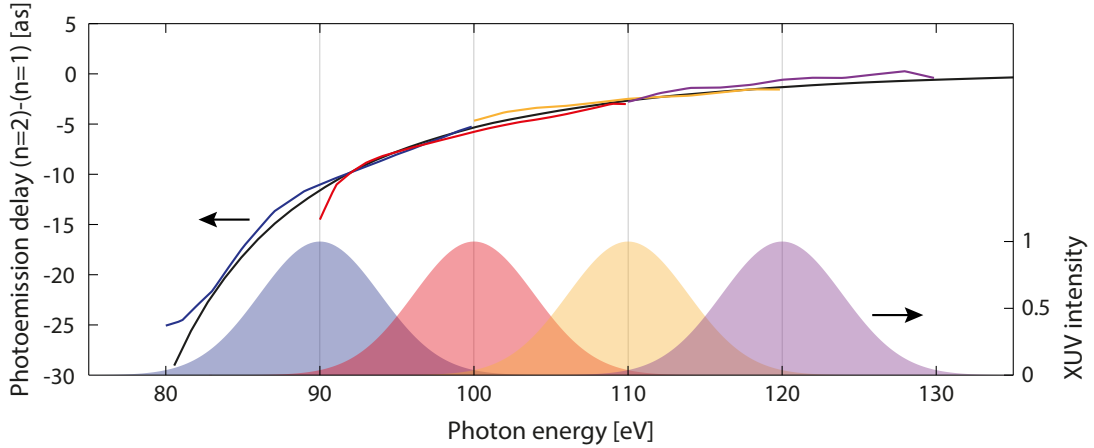


Figure A.4: Generalized-projections test on ab-initio modeling of helium photoemission, only direct and shake-up emission into $n = 2$ are included. Upper part: analytic prediction of the relative photoemission delay (black line) and results of a generalized-projections-retrieval of the ab-initio data (colored lines). Lower part: the XUV pulse spectra employed for calculating the four test spectrograms (shaded areas).

chapter 5. Analytic predictions for the photoemission delay exist as a benchmark, which are validated by the COE and restricted TDSE retrieval methods, so the spectrograms offer a reliable and expedient test case. Figure A.4 shows the retrieval results for four simulated spectrograms recorded using XUV pulses centered at 90, 100, 110 and 120 eV and a bandwidth of 9.2 eV. While the COE method only returns the delay at the central photon energy (grey lines) and the restricted TDSE method returns the photoemission delay in the proximity of the central photon energy, the generalized-projections method returns the photoemission delay for most of the XUV pulse bandwidth. In the current example, in regions where the XUV pulses' spectral intensities were higher than 10% of the maximum, a maximum deviation of 1.8 as was found for this test case, even in the steep low energy region. The two main advantages of this algorithm are the extraction of data without previous assumptions and the availability of the photoemission delay for the whole XUV spectrum. In the current example, a generalized-projections retrieval of three spectrograms can provide the photoemission delay for the whole displayed spectral range, while other retrieval methods require many more simulations to cover the void between data points.

A.4 Chirped Gaussian Pulses in the Time and Frequency Domain

We use Gaussian pulses to model both the streaking laser field, as well as the electron wave packets in the restricted TDSE method because they approximate the experimental pulses well. Another advantage is their self-similarity under Fourier transformation.

Therefore, pulse description in both time and frequency domain is equivalent in cases dealing with a single light or electron pulse. However, when describing coupled pulses, the domain in which pulses are described in is not exchangeable and has to be picked depending on the coupling constraints between the pulses. The employed analytical expressions for a linearly chirped Gaussian pulse in the frequency and time domain are presented in equations (A.4)-(A.8).

When changing a pulse's chirp using a perfect optical element, the pulse's radiant fluence H_e is invariant. Consequently, the normalization in equations (A.4)-(A.8) is chosen to maintain the radiant fluence.

In the frequency domain, the electric field of a linearly chirped Gaussian laser pulse can be described using some measure of amplitude, in this case H_e , an intensity FWHM bandwidth $\Delta\omega$, its carrier frequency ω_0 , its linear group delay dispersion β_ω , its central frequency's position in time t_0 and the CEP ϕ_{CEP} .

$$\tilde{E}^+(\omega) = \sqrt{H_e}^4 \sqrt{\frac{16\pi\alpha^2 \ln 2}{\Delta\omega^2}} e^{-2 \ln 2 \left(\frac{\omega - \omega_0}{\Delta\omega}\right)^2} e^{i\left(\frac{1}{2}\beta_\omega(\omega - \omega_0)^2 + \omega t_0 + \phi_{\text{CEP}}\right)} \quad (\text{A.4})$$

In the time domain, instead of the bandwidth one rather uses its intensity FWHM duration \mathcal{T} and its linear chirp β_t . However, all these can be deduced from the spectral domain quantities using equations (A.6)-(A.8).

$$\tilde{E}^+(t) = \mathcal{F}^{-1}(\tilde{E}^+(\omega)) = \frac{1}{2} N_t e^{-2 \ln 2 \left(\frac{t - t_0}{\mathcal{T}}\right)^2} e^{i\left(-\frac{1}{2}\beta_t(t - t_0)^2 - \omega_0(t - t_0) + \phi_{\text{CEP}}\right)} \quad (\text{A.5})$$

$$\mathcal{T} = \sqrt{(\beta_\omega \Delta\omega)^2 + \left(\frac{4 \ln 2}{\Delta\omega}\right)^2} \quad (\text{A.6})$$

$$\beta_t = \frac{\beta_\omega \Delta\omega^4}{\beta_\omega^2 \Delta\omega^4 + 16(\ln 2)^2} \quad (\text{A.7})$$

$$N_t = \sqrt{H_e}^4 \sqrt{\frac{256\pi\Delta\omega^2\alpha^2 \ln 2}{\beta_\omega^2 \Delta\omega^4 + (\ln 16)^2}} \quad (\text{A.8})$$

Figure A.5 displays two sets of two coupled attosecond pulses. The left column's pulses are defined in the spectral domain using equal radiant fluence, equal bandwidth and a vanishing and non-vanishing group-delay dispersion. Per definition, the spectral intensities coincide. The time domain envelope of the uncompressed laser pulse is significantly elongated as one would expect for a chirped pulse. Contrarily, the right column's pulses are defined in the time domain using the same equal radiant fluence, but equal duration and vanishing and non-vanishing time domain chirps, equivalent to the left column's group delay dispersions. Now, per definition, the time-dependent intensity coincides, and

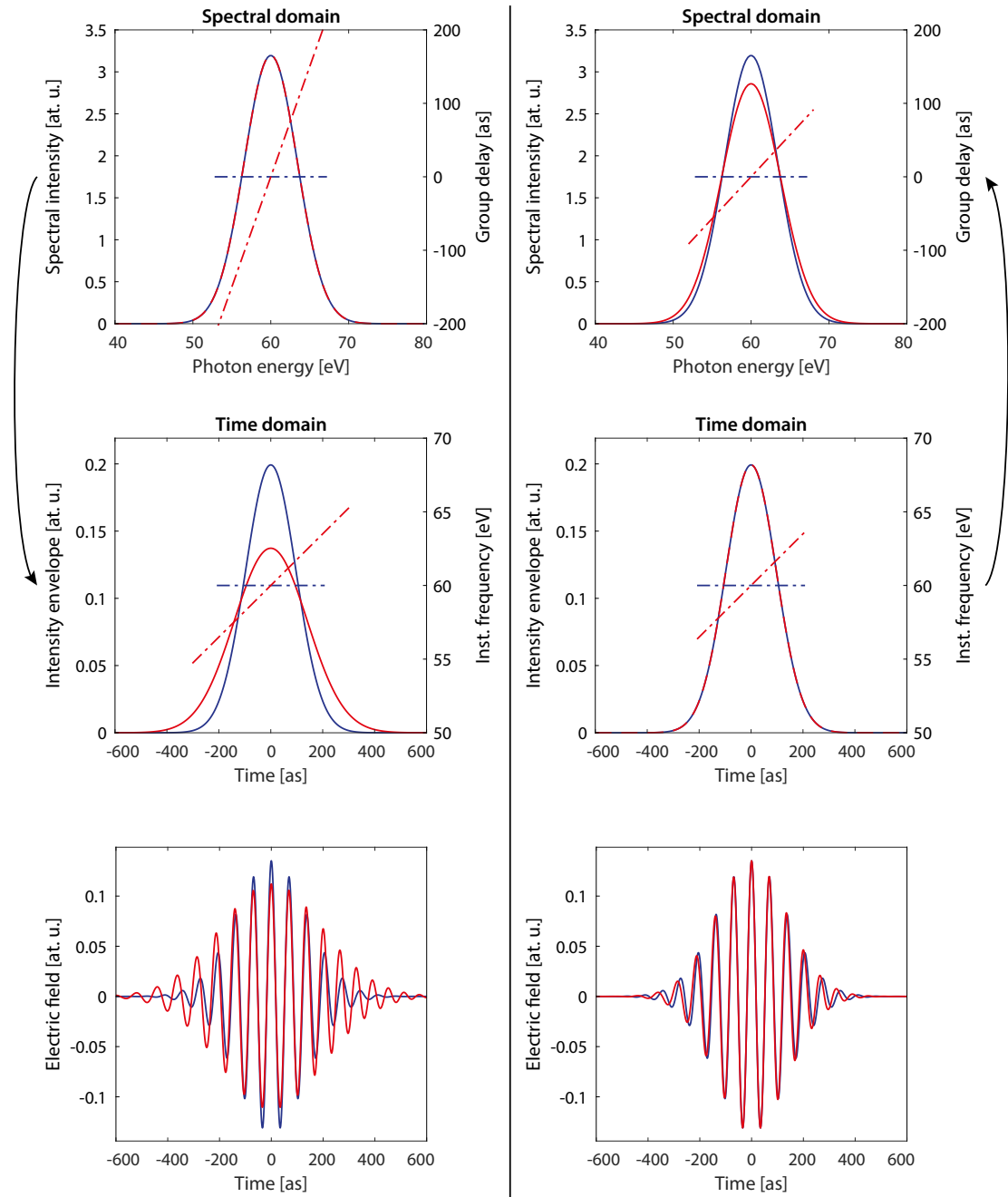


Figure A.5: Gaussian laser pulses in the time and frequency domain. Intensities, fields (full), group delays and instantaneous frequencies (dashed-dotted) are depicted. Left column: definition in the spectral domain with equal bandwidths and different group delay dispersions. Right column: definition in the temporal domain with equal durations and different chirps.

the spectral intensity of the chirped laser pulse is broadened compared to the unchirped one.

When considering fitting an attosecond streaking spectrogram containing multiple photoemission features, this difference between domains has important implications. Fitting happens under the assumption that the electron wave packets resemble the photoemitting attosecond pulse's relative spectral intensity multiplied by the energy-dependent photoemission cross-section. Varying the time of arrival and chirp of the different features in the spectrogram then allows retrieving the relative photoemission delay and chirp differences between electron wave packets. Constraining degrees of freedom in the fitting process can significantly increase stability, e.g., if only different photoemission delays are allowed, the duration or bandwidth of all electron wave packets created by the same attosecond pulse should be the same. However, if the photoemission delay and its frequency dependence of the electron wave packets are examined, only the bandwidth can be fixed across the features, not the duration. This can be directly deduced from figure A.5: Two pulses of equal duration but different chirp exhibit different spectral widths in the photoelectron spectrum, which is non-physical if the photoemission cross-section is properly accounted for (natural line widths are usually negligible compared to an attosecond pulse's bandwidth). Thus, defining our wave packets using one duration prohibits the reliable retrieval of attosecond electron wave packets exhibiting different chirps. If instead defining the wave packets in the spectral domain using one bandwidth and different group delay dispersions, no problem arises since the spectral width for all photoemission features is fixed by definition and the duration of all wave packets is varied according to their group delay dispersion.

It is convenient to use Gaussian laser pulses due to aforementioned properties. Nonetheless, using equations (A.4) or (A.5) allows generating pulses of any duration. The formulae do not guarantee physical pulses. According to the wave equation, only electric fields with vanishing time integral are allowed to propagate. This condition is violated when defining Gaussian envelope pulses with durations close to or shorter than their oscillation period. Therefore, if working in this regime, the time integral has to be addressed as a sanity check and if necessary other pulse shapes must be chosen.

A.5 Photoemission Cross-Section — Extreme-Ultraviolet Chirp Delay Distortion

If an attosecond streaking experiment is performed using chirped XUV light, caution has to be exercised if the examined photoemission feature's photoemission cross-section is energy-dependent over the bandwidth of the employed XUV light [98, 151]. Depending on the cross-section's slope, it shifts the observed photoelectron central energy from the expected value defined by the photon energy and the ionization potential in the experiment. The leading and trailing edges of a chirped attosecond pulse have different photon energy. This translates the cross-section energy shift to a shift in the effective light pulse time-of-arrival and thus an apparent delay because the leading and trailing light pulse edges have a different probability to ionize. Figure A.6 illustrates a worst-case

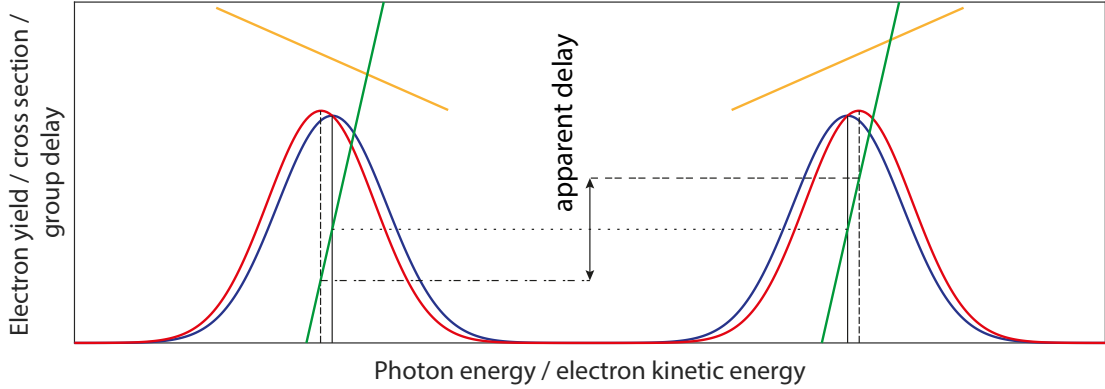


Figure A.6: Apparent delays due to cross-section-XUV-chirp-interaction. The real spectrum (blue) is distorted by the photon energy-dependent cross-section (yellow) such that the observed photoemission features (red) weight the XUV pulse’s spectral components differently. The energy-dependent XUV group delay (green) therefore causes a different effective time-of-arrival of the attosecond pulse for the two depicted spectral features. Even though the photoemission delay of both features is equal (horizontal dotted black line), the experiment measures an apparent delay (dashed-dotted lines). Initial publication in [73].

example. Two compared photoemission features display opposite cross-section energy dependence. Hence, the XUV chirp causes opposite delay changes, and the apparent delay is maximized.

Because photoemission cross-sections are often available from synchrotron measurements, the effect can be estimated and corrected using two approaches. Gagnon et al. [151] propose dividing all measured spectra by the relevant photoemission cross-section, which naturally eliminates the effect before data analysis and is superior for complex cross-section shapes, e.g., near autoionizing resonances. This approach however does not correctly work in the presence of background, requires stitching of cross-section data when multiple features are observed and estimating the magnitude of the correction requires a complete re-evaluation of all data. For measurements in energy regions with slowly varying photoionization cross-section, we hence calculate and correct the leading order effect in post-processing by determining the XUV group delay dispersion and multiplying by the peak shift for each evaluated feature.

A.6 Data Conversion and Energy Calibration

Before retrieval, all individual spectrograms were energy calibrated using time-to-energy conversion tables for the employed electrostatic lens setting, which alter the expected $E_{\text{kin}} \sim t^{-2}$ behavior. These were mostly available from the time-of-flight spectrometer vendor and otherwise measured using xenon $N_{4,5}O$ Auger emission and photoemission [152]. To preserve the electron yield integral and central peak positions, the energy-dependent

intensity was scaled by the Jacobian of the time-to-energy conversion. The time-to-energy conversion introduces nonlinear energy sampling which is undesirable, e.g., for the generalized-projections-type retrieval. Thus, the electron spectra were binned and scaled such that the electron yield was preserved. Furthermore, an energy-dependent amplification of a photoemission feature can cause a delay change in the presence of attosecond pulse chirp in a mechanism similar to that discussed in section A.5. Therefore, lens transmission tables were measured using background electron emission from graphite where no lens transmission tables were available.

A.7 Background Subtraction

Background electrons due to inelastic scattering form a continuous slowly changing pedestal below the highest kinetic energy photoemission feature. While inelastic scattering is most prevalent in high-density samples, i.e., solids, it also happens at decreased probability in gaseous samples. Although caused by the same process, the gas-phase and solid case are different due to the time when inelastic scattering occurs. The ratio of integrated atom density before and in the streaking volume to the integrated atom density after streaking until detection is large for a solid and small for a gaseous sample. Therefore, the majority of inelastically scattered electrons from a solid sample were scattered before streaking and hence streak with a randomly increased delay due to the statistical nature of scattering [19]. Comparing with figure A.1, the long duration of the resulting wave packet decreases the average streaking amplitude of background electrons. Inelastically scattered electrons from a gaseous sample predominantly scatter after streaking and when the streaking shift is already fully developed. Consequently, they do not lose their phase in the streaking spectrogram but change their energy. The edge of the background spectrum thus streaks with the undistorted delay of the initial photoemission feature.

If ignored, the background electrons shift spectral features and decrease the observed streaking amplitude. Furthermore, the generalized-projections retrieval cannot discern between unscattered and scattered electrons and thus will retrieve impossibly short attosecond pulse durations by fitting the ultrabroad background. Before retrieval, we hence either subtract a Shirley background or in the case of the restricted TDSE retrieval modified the fitting procedure to automatically subtract background by differentiation.

Split Shirley Background Subtraction

The Shirley background description assumes a constant electron energy loss function for unscattered electrons [153], what leads to a constant background between photoemission peaks and an error-function-like increase from high to low electron kinetic energy in peak areas. Instructions for its calculation can be found in [136, 154]. In our implementation, the background shape is retrieved from a photoelectron spectrum in an iterative way, and peak regions are defined by the experimenter. The technique is universally applicable but cannot grasp more complicated background shapes, i.e., due to secondary electron

emission at low kinetic energies. Furthermore, the exact choice of peak areas can influence the photoemission delay.

Differential Background Subtraction

During the restricted TDSE retrieval, an alternative background subtraction can remedy these disadvantages. The procedure is illustrated in figure A.7. Every photoelectron energy bin is differentiated along the XUV-NIR delay axis before retrieval, eliminating all constant components without assumptions about their shape or the chance of experimenter influence. Before calculation of the merit function in the fit procedure, the fit spectrogram is also differentiated. The non-differentiated best-fit spectrogram can be calculated after the fit procedure using the retrieved parameters and the background by subtracting the resulting fit spectrogram from the experimental data.

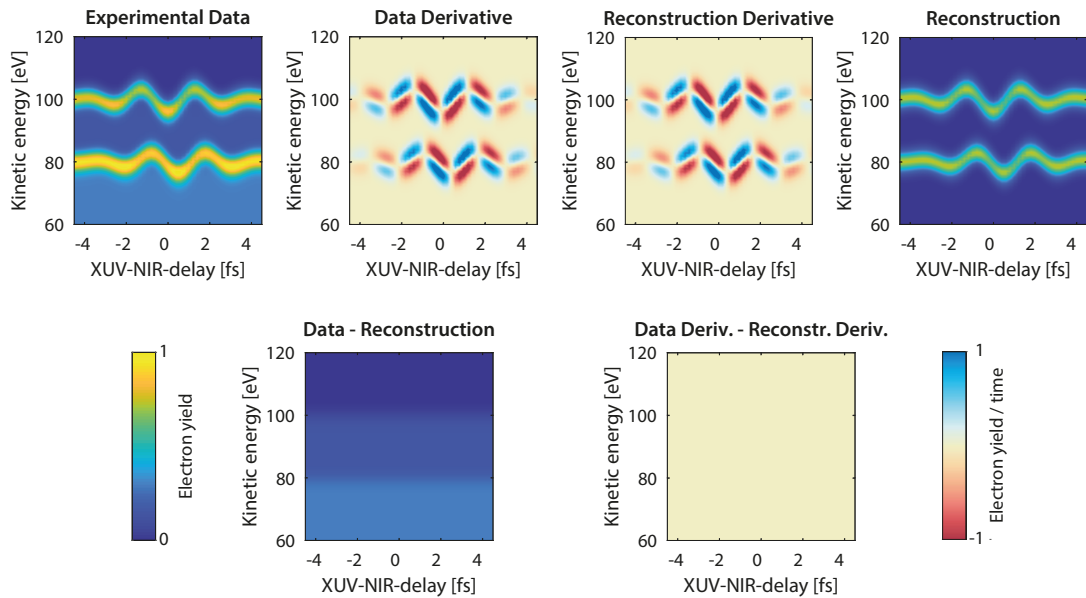


Figure A.7: Restricted TDSE retrieval of a simulated spectrogram with background. Top row, left to right: constant background is eliminated by differentiation along the XUV-NIR delay axis. The retrieval is run, and calculated spectrograms also differentiated before calculation of the merit function. The best-fit parameters are used to calculate the final retrieved spectrogram. Bottom row, left to right: comparison of data and reconstruction. Before differentiation, the retrieved and initial spectrogram differ exactly by the background. The differentiated data and reconstruction do not differ.

Appendix B

Experimental Tools

All experiments were carried out at the Max-Planck-Institute of Quantum Optics and the Chair for Laser and X-Ray Physics at the Technical University of Munich. Attosecond streaking spectroscopy is still pushing what is technologically feasible and requires highly specialized tools, often operated close to their limits. Therefore, no single laser or beamline can facilitate all experiments, and the right selection of source and beamline is key to experimental success. Combinations of three femtosecond lasers and three attosecond beamlines were employed to obtain the presented results. Most of this infrastructure is described in published work, which will be listed together with a short description. Major upgrades that were performed and required to achieve results presented in this thesis will be delineated.

B.1 FP2 Laser System

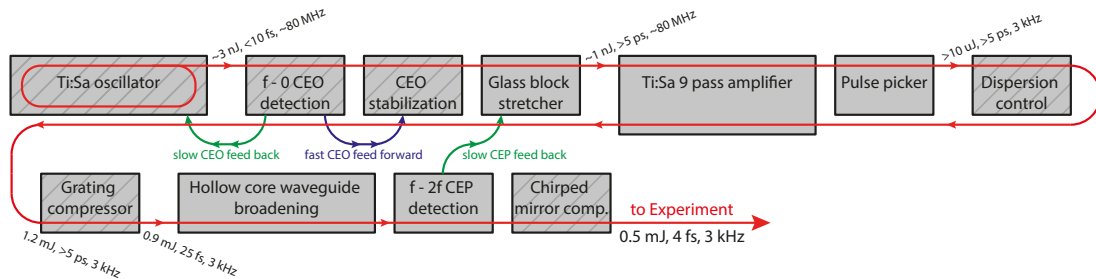


Figure B.1: The FP2 laser system, beam path in red, fast electronic feed-forward CEP stabilization in blue and slow electronic CEP stabilization feed-back in green. The hashed components were exchanged during the upgrade.

The Femtopower 2 laser system (FP2) is based on a commercial titanium-sapphire (Ti:Sa) oscillator and chirped-pulse-amplifier manufactured by Femtolasers Produktions GmbH. An overview of the system before a significant upgrade can be found in [155]. In the initial system, a train of laser pulses was created in a Ti:Sa oscillator (Femtolasers Rainbow). Its CEO frequency was measured using an f-to-0 scheme and then fixed in a fast feed-back scheme by manipulating the intra-cavity dispersion via the oscillator pump power. Since this pump modulation had an unintended impact on many cavity parameters,

the concept had limited operating range and could only provide CEP-stabilized pulses for a limited time. Significant dispersion changes were counteracted by manually moving a wedge in the laser cavity. Subsequently, the oscillator pulses were temporally stretched, amplified and a small number of pulses with a constant CEP picked in a nine pass Ti:Sa amplifier (Femtolasers Femtopower). Recompression was achieved using a four-prism compressor. To counteract gain narrowing during the amplification, the pulses were spectrally shaped using anti-Gaussian filters during the amplification and spectrally broadened in a neon filled hollow-core waveguide after compression. The spectrum after broadening was more than octave-spanning, allowing to determine and counteract slow drifts in the CEP in an f-to-2f scheme feeding back to a wedge pair in the stretcher. Compression was finalized in a four-pair chirped mirror compressor and a SiO₂ wedge pair. Typical pulses sent to the experiment had 0.5 mJ pulse energy at 3.8 fs intensity FWHM duration and 780nm central wavelength.

Figure B.1 shows the reworked setup and typical pulse parameters, all hashed components were exchanged or rebuilt. The oscillator is now replaced by a hermetically sealed Ti:Sa oscillator (Femtolasers Rainbow 2), which significantly increases overall stability during alignment and operation. Further improvement of stability is achieved by changing the CEO frequency stabilization from the feed-back to a feed-forward scheme (Femtolasers CEP4) [156]: After a similar CEP detection, downstream of the laser cavity, the whole frequency comb spectrum is red-shifted by the unstabilized CEO frequency using an acousto optic modulator. Because a non-vanishing CEO frequency manifests as a spectral shift of all frequency comb modes, this shifting fixes the CEO frequency to zero, resulting in identical pulse fields along the pulse train. Slow drifts are automatically counteracted by changing the intra-cavity dispersion via the oscillator crystal temperature and the aforementioned wedge, allowing constantly operating the laser at fixed CEP. Furthermore, an acousto optic modulator replaces the anti-Gauss filters in the amplifier, which besides arbitrary spectral shaping allows arbitrary changes to the spectral phase of the laser pulses. This allows to correct for the third order dispersion caused by a transmission grating compressor and therefore replacing the prism compressor, further increasing stability and throughput. The FWHM intensity duration and pulse energy sent to the hollow core waveguide for spectral broadening were comparable before and after the upgrade. However, comparable broadening is now achieved at significantly lower neon pressures, 1.6 bar vs. 2.0 bar, proving increased peak intensity before broadening, suggesting better compression of the low-intensity pulse structure not characterized by the FWHM duration and better spatial mode properties. The latter is affirmed by an increased throughput of the hollow core waveguide. The amount of dispersive material after the spectral broadening stage is optimized to allow for a compressor containing only three matched pairs of chirped mirrors, decreasing phase oscillations and thus the pulse duration sent to the experiment to below 3 fs while increasing the pulse energy by 12%. In the downstream high-harmonic generation, this translates to a three-fold increase in XUV flux around 100 eV photon energy.

B.2 FP3 Laser System

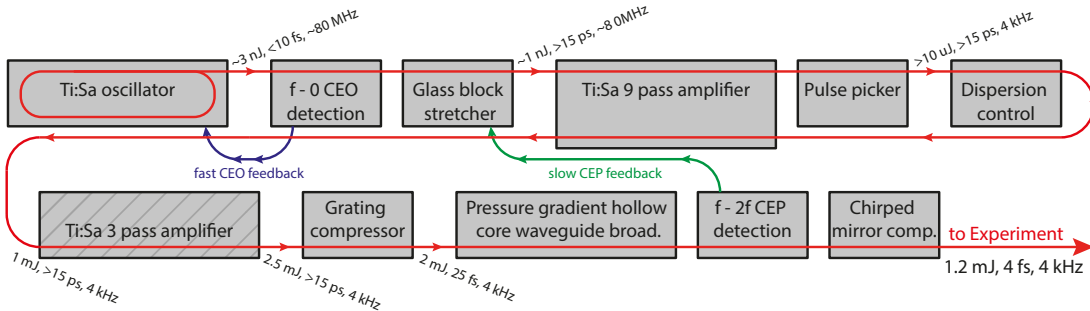


Figure B.2: The FP3 laser system, beam path in red, fast and slow electronic CEP stabilization feed-back in blue and green. The booster amplification stage (hashed) was partially rebuilt due to a pump laser upgrade.

The Femtopower 3 laser system (FP3) oscillator and f_{CEO} feed-back configuration are comparable to that of FP2 before the upgrade and the amplifier configuration of FP2 after the upgrade. After the first stage of amplification, a second three-pass Ti:Sa amplifier boosts the pulse energy by 200 % to 3 mJ before recompression in a transmission grating amplifier. Figure B.2 gives an overview of the main components and pulse parameters during the different stages of amplification and manipulation, an in-depth description is found in [157]. Changes to the system were necessary since the extreme pulse energy caused self-focusing and filamentation in the noble gas before and after a standard hollow core waveguide, which prevented efficient spectral broadening due to spatial mode deterioration. A differentially pumped waveguide is now employed [158], which consists of a 380 μm inner diameter, 1.4 m long fiber that is cleaved at the center to create a gas inlet. The beam entrance and exit volumes are continuously evacuated to prevent nonlinear interaction before and after the waveguide, allowing efficient broadening at the cost of permanent gas consumption. Initially planned and commissioned using neon as a nonlinear medium, a surge in pricing prevented its ongoing use, such that the system is now operated using helium. However, nothing but the inlet pressure had to be adapted to regain adequate spectral broadening. The initial booster stage pump lasers (2x Thales Optronique S.A.S, ETNA HP) reached their end of life and were substituted by a lower power replacement (Photonics Industries International Inc., DM100), decreasing the output pulse energy to 2.5 mJ after the CPA. The losses are entirely equalized by higher throughput in the hollow core waveguide due to an improved spatial mode. The final ~1.2 mJ pulses are centered around 800 nm wavelength and reach durations <math><4\text{ fs}</math>.

B.3 The Femtopower at the Technical University of Munich

The Femtopower laser system in the attosecond laboratory at the Technical University of Munich is a next-generation boosted Ti:Sa chirped pulse amplification system. The

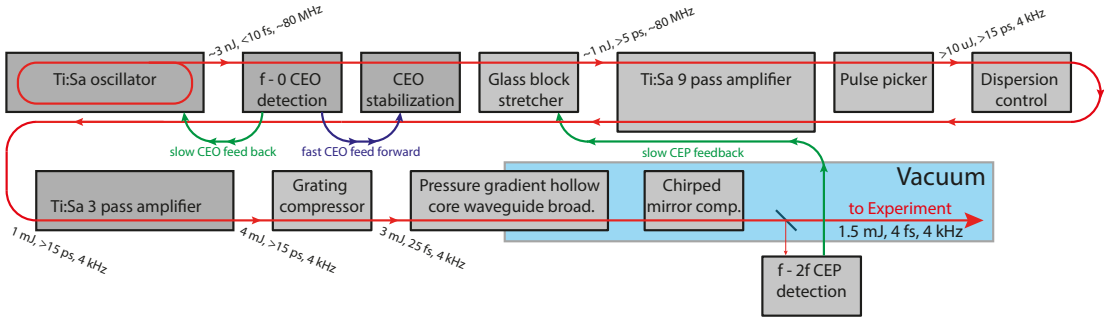


Figure B.3: The Femtopower laser system at the Technical University of Munich, beam path in red, fast electronic feed-forward CEP stabilization in blue and slow electronic CEP stabilization feed-back in green.

oscillator and front end resemble the FP2 System, including a feed-forward CEP stabilization, while the second amplification stage is designed like the FP3 booster. The new generation allows for increased efficiency and higher pulse energies. Therefore, and due to longer but less tight broadening conditions in two helium-filled, 1 m length, 500 μm diameter hollow core waveguides, it offers increased pulse energy (1.5 mJ) after spectral broadening. A further advance is that the fiber exit couples the light pulses directly into the experiment vacuum system, mitigating losses and allowing to only use two instead of six pairs of chirped mirrors. Figure B.3 shows a coarse sketch of the system, detailed information about the system can be found in [159, 160].

B.4 The Attosecond Beamline at the Technical University of Munich

The attosecond beamline at the Technical University of Munich is an improved version of first-generation attosecond beamlines [46, 161], which offer maximum stability due to co-propagation of the XUV and NIR pulses. The setup resembles the scheme presented in figure 4.3. The design is described in [159, 160, 162, 163]. After high-harmonic generation of an attosecond pulse train in a usually neon filled ceramic tube target with ~ 2 mm diameter and pre-drilled ~ 300 μm entrance and exit holes, the XUV and NIR laser pulses are spatially separated by a small metallic and bigger concentric nitrocellulose filter. Due to the small divergence of the XUV, its majority passes through the metal filter, while the outer part of the mode is blocked by the nitrocellulose filter. This instead transmits the NIR laser pulse, such that an annular NIR pulse co-propagates with the central XUV pulse. A concentric double mirror, whose inner part also acts as band-pass in the intensity gating process which isolates a single attosecond pulse from the generated pulse train and controls the XUV-NIR-delay for the streak camera experiment, refocuses both pulses on an effusive gas nozzle, which introduces the gaseous sample. Photoelectrons are recorded using a self-built time-of-flight spectrometer [99], which uses a high-voltage lens to uniformly increase the electron acceptance angle in the whole energy region relevant to attosecond streaking. Compared to commercially available time-of-flight spectrometers,

this makes collected data more robust against incorrectly calibrated lens amplification, which can induce systematic photoemission delay errors when attosecond pulse chirp is present [82].

B.5 The Bulk and Gas Phase Beamline AS2

Helium shake-up experiments were performed using the AS2 beamline, which was designed to accommodate advanced NIR and XUV reshaping after high-harmonic generation, as well as transient absorption experiments in bulk materials. After high-harmonic generation, which is achieved similar as in section B.4, the XUV and NIR laser pulses are spatially separated in a Mach-Zehnder-interferometer using a perforated mirror. After separation, the XUV beam can be filtered using various metal foils and is then deflected by a 45° mirror to reach a second perforated mirror, which recombines the XUV with the NIR laser pulse. The 45° reflection also serves as a band-pass filter to achieve an isolated attosecond pulse. Due to the real spatial separation of the XUV and NIR light, more complicated XUV filtering setups are realizable. After recombination, both pulses are focused using a toroidal mirror into the interaction volume under a commercially available time-of-flight spectrometer (STEFAN KAESDORF, Geraete für Forschung und Industrie, ETF10). Gaseous samples are introduced using an effusive gas nozzle. After the interaction volume, a toroidal grating reimages the XUV focus onto an XUV CCD camera allowing in-situ characterization of the XUV radiation used in the experiment. Detailed information about the apparatus can be found in [164, 165].

B.6 The Surface Science Beamline AS3

The high-harmonic generation, beam guiding and interferometer setup of the AS3 beamline is similar to that of the attosecond beamline at the Technical University of Munich. Surface experiments require base pressures in the 10×10^{-11} mbar range to maintain pristine surfaces during the measurement time. Such pressure is achieved using a combined titanium-sublimation and liquid nitrogen cooled cryo-pump additional to a turbo pump in the fully bakeable experimental chamber and maintained by a total of three differential pumping stages and a skimmer which intercept gas molecules introduced for high-harmonic generation that travel towards the experimental chamber. Furthermore, a separable preparation chamber allows to prepare and clean crystal surfaces in-situ without contaminating the experiment volume using evaporators, a gas dosing system, cleaver, sputter gun and electron impact heating to >2500 K. These samples can be characterized prior to attosecond experiments using low energy electron diffraction, thermo-desorption, and x-ray photoelectron spectroscopy. The different preparation tools can be approached using rotary flanges that are sealed using doubly differentially pumped Teflon-slip-gaskets. The sample holder can be cooled using a continuous-flow cryostat and liquid nitrogen or helium to achieve sample temperatures below 20 K during measurements or preparations. Photoelectrons can be detected using either a commercially available time-of-flight spectrometer (STEFAN KAESDORF, Geraete für Forschung und Industrie, ETF11,

elongated version) or a commercially available hemispherical analyzer (SPECS GmbH, PHOIBOS 100, elongated version). Charging of dielectric samples during photoemission studies can be prevented using an electron-flood gun. Detailed information on the setup can be found in [166].

Bibliography

- [1] H. Hertz. “Ueber einen Einfluss des ultravioletten Lichtes auf die electriche Entladung”. In: *Ann. der Phys. und Chemie* 267.8 (1887), pp. 983–1000. DOI: 10.1002/andp.18872670827 (cit. on p. 1).
- [2] W. Hallwachs. “Ueber den Einfluss des Lichtes auf electrostatisch geladene Körper”. In: *Ann. der Phys. und Chemie* 269.2 (1888), pp. 301–312. DOI: 10.1002/andp.18882690206 (cit. on p. 1).
- [3] A. Einstein. “Über einen die Erzeugung und Verwandlung des Lichtes betreffenden heuristischen Gesichtspunkt”. In: *Ann. Phys.* 322.6 (1905), pp. 132–148. DOI: 10.1002/andp.19053220607 (cit. on p. 1).
- [4] M. Planck. “Ueber das Gesetz der Energieverteilung im Normalspectrum”. In: *Ann. Phys.* 309.3 (1901), pp. 553–563. DOI: 10.1002/andp.19013090310 (cit. on p. 1).
- [5] F. Krausz. “The birth of attosecond physics and its coming of age”. In: *Phys. Scr.* 91.6 (2016), p. 063011. DOI: 10.1088/0031-8949/91/6/063011 (cit. on p. 1).
- [6] A. L. Cavalieri et al. “Attosecond spectroscopy in condensed matter”. In: *Nature* 449.7165 (2007), pp. 1029–1032. DOI: 10.1038/nature06229 (cit. on pp. 1, 30, 33, 73, 74, 81, 94).
- [7] M. Schultze et al. “Delay in photoemission.” In: *Science* 328.5986 (2010), pp. 1658–62. DOI: 10.1126/science.1189401 (cit. on pp. 1, 33, 35, 95).
- [8] J. Caillat et al. “Attosecond Resolved Electron Release in Two Color Near Threshold Photoionization of N₂”. In: *Phys. Rev. Lett.* 106.9 (2011), p. 093002. DOI: 10.1103/PhysRevLett.106.093002 (cit. on p. 1).
- [9] S. Haessler et al. “Phase-resolved attosecond near-threshold photoionization of molecular nitrogen”. In: *Phys. Rev. A* 80.1 (2009), p. 011404. DOI: 10.1103/PhysRevA.80.011404 (cit. on p. 1).
- [10] M. Huppert et al. “Attosecond Delays in Molecular Photoionization”. In: *Phys. Rev. Lett.* 117.9 (2016), p. 093001. DOI: 10.1103/PhysRevLett.117.093001 (cit. on pp. 1, 57, 65).
- [11] K. Klünder et al. “Probing Single-Photon Ionization on the Attosecond Time Scale”. In: *Phys. Rev. Lett.* 106.14 (2011), p. 143002. DOI: 10.1103/PhysRevLett.106.143002 (cit. on p. 1).
- [12] C. Palatchi et al. “Atomic delay in helium, neon, argon and krypton”. In: *J. Phys. B At. Mol. Opt. Phys.* 47.24 (2014), p. 245003. DOI: 10.1088/0953-4075/47/24/245003 (cit. on p. 1).

- [13] M. Sabbar et al. “Resonance Effects in Photoemission Time Delays”. In: *Phys. Rev. Lett.* 115.13 (2015), p. 133001. DOI: 10.1103/PhysRevLett.115.133001 (cit. on p. 1).
- [14] S. Heuser et al. “Angular dependence of photoemission time delay in helium”. In: *Phys. Rev. A* 94.6 (2016), p. 063409. DOI: 10.1103/PhysRevA.94.063409 (cit. on pp. 1, 59).
- [15] M. Kotur et al. “Spectral phase measurement of a Fano resonance using tunable attosecond pulses”. In: *Nat. Commun.* 7 (2016), p. 10566. DOI: 10.1038/ncomms10566 (cit. on p. 1).
- [16] V. Gruson et al. “Attosecond dynamics through a Fano resonance: Monitoring the birth of a photoelectron”. In: *Science* 354.6313 (2016), pp. 734–738. DOI: 10.1126/science.aah5188 (cit. on p. 1).
- [17] E. P. Månsson et al. “Double ionization probed on the attosecond timescale”. In: *Nat. Phys.* 10.3 (2014), pp. 207–211. DOI: 10.1038/nphys2880 (cit. on p. 1).
- [18] S. Neppl et al. “Attosecond Time-Resolved Photoemission from Core and Valence States of Magnesium”. In: *Phys. Rev. Lett.* 109.8 (2012), p. 087401. DOI: 10.1103/PhysRevLett.109.087401 (cit. on pp. 1, 33).
- [19] S. Neppl et al. “Direct observation of electron propagation and dielectric screening on the atomic length scale”. In: *Nature* 517.7534 (2015), pp. 342–346. DOI: 10.1038/nature14094 (cit. on pp. 1, 30, 74, 81, 105).
- [20] L. Seiffert et al. “Attosecond chronoscopy of electron scattering in dielectric nanoparticles”. In: *Nat. Phys.* 13.8 (2017), pp. 766–770. DOI: 10.1038/nphys4129 (cit. on pp. 1, 74).
- [21] C. Chen et al. “Distinguishing attosecond electron–electron scattering and screening in transition metals”. In: *Proc. Natl. Acad. Sci.* 114.27 (2017), E5300–E5307. DOI: 10.1073/pnas.1706466114 (cit. on pp. 1, 74).
- [22] Z. Tao et al. “Direct time-domain observation of attosecond final-state lifetimes in photoemission from solids”. In: *Science* 353.6294 (2016), pp. 62–67. DOI: 10.1126/science.aaf6793 (cit. on pp. 1, 74).
- [23] J.-C. Diels and W. Rudolph. *Ultrashort laser pulse phenomena*. Burlington: Academic Press, 2006. DOI: 10.1016/B978-012215493-5/50000-8 (cit. on p. 3).
- [24] H. Shull and G. G. Hall. “Atomic Units”. In: *Nature* 184.4698 (1959), pp. 1559–1560. DOI: 10.1038/1841559a0 (cit. on p. 3).
- [25] P. J. Mohr, D. B. Newell, and B. N. Taylor. “CODATA recommended values of the fundamental physical constants: 2014”. In: *Rev. Mod. Phys.* 88.3 (2016), p. 035009. DOI: 10.1103/RevModPhys.88.035009 (cit. on p. 3).
- [26] S. P. Hau-Riege. *High-Intensity X-Rays - Interaction with Matter*. Weinheim: Wiley-VCH Verlag, 2011. DOI: 10.1002/9783527636365 (cit. on p. 3).

-
- [27] R. Kienberger et al. “Atomic transient recorder.” In: *Nature* 427.6977 (2004), pp. 817–821. DOI: 10.1038/nature02277 (cit. on pp. 4, 17, 22).
- [28] Nobelprize.org. *All Nobel Prizes in Physics*. 2014 (cit. on p. 8).
- [29] L. Eisenbud. “The Formal Properties of Nuclear Collisions”. PhD thesis. Princeton Univ., 1948 (cit. on pp. 11, 67).
- [30] E. P. Wigner. “Lower Limit for the Energy Derivative of the Scattering Phase Shift”. In: *Phys. Rev.* 98.1 (1955), pp. 145–147. DOI: 10.1103/PhysRev.98.145 (cit. on pp. 11, 15).
- [31] F. T. Smith. “Lifetime Matrix in Collision Theory”. In: *Phys. Rev.* 118.1 (1960), pp. 349–356. DOI: 10.1103/PhysRev.118.349 (cit. on p. 11).
- [32] P. A. Martin. “Time Delay of Quantum Scattering Processes”. In: *New Dev. Math. Phys.* Ed. by H. Mitter and L. Pittner. Wien: Springer-Verlag, 1981. DOI: 10.1007/978-3-7091-8642-8 (cit. on p. 11).
- [33] H. Haberzettl and R. Workman. “Time delay in a multichannel formalism”. In: *Phys. Rev. C* 76.5 (2007), p. 058201. DOI: 10.1103/PhysRevC.76.058201 (cit. on p. 12).
- [34] J. M. Dahlström, A. L’Huillier, and A. Maquet. “Introduction to attosecond delays in photoionization”. In: *J. Phys. B At. Mol. Opt. Phys.* 45.18 (2012), p. 183001. DOI: 10.1088/0953-4075/45/18/183001 (cit. on p. 15).
- [35] R. Pazourek, S. Nagele, and J. Burgdörfer. “Attosecond chronoscopy of photoemission”. In: *Rev. Mod. Phys.* 87.3 (2015), pp. 765–802. DOI: 10.1103/RevModPhys.87.765 (cit. on pp. 15, 31, 35).
- [36] H. Muller. “Reconstruction of attosecond harmonic beating by interference of two-photon transitions”. In: *Appl. Phys. B* 74.S1 (2002), S17–S21. DOI: 10.1007/s00340-002-0894-8 (cit. on p. 17).
- [37] U. Heinzmann and J. H. Dil. “Spin-orbit-induced photoelectron spin polarization in angle-resolved photoemission from both atomic and condensed matter targets”. In: *J. Phys. Condens. Matter* 24.17 (2012), p. 173001. DOI: 10.1088/0953-8984/24/17/173001 (cit. on p. 17).
- [38] M. Fanciulli et al. “Spin Polarization and Attosecond Time Delay in Photoemission from Spin Degenerate States of Solids”. In: *Phys. Rev. Lett.* 118.6 (2017), p. 067402. DOI: 10.1103/PhysRevLett.118.067402 (cit. on p. 17).
- [39] A. McPherson et al. “Studies of multiphoton production of vacuum-ultraviolet radiation in the rare gases”. In: *J. Opt. Soc. Am. B* 4.4 (1987), pp. 595–601. DOI: 10.1364/JOSAB.4.000595 (cit. on p. 17).
- [40] M. Ferray et al. “Multiple-harmonic conversion of 1064 nm radiation in rare gases”. In: *J. Phys. B At. Mol. Opt. Phys.* 21.3 (1988), pp. L31–L35. DOI: 10.1088/0953-4075/21/3/001 (cit. on p. 17).

- [41] G. Marcus et al. “Subfemtosecond K-Shell Excitation with a Few-Cycle Infrared Laser Field”. In: *Phys. Rev. Lett.* 108.2 (2012), p. 023201. DOI: 10.1103/PhysRevLett.108.023201 (cit. on p. 17).
- [42] J. L. Krause, K. J. Schafer, and K. C. Kulander. “High-order harmonic generation from atoms and ions in the high intensity regime”. In: *Phys. Rev. Lett.* 68.24 (1992), pp. 3535–3538. DOI: 10.1103/PhysRevLett.68.3535 (cit. on p. 18).
- [43] P. B. Corkum. “Plasma perspective on strong field multiphoton ionization”. In: *Phys. Rev. Lett.* 71.13 (1993), pp. 1994–1997. DOI: 10.1103/PhysRevLett.71.1994 (cit. on p. 18).
- [44] M. V. Ammosov, N. B. Delone, and V. P. Krainov. “Tunnel ionization of complex atoms and of atomic ions in an alternating electromagnetic field”. In: *Zh. Eksp. Teor. Fiz.* 91 (1986), pp. 2008–2013 (cit. on p. 20).
- [45] M. T. Hassan et al. “Optical attosecond pulses and tracking the nonlinear response of bound electrons”. In: *Nature* 530.7588 (2016), pp. 66–70. DOI: 10.1038/nature16528 (cit. on p. 18).
- [46] M. Hentschel et al. “Attosecond metrology.” In: *Nature* 414.6863 (2001), pp. 509–513. DOI: 10.1038/35107000 (cit. on pp. 21, 25, 110).
- [47] A. Baltuska et al. “Attosecond control of electronic processes by intense light fields.” In: *Nature* 421.6923 (2003), pp. 611–615. DOI: 10.1038/nature01414 (cit. on p. 21).
- [48] A. Rundquist. “Phase-Matched Generation of Coherent Soft X-rays”. In: *Science* 280.5368 (1998), pp. 1412–1415. DOI: 10.1126/science.280.5368.1412 (cit. on p. 21).
- [49] A. L’Huillier, K. J. Schafer, and K. C. Kulander. “Theoretical aspects of intense field harmonic generation”. In: *J. Phys. B At. Mol. Opt. Phys.* 24.15 (1991), pp. 3315–3341. DOI: 10.1088/0953-4075/24/15/004 (cit. on p. 21).
- [50] A. Paul et al. “Phase-Matching Techniques for Coherent Soft X-Ray Generation”. In: *IEEE J. Quantum Electron.* 42.1 (2006), pp. 14–26. DOI: 10.1109/JQE.2005.859914 (cit. on pp. 21, 22).
- [51] P. Salières, A. L’Huillier, and M. Lewenstein. “Coherence Control of High-Order Harmonics”. In: *Phys. Rev. Lett.* 74.19 (1995), pp. 3776–3779. DOI: 10.1103/PhysRevLett.74.3776 (cit. on p. 21).
- [52] A. D. Shiner et al. “Wavelength Scaling of High Harmonic Generation Efficiency”. In: *Phys. Rev. Lett.* 103.7 (2009), p. 073902. DOI: 10.1103/PhysRevLett.103.073902 (cit. on p. 22).
- [53] C. M. Heyl et al. “Scale-invariant nonlinear optics in gases”. In: *Optica* 3.1 (2016), pp. 75–81. DOI: 10.1364/OPTICA.3.000075 (cit. on p. 22).
- [54] D. Bradley and G. New. “Ultrashort pulse measurements”. In: *Proc. IEEE* 62.3 (1974), pp. 313–345. DOI: 10.1109/PROC.1974.9427 (cit. on p. 22).

-
- [55] E. Goulielmakis et al. “Direct measurement of light waves.” In: *Science* 305.5688 (2004), pp. 1267–1269. DOI: 10.1126/science.1100866 (cit. on p. 25).
- [56] J. Gagnon and V. S. Yakovlev. “The direct evaluation of attosecond chirp from a streaking measurement”. In: *Appl. Phys. B* 103.2 (2011), pp. 303–309. DOI: 10.1007/s00340-010-4358-2 (cit. on pp. 26, 94).
- [57] M. Kitzler et al. “Quantum Theory of Attosecond XUV Pulse Measurement by Laser Dressed Photoionization”. In: *Phys. Rev. Lett.* 88.17 (2002), p. 173904. DOI: 10.1103/PhysRevLett.88.173904 (cit. on p. 26).
- [58] V. S. Yakovlev et al. “Attosecond Streaking Enables the Measurement of Quantum Phase”. In: *Phys. Rev. Lett.* 105.7 (2010), p. 073001. DOI: 10.1103/PhysRevLett.105.073001 (cit. on pp. 26, 96, 99).
- [59] F. Quéré, Y. Mairesse, and J. Itatani. “Temporal characterization of attosecond XUV fields”. In: *J. Mod. Opt.* 52.2-3 (2005), pp. 339–360. DOI: 10.1080/09500340412331307942 (cit. on pp. 26, 28).
- [60] S. Nagele et al. “Time-resolved photoemission by attosecond streaking: extraction of time information”. In: *J. Phys. B At. Mol. Opt. Phys.* 44.8 (2011), p. 081001. DOI: 10.1088/0953-4075/44/8/081001 (cit. on p. 31).
- [61] M. Y. Ivanov and O. Smirnova. “How Accurate Is the Attosecond Streak Camera?” In: *Phys. Rev. Lett.* 107.21 (2011), p. 213605. DOI: 10.1103/PhysRevLett.107.213605 (cit. on pp. 31, 35).
- [62] R. Pazourek, S. Nagele, and J. Burgdörfer. “Time-resolved photoemission on the attosecond scale: opportunities and challenges”. In: *Faraday Discuss.* 163 (2013), pp. 353–376. DOI: 10.1039/c3fd00004d (cit. on p. 31).
- [63] R. Pazourek. “Time-resolved photoemission in one- and two-electron atoms”. PhD thesis. Technische Universität Wien, 2013 (cit. on pp. 31, 53).
- [64] J. C. Baggesen and L. B. Madsen. “Polarization Effects in Attosecond Photoelectron Spectroscopy”. In: *Phys. Rev. Lett.* 104.4 (2010), p. 043602. DOI: 10.1103/PhysRevLett.104.043602 (cit. on pp. 35, 52).
- [65] J. C. Baggesen and L. B. Madsen. “Erratum: Polarization Effects in Attosecond Photoelectron Spectroscopy [Phys. Rev. Lett. 104 , 043602 (2010)]”. In: *Phys. Rev. Lett.* 104.20 (2010), p. 209903. DOI: 10.1103/PhysRevLett.104.209903 (cit. on pp. 35, 52).
- [66] J. Feist et al. “Time delays for attosecond streaking in photoionization of neon”. In: *Phys. Rev. A* 89.3 (2014), p. 033417. DOI: 10.1103/PhysRevA.89.033417 (cit. on p. 35).
- [67] L. R. Moore et al. “Time delay between photoemission from the 2p and 2s subshells of neon”. In: *Phys. Rev. A* 84.6 (2011), p. 061404. DOI: 10.1103/PhysRevA.84.061404 (cit. on p. 35).

- [68] A. S. Kheifets and I. A. Ivanov. “Delay in Atomic Photoionization”. In: *Phys. Rev. Lett.* 105.23 (2010), p. 233002. DOI: 10.1103/PhysRevLett.105.233002 (cit. on p. 35).
- [69] A. S. Kheifets. “Time delay in valence-shell photoionization of noble-gas atoms”. In: *Phys. Rev. A* 87.6 (2013), p. 063404. DOI: 10.1103/PhysRevA.87.063404 (cit. on p. 35).
- [70] A. S. Kheifets et al. “Dipole phase and photoelectron group delay in inner-shell photoionization”. In: *Phys. Rev. A* 92.6 (2015), p. 063422. DOI: 10.1103/PhysRevA.92.063422 (cit. on p. 35).
- [71] C.-H. Zhang and U. Thumm. “Electron-ion interaction effects in attosecond time-resolved photoelectron spectra”. In: *Phys. Rev. A* 82.4 (2010), p. 043405. DOI: 10.1103/PhysRevA.82.043405 (cit. on p. 35).
- [72] M. Isinger et al. “Photoionization in the time and frequency domain”. In: *Science* 358.6365 (2017), pp. 893–896. DOI: 10.1126/science.aao7043 (cit. on p. 35).
- [73] M. Ossiander et al. “Attosecond correlation dynamics”. In: *Nat. Phys.* 13.3 (2017), pp. 280–285. DOI: 10.1038/nphys3941 (cit. on pp. 35, 38, 41–44, 46, 47, 52, 54, 55, 104).
- [74] R. Pazourek et al. “Attosecond Streaking of Correlated Two-Electron Transitions in Helium”. In: *Phys. Rev. Lett.* 108.16 (2012), p. 163001. DOI: 10.1103/PhysRevLett.108.163001 (cit. on pp. 36, 52, 54, 56, 99).
- [75] J. S. Parker et al. “Time delay between singly and doubly ionizing wavepackets in laser-driven helium”. In: *J. Phys. B At. Mol. Opt. Phys.* 36.21 (2003), pp. L393–L400. DOI: 10.1088/0953-4075/36/21/L04 (cit. on p. 36).
- [76] J. Feist et al. “Nonsequential two-photon double ionization of helium”. In: *Phys. Rev. A* 77.4 (2008), p. 043420. DOI: 10.1103/PhysRevA.77.043420 (cit. on p. 36).
- [77] J. Colgan and M. S. Pindzola. “Core-Excited Resonance Enhancement in the Two-Photon Complete Fragmentation of Helium”. In: *Phys. Rev. Lett.* 88.17 (2002), p. 173002. DOI: 10.1103/PhysRevLett.88.173002 (cit. on p. 36).
- [78] S. Laulan and H. Bachau. “Correlation effects in two-photon single and double ionization of helium”. In: *Phys. Rev. A* 68.1 (2003), p. 013409. DOI: 10.1103/PhysRevA.68.013409 (cit. on p. 36).
- [79] M. S. Pindzola et al. “The time-dependent close-coupling method for atomic and molecular collision processes”. In: *J. Phys. B At. Mol. Opt. Phys.* 40.7 (2007), R39–R60. DOI: 10.1088/0953-4075/40/7/R01 (cit. on p. 36).
- [80] R. Wehlitz et al. “Angular distributions of helium satellites $\text{He} + n\ell$ ($n=2-7$)”. In: *J. Phys. B At. Mol. Opt. Phys.* 26.22 (1993), pp. L783–L788. DOI: 10.1088/0953-4075/26/22/002 (cit. on pp. 37, 42, 45).
- [81] F. A. Siegrist. “Attosecond Dynamics Based on Electron Correlation and Excitation”. Master Thesis. Technische Universität München, 2016 (cit. on p. 39).

-
- [82] S. Neppel. “Attosecond Time-Resolved Photoemission from Surfaces and Interfaces”. PhD thesis. Technische Universität München, 2012 (cit. on pp. 41, 76, 80, 81, 111).
- [83] A. Palacios, C. W. McCurdy, and T. N. Rescigno. “Extracting amplitudes for single and double ionization from a time-dependent wave packet”. In: *Phys. Rev. A* 76.4 (2007), p. 043420. DOI: 10.1103/PhysRevA.76.043420 (cit. on p. 49).
- [84] F. A. Gianturco, R. R. Lucchese, and N. Sanna. “Calculation of low energy elastic cross sections for electron CF₄ scattering”. In: *J. Chem. Phys.* 100.9 (1994), pp. 6464–6471. DOI: 10.1063/1.467237 (cit. on pp. 49, 65).
- [85] A. P. P. Natalense and R. R. Lucchese. “Cross section and asymmetry parameter calculation for sulfur 1s photoionization of SF₆”. In: *J. Chem. Phys.* 111.12 (1999), pp. 5344–5348. DOI: 10.1063/1.479794 (cit. on pp. 49, 65).
- [86] P. Hockett et al. “Time delay in molecular photoionization”. In: *J. Phys. B At. Mol. Opt. Phys.* 49.9 (2016), p. 095602. DOI: 10.1088/0953-4075/49/9/095602 (cit. on pp. 49, 65, 66).
- [87] J. M. Hollas. “Photoelectron spectroscopy”. In: *High Resolut. Spectrosc.* London: Butterworths, 1982, pp. 435–480. DOI: B978-0-408-10605-4.50012-0 (cit. on p. 51).
- [88] P. R. Woodruff and J. A. R. Samson. “Measurements of partial cross sections and autoionization in the photoionization of helium to He+(N=2)”. In: *Phys. Rev. A* 25.2 (1982), pp. 848–856. DOI: 10.1103/PhysRevA.25.848 (cit. on pp. 51, 56).
- [89] G. W. Erickson. “Energy levels of one-electron atoms”. In: *J. Phys. Chem. Ref. Data* 6.3 (1977), pp. 831–870. DOI: 10.1063/1.555557 (cit. on p. 51).
- [90] P. Ramachandran and G. Varoquaux. “Mayavi: 3D Visualization of Scientific Data”. In: *Comput. Sci. Eng.* 13.2 (2011), pp. 40–51. DOI: 10.1109/MCSE.2011.35 (cit. on p. 52).
- [91] U. Fano and J. W. Cooper. “Spectral Distribution of Atomic Oscillator Strengths”. In: *Rev. Mod. Phys.* 40.3 (1968), pp. 441–507. DOI: 10.1103/RevModPhys.40.441 (cit. on p. 57).
- [92] G. C. Baldwin and G. S. Klaiber. “Photo-Fission in Heavy Elements”. In: *Phys. Rev.* 71.1 (1947), pp. 3–10. DOI: 10.1103/PhysRev.71.3 (cit. on p. 57).
- [93] J. P. Connerade. “Controlled Collapse and the Profiles of ”Giant Resonances””. In: *Giant Reson. Atoms, Mol. Solids*. Ed. by J. P. Connerade, J. M. Esteve, and R. C. Karnatak. Vol. 151. NATO ASI Series. New York: Springer Science+Business Media, 1987, pp. 3–23. DOI: 10.1007/978-1-4899-2004-1 (cit. on p. 57).
- [94] G. Wendin. “Giant dipole resonance in 4d photo absorption of atomic barium”. In: *Phys. Lett. A* 46.2 (1973), pp. 119–120. DOI: 10.1016/0375-9601(73)90054-6 (cit. on p. 57).
- [95] M. Y. Amusia and J.-P. Connerade. “The theory of collective motion probed by light”. In: *Reports Prog. Phys.* 63.1 (2000), pp. 41–70. DOI: 10.1088/0034-4885/63/1/202 (cit. on p. 57).

- [96] J. P. Connerade. “Quantum defect theory in a double-valley potential”. In: *J. Phys. B* 15.24 (1982), pp. L881–L886. DOI: 10.1088/0022-3700/15/24/001 (cit. on p. 58).
- [97] T. N. Olney, G. Cooper, and C. Brion. “Quantitative studies of the photoabsorption (4.5–488 eV) and photoionization (9–59.5 eV) of methyl iodide using dipole electron impact techniques”. In: *Chem. Phys.* 232.1-2 (1998), pp. 211–237. DOI: 10.1016/S0301-0104(97)00368-6 (cit. on pp. 57, 68, 69, 79).
- [98] C. Cirelli et al. “Energy-Dependent Photoemission Time Delays of Noble Gas Atoms Using Coincidence Attosecond Streaking”. In: *IEEE J. Sel. Top. Quantum Electron.* 21.5 (2015), pp. 1–7. DOI: 10.1109/JSTQE.2015.2416152 (cit. on pp. 58, 103).
- [99] A. Kim. “Attosecond time-resolved photoemission from solid samples”. PhD thesis. Technische Universität München, 2014 (cit. on pp. 59, 110).
- [100] J. N. Cutler et al. “Chemical dependence of core-level linewidths and ligand-field splittings: High-resolution core-level photoelectron spectra of I4d levels”. In: *Phys. Rev. Lett.* 67.12 (1991), pp. 1531–1534. DOI: 10.1103/PhysRevLett.67.1531 (cit. on p. 59).
- [101] J. N. Cutler, G. M. Bancroft, and K. H. Tan. “Ligand-field splittings and core-level linewidths in I4d photoelectron spectra of iodine molecules”. In: *J. Chem. Phys.* 97.11 (1992), pp. 7932–7943. DOI: 10.1063/1.463468 (cit. on pp. 59, 61, 64).
- [102] D. W. Lindle et al. “Inner-shell photoemission from the iodine atom in CH₃I”. In: *Phys. Rev. A* 30.1 (1984), pp. 239–244. DOI: 10.1103/PhysRevA.30.239 (cit. on pp. 59, 60, 68, 69).
- [103] T. A. Carlson et al. “Angle resolved photoelectron spectroscopy of the valence shells in HI and CH₃I as a function of photon energy from 13 to 90 eV”. In: *J. Chem. Phys.* 80.8 (1984), pp. 3521–3527. DOI: 10.1063/1.447196 (cit. on pp. 59, 60).
- [104] L. Karlsson et al. “The NVV Auger electron spectrum of the HI molecule”. In: *J. Phys. B At. Mol. Opt. Phys.* 22.19 (1989), pp. 3001–3009. DOI: 10.1088/0953-4075/22/19/014 (cit. on p. 60).
- [105] M. Drescher et al. “Time-resolved atomic inner-shell spectroscopy”. In: *Nature* 419.6909 (2002), pp. 803–807. DOI: 10.1038/nature01143 (cit. on p. 63).
- [106] J. Campbell and T. Papp. “Width of the Atomic K–N₇ Levels”. In: *At. Data Nucl. Data Tables* 77.1 (2001), pp. 1–56. DOI: 10.1006/adnd.2000.0848 (cit. on p. 64).
- [107] J. P. Perdew and A. Zunger. “Self-interaction correction to density-functional approximations for many-electron systems”. In: *Phys. Rev. B* 23.10 (1981), pp. 5048–5079. DOI: 10.1103/PhysRevB.23.5048 (cit. on p. 65).
- [108] M. W. Schmidt et al. “General atomic and molecular electronic structure system”. In: *J. Comput. Chem.* 14.11 (1993), pp. 1347–1363. DOI: 10.1002/jcc.540141112 (cit. on pp. 66, 79).

-
- [109] K. L. Schuchardt et al. “Basis Set Exchange: A Community Database for Computational Sciences”. In: *J. Chem. Inf. Model.* 47.3 (2007), pp. 1045–1052. DOI: 10.1021/ci600510j (cit. on pp. 66, 79).
- [110] D. Feller. “The role of databases in support of computational chemistry calculations”. In: *J. Comput. Chem.* 17.13 (1996), pp. 1571–1586. DOI: 10.1002/(SICI)1096-987X(199610)17:13<1571::AID-JCC9>3.0.CO;2-P (cit. on pp. 66, 79).
- [111] P. L. Barbieri, P. A. Fantin, and F. E. Jorge. “Gaussian basis sets of triple and quadruple zeta valence quality for correlated wave functions”. In: *Mol. Phys.* 104.18 (2006), pp. 2945–2954. DOI: 10.1080/00268970600899018 (cit. on pp. 66, 79).
- [112] C. Campos and F. Jorge. “Triple zeta quality basis sets for atoms Rb through Xe: application in CCSD(T) atomic and molecular property calculations”. In: *Mol. Phys.* 111.2 (2013), pp. 167–173. DOI: 10.1080/00268976.2012.709282 (cit. on pp. 66, 79).
- [113] T. Yanai, D. P. Tew, and N. C. Handy. “A new hybrid exchange correlation functional using the Coulomb-attenuating method (CAM-B3LYP)”. In: *Chem. Phys. Lett.* 393.1-3 (2004), pp. 51–57. DOI: 10.1016/j.cplett.2004.06.011 (cit. on p. 66).
- [114] H. Friedrich. *Scattering Theory*. Heidelberg: Springer, 2016. DOI: 10.1007/978-3-662-48526-2 (cit. on p. 68).
- [115] V. K. Dolmatov et al. “Attosecond time delay in the photoionization of Mn in the region of the 3p→3d giant resonance”. In: *Phys. Rev. A* 91.5 (2015), p. 053415. DOI: 10.1103/PhysRevA.91.053415 (cit. on p. 68).
- [116] L. Argenti et al. “Control of photoemission delay in resonant two-photon transitions”. In: *Phys. Rev. A* 95.4 (2017), p. 043426. DOI: 10.1103/PhysRevA.95.043426 (cit. on pp. 68, 70).
- [117] U. Fano. “Effects of configuration interaction on intensities and phase shifts”. In: *Phys. Rev.* 124.6 (1961), pp. 1866–1878. DOI: 10.1103/PhysRev.124.1866 (cit. on p. 68).
- [118] U. Fano and J. W. Cooper. “Line Profiles in the Far-uv Absorption Spectra of the Rare Gases”. In: *Phys. Rev.* 137.5A (1965), A1364–A1379. DOI: 10.1103/PhysRev.137.A1364 (cit. on p. 68).
- [119] J. W. Cooper. “Interaction of Maxima in the Absorption of Soft X Rays”. In: *Phys. Rev. Lett.* 13.25 (1964), pp. 762–764. DOI: 10.1103/PhysRevLett.13.762 (cit. on p. 68).
- [120] F. Combet Farnoux and M. Ben Amar. “Inner and outer shell ionization for atomic iodine: calculation of cross-sections and angular distribution parameters”. In: *J. Electron Spectros. Relat. Phenomena* 41.1 (1986), pp. 67–87. DOI: 10.1016/0368-2048(86)80032-9 (cit. on p. 70).

- [121] S. Pabst, D. Wang, and R. Santra. “Driving Rabi oscillations at the giant dipole resonance in xenon”. In: *Phys. Rev. A* 92.5 (2015), p. 053424. DOI: 10.1103/PhysRevA.92.053424 (cit. on p. 70).
- [122] M. Magrakvelidze, M. E.-A. Madjet, and H. S. Chakraborty. “Attosecond delay of xenon 4d photoionization at the giant resonance and Cooper minimum”. In: *Phys. Rev. A* 94.1 (2016), p. 013429. DOI: 10.1103/PhysRevA.94.013429 (cit. on p. 70).
- [123] A. Mandal et al. “Angle-resolved Wigner time delay in atomic photoionization: The 4d subshell of free and confined Xe”. In: *Phys. Rev. A* 96.5 (2017), p. 053407. DOI: 10.1103/PhysRevA.96.053407 (cit. on p. 70).
- [124] G. Wachter. “Simulation of condensed matter dynamics in strong femtosecond laser pulses”. PhD thesis. Technische Universität Wien, 2014 (cit. on p. 74).
- [125] F. Siek et al. “Angular momentum–induced delays in solid-state photoemission enhanced by intra-atomic interactions”. In: *Science* 357.6357 (2017), pp. 1274–1277. DOI: 10.1126/science.aam9598 (cit. on p. 74).
- [126] R. Locher et al. “Energy-dependent photoemission delays from noble metal surfaces by attosecond interferometry”. In: *Optica* 2.5 (2015), pp. 405–410. DOI: 10.1364/OPTICA.2.000405 (cit. on p. 74).
- [127] L. Kasmi et al. “Effective mass effect in attosecond electron transport”. In: *Optica* 4.12 (2017), pp. 1492–1497. DOI: 10.1364/OPTICA.4.001492 (cit. on p. 74).
- [128] F. Schlaepfer et al. “Gouy phase shift for annular beam profiles in attosecond experiments”. In: *Opt. Express* 25.4 (2017), pp. 3646–3655. DOI: 10.1364/OE.25.003646 (cit. on p. 74).
- [129] D. Hoff et al. “Tracing the phase of focused broadband laser pulses”. In: *Nat. Phys.* 13.10 (2017), pp. 947–951. DOI: 10.1038/nphys4185 (cit. on p. 74).
- [130] M. Ossiander et al. “Absolute timing of the photoelectric effect”. In: *Nature* 561.7723 (2018), pp. 374–377. DOI: 10.1038/s41586-018-0503-6 (cit. on pp. 75, 77, 78, 80, 83).
- [131] M. Ossiander. “On the Expansion of Attosecond Streaking Spectroscopy towards Ultrafast Surface Dynamics”. Master Thesis. Technische Universität München, 2014 (cit. on p. 75).
- [132] J. Riemensberger. “PhD Thesis (submitted)”. PhD thesis. Technische Universität München, 2018 (cit. on pp. 75, 79).
- [133] P. Dowben and R. Jones. “A re-interpretation of the LEED structures formed by iodine on W(110)”. In: *Surf. Sci.* 105.1 (1981), pp. 334–346. DOI: 10.1016/0039-6028(81)90166-7 (cit. on p. 76).
- [134] S. Pülm et al. “Iodine adsorption on clean and cesiated W(110) studied with UPS and metastable impact electron spectroscopy (MIES)”. In: *Surf. Sci.* 325.1-2 (1995), pp. 75–84. DOI: 10.1016/0039-6028(94)00790-X (cit. on p. 76).

-
- [135] R. G. Jones. “Halogen adsorption on solid surfaces”. In: *Prog. Surf. Sci.* 27.1-2 (1988), pp. 25–160. DOI: 10.1016/0079-6816(88)90013-5 (cit. on p. 76).
- [136] M. Gerl. “Time-resolved investigation of photoelectron dynamics by Attosecond Streaking Spectroscopy on solids”. Master Thesis. Technische Universität München, 2013 (cit. on pp. 79, 105).
- [137] L. Nahon, A. Svensson, and P. Morin. “Experimental study of the 4d ionization continuum in atomic iodine by photoelectron and photoion spectroscopy”. In: *Phys. Rev. A* 43.5 (1991), pp. 2328–2337. DOI: 10.1103/PhysRevA.43.2328 (cit. on p. 79).
- [138] M. Y. Amusia et al. “Photoionization of atomic iodine and its ions”. In: *Phys. Rev. A* 61.2 (2000), p. 020701. DOI: 10.1103/PhysRevA.61.020701 (cit. on p. 79).
- [139] S. Hüfner. *Photoelectron Spectroscopy*. Berlin: Springer-Verlag, 2003. DOI: 10.1007/978-3-662-09280-4 (cit. on p. 80).
- [140] S. Tanuma et al. “Experimental determination of electron inelastic mean free paths in 13 elemental solids in the 50 to 5000 eV energy range by elastic-peak electron spectroscopy”. In: *Surf. Interface Anal.* 37.11 (2005), pp. 833–845. DOI: 10.1002/sia.2102 (cit. on p. 81).
- [141] C. Lemell et al. “Simulation of attosecond streaking of electrons emitted from a tungsten surface”. In: *Phys. Rev. A* 79.6 (2009), p. 062901. DOI: 10.1103/PhysRevA.79.062901 (cit. on p. 81).
- [142] E. E. Krasovskii. “Attosecond spectroscopy of solids: Streaking phase shift due to lattice scattering”. In: *Phys. Rev. B - Condens. Matter Mater. Phys.* 84.19 (2011), pp. 1–5. DOI: 10.1103/PhysRevB.84.195106 (cit. on p. 81).
- [143] T.-W. Pi, L.-H. Hong, and C.-P. Cheng. “Synchrotron-radiation photoemission study of Ba on W(110)”. In: *Phys. Rev. B* 58.7 (1998), pp. 4149–4155. DOI: 10.1103/PhysRevB.58.4149 (cit. on p. 81).
- [144] E. Morosan et al. “Strongly Correlated Materials”. In: *Adv. Mater.* 24.36 (2012), pp. 4896–4923. DOI: 10.1002/adma.201202018 (cit. on p. 85).
- [145] H. Ding et al. “Evolution of the Fermi Surface with Carrier Concentration in Bi₂Sr₂CaCu₂O_{8+d}”. In: *Phys. Rev. Lett.* 78.13 (1997), pp. 2628–2631. DOI: 10.1103/PhysRevLett.78.2628 (cit. on p. 85).
- [146] B. Keimer et al. “From quantum matter to high-temperature superconductivity in copper oxides”. In: *Nature* 518.7538 (2015), pp. 179–186. DOI: 10.1038/nature14165 (cit. on pp. 85, 86).
- [147] E. Sterpetti et al. “Comprehensive phase diagram of two-dimensional space charge doped Bi₂Sr₂CaCu₂O_{8+x}”. In: *Nat. Commun.* 8.1 (2017), p. 2060. DOI: 10.1038/s41467-017-02104-z (cit. on p. 85).
- [148] P. Gay et al. “Femtosecond Dynamics of BSCCO-2212”. In: *J. Low Temp. Phys.* 117.5/6 (1999), pp. 1025–1029. DOI: 10.1023/A:1022561904373 (cit. on p. 86).

- [149] K. W. DeLong et al. “Pulse retrieval in frequency-resolved optical gating based on the method of generalized projections”. In: *Opt. Lett.* 19.24 (1994), p. 2152. DOI: 10.1364/OL.19.002152 (cit. on pp. 96, 99).
- [150] Y. Mairesse and F. Quéré. “Frequency-resolved optical gating for complete reconstruction of attosecond bursts”. In: *Phys. Rev. A* 71.1 (2005), p. 011401. DOI: 10.1103/PhysRevA.71.011401 (cit. on p. 96).
- [151] J. Gagnon, E. Goulielmakis, and V. S. Yakovlev. “The accurate FROG characterization of attosecond pulses from streaking measurements”. In: *Appl. Phys. B* 92.1 (2008), pp. 25–32. DOI: 10.1007/s00340-008-3063-x (cit. on pp. 96, 99, 103, 104).
- [152] T. Carroll et al. “Xenon N_{4,5}O Auger spectrum—a useful calibration source”. In: *J. Electron Spectros. Relat. Phenomena* 125.2 (2002), pp. 127–132. DOI: 10.1016/S0368-2048(02)00134-2 (cit. on p. 104).
- [153] D. Shirley. “High-Resolution X-Ray Photoemission Spectrum of the Valence Bands of Gold”. In: *Phys. Rev. B* 5.12 (1972), pp. 4709–4714. DOI: 10.1103/PhysRevB.5.4709 (cit. on p. 105).
- [154] A. Proctor and P. M. A. Sherwood. “Data analysis techniques in x-ray photoelectron spectroscopy”. In: *Anal. Chem.* 54.1 (1982), pp. 13–19. DOI: 10.1021/ac00238a008 (cit. on p. 105).
- [155] A. L. Cavalieri et al. “Intense 1.5-cycle near infrared laser waveforms and their use for the generation of ultra-broadband soft-x-ray harmonic continua”. In: *New J. Phys.* 9.7 (2007), p. 242. DOI: 10.1088/1367-2630/9/7/242 (cit. on p. 107).
- [156] F. Lücking et al. “Long-term carrier-envelope-phase-stable few-cycle pulses by use of the feed-forward method”. In: *Opt. Lett.* 37.11 (2012), pp. 2076–2078. DOI: 10.1364/OL.37.002076 (cit. on p. 108).
- [157] W. Schweinberger et al. “Waveform-controlled near-single-cycle milli-joule laser pulses generate sub-10 nm extreme ultraviolet continua”. In: *Opt. Lett.* 37.17 (2012), pp. 3573–3575. DOI: 10.1364/OL.37.003573 (cit. on p. 109).
- [158] V. Shirvanyan. “Generation of mJ, sub-4-fs pulses via hollow-core fiber nonlinear pulse compression using the conjugate pressure-gradient method”. Master Thesis. Technische Universität München, 2015 (cit. on p. 109).
- [159] A. M. Duensing. “Generation of High-Power, Few-Cycle Laser Pulses by Spectral Broadening in a Differentially Pumped Hollow-Core Fiber Setup”. Master Thesis. Technische Universität München, 2016 (cit. on p. 110).
- [160] M. Wurzer. “Implementation and Characterization of an Attosecond Beamline”. Master Thesis. Technische Universität München, 2016 (cit. on p. 110).
- [161] M. Schultze et al. “State-of-the-art attosecond metrology”. In: *J. Electron Spectros. Relat. Phenomena* 184.3-6 (2011), pp. 68–77. DOI: 10.1016/j.elspec.2011.01.003 (cit. on p. 110).

-
- [162] M. O. Mittermair. “Development, Design and Implementation of a Diagnostic Unit for the Analysis of XUV Attosecond Pulses”. Master Thesis. Technische Universität München, 2015 (cit. on p. 110).
- [163] A. J. Späh. “Development , Design and Implementation of an Ultra-High Vacuum Chamber for Gas-Phase Attosecond Streaking Spectroscopy”. Master Thesis. Technische Universität München, 2015 (cit. on p. 110).
- [164] M. Fieß. “Advancing attosecond metrology”. PhD thesis. Ludwig-Maximilians-Universität München, 2010 (cit. on p. 111).
- [165] M. Fieß et al. “Versatile apparatus for attosecond metrology and spectroscopy”. In: *Rev. Sci. Instrum.* 81.9 (2010), p. 093103. DOI: 10.1063/1.3475689 (cit. on p. 111).
- [166] E. Magerl et al. “A flexible apparatus for attosecond photoelectron spectroscopy of solids and surfaces.” In: *Rev. Sci. Instrum.* 82.6 (2011), p. 063104. DOI: 10.1063/1.3596564 (cit. on p. 112).

Abbreviations

BiSCCO	bismuth-strontium-calcium-copper-oxide
CEO	carrier-to-envelope offset
CEP	carrier-to-envelope phase
CLC	Coulomb-laser-coupling
COE	center-of-energy
EWS	Eisenbud-Wigner-Smith
FWHM	full-width-at-half-maximum
IMFP	inelastic mean free path
NIR	near-infrared
RABBITT	reconstruction of attosecond beating by interference of two-photon transitions
sat. ML	saturated monolayers
SI	International System of Units
TDSE	time-dependent Schrödinger equation
VIS	visible
XUV	extreme-ultraviolet

Danksagung

Der Weg zu dieser Dissertation wurde von vielen Menschen durch kluge Gedanken und heitere Stunden geebnet. Beides war für ihre Entstehung unerlässlich, deshalb möchte ich mich herzlich bei all diesen Kollegen bedanken. Mein aufrichtiger Dank gilt:

Prof. Dr. Reinhard Kienberger für die Vielzahl an Möglichkeiten, welche er mir nicht nur während meines Doktorats, sondern meiner gesamten Zeit an seinem Lehrstuhl, eröffnete. Die Atmosphäre, in welcher eigene Projekte stets unterstützt wurden, sowie den Beistand bei deren Durchführung, weiß ich zu schätzen. Außerdem für den Zusammenhalt und die Stimmung am Lehrstuhl, für welche er maßgeblich verantwortlich war.

Martin Schultze für die Zusammenarbeit während des Supraleiter- und des Helium-Projekts, sowie dazwischen und danach. Von ihm habe ich viel gelernt und durch ihn habe ich viele interessante Menschen getroffen. Ferner dafür, mit mir tausend Meilen die Melone transportiert zu haben.

Florian Siegrist für die zum Jahr gewordene erste Woche seiner Masterarbeit im Heliumprojekt und für die Zeit während dieses Jahres.

Johann Riemensberger für viele Diskussionen und dafür, sich von einer 24-Stunden-Zugfahrt und dem Krebs-Unglück nicht abhalten gelassen zu haben, am Ende der Welt wandern zu gehen.

Prof. Dr. Peter Feulner für die stetige Hilfe mit jedweden Vakuum-Problem und dafür, dass er sich von nichts die gute Laune verderben ließ.

Dem Ozon-Team, Tobias Latka und Vage Shirvanyan, dafür, niemals die Hoffnung aufgegeben zu haben.

Dem E11-Attosekunden-Labor, für die perfekte Vorbereitung und die Unterstützung während der Iod-Strahlzeit und am Feierabend danach, vor allem Michael Mittermair, Martin Wagner, Rupert Heider und Andi Duensing, der mich nicht alleine auf die Zugspitze hat klettern lassen.

Dem AS3-Team, Dionysios Potamianos, Maximilian Schnitzenbaumer, Ayman Akil, Sebastian Jarosch und Michael Jobst, das die Beamline über die Jahre am Leben gehalten hat.

Dem MPQ-Reinraum-Team, Sabine Keiber, Annkatrin Sommer, Shawn Sederberg und Nicholas Karpowicz, mit welchem ich jahrelang Laser repariert habe.

Dem ganzen Lehrstuhl E11 dafür, wie herzlich er uns aufgenommen hat.

Meinen Büro-Kollegen am E11, Markus Wurzer und Albert Schletter, die die Anfertigung dieser Arbeit ertragen und deutlich angenehmer gemacht haben.

Der Gruppe von Prof. Dr. Burgdörfer, Renate Pazourek, Christoph Lemmel und Florian Libisch für die fruchtbare Zusammenarbeit und dafür, dass sie noch Anrufe aus München beantworten.

Olga Razskazovskaya und Alexander Guggenmos für die vielen Optiken, ohne die keines der vorgestellten Experimente stattgefunden hätte.

Wolfram Helml für die Erfahrung am Soleil in Paris.

Den vielen Personen im Hintergrund, welche die Institute am Laufen gehalten und Teile für unsere Experimente gefertigt haben.

Gerlinde, Konrad und Michael, die mich immer unterstützt haben und ohne die ich es nicht einmal an den Anfang dieser Arbeit geschafft hätte.

Lea, bald sind es zwölf Jahre.